

Master Thesis: Simulated Van Allen Belt Exposure of Zirconium Diboride by Electron Irradiation

Daniel Rønning

Delft University of Technology

Simulated Van Allen Belt Exposure of Zirconium Diboride by Electron Irradiation

by

Daniel Rønning

to obtain the degree of Master of Science
in Aerospace Structures and Materials

at Delft University of Technology,
to be defended on Friday, October 6, 2023, at 9:00 AM.

Student Number: 4659511
Project Duration: March 13, 2023 - October 6, 2023
Thesis Supervisor: Dr. Yinglu Tang
Faculty: Faculty of Aerospace Engineering, Delft

Cover: Parker Solar Prober Sketch NASA/JOHNS HOPKINS APL/BEN SMITH [1]
Style: TU Delft Report Style, with modifications by Daan Zwaneveld

Acknowledgment

Yinglu Tang, my project supervisor, was extremely helpful throughout the thesis process. She was a terrific motivator, kept track of my development, and was a patient mentor. I am also very grateful for her assistance in establishing relationship with other departments and externals such as ESTEC.

I would also like to thank Hans Brouwer, Lennart van Den Hengel, Nuno Dias, and Roy Awater for their help and expertise during the project's experimental phase.

Finally, I would like to thank my friends and family for their support throughout the thesis.

Sincerely,

Rønning, Daniel

Abstract

Due to their innately robust thermal and mechanical qualities, ultra-high temperature ceramics (UHTCs) such as zirconium diboride (ZrB_2) have been investigated as viable materials to be used in reusable thermal protection systems (TPS). TPSs are vital to a spacecraft's heat balance in atmospheric reentry and in space. Here, the thermal and optical properties are especially critical in determining the heat balance. However, radiation exposure in space can degrade such material properties, especially over a prolonged mission duration. The interaction of electron radiation-which can be found in the outer Van Allen belt with ZrB_2 has not been studied previously and was, therefore, the main scope of this study.

The response of thermo-optical properties of ZrB_2 to increasing electron radiation doses simulating 5, 10, and 50 years of outer Van Allen belt radiation exposure was investigated. ZrB_2 samples were made through spark plasma sintering and exposed to 3 MeV electron irradiation. The ZrB_2 samples were characterized by their microstructure, thermal conductivity, coefficient of thermal expansion (CTE), emittance, absorptivity, and surface roughness. It was found that ZrB_2 's thermo-optical properties showed high radiation resistance at these dosages, and no apparent microstructural change was observed after irradiation. However, the irradiated samples had, on average, a 29 % lower surface roughness than the unirradiated samples, possibly originating from electron sputtering. Moreover, ZrB_2 samples produced at various sintering temperatures did not display a different radiation resistance.

Contents

List of Figures	vii
List of Tables	viii
Nomenclature	ix
1 Introduction	1
2 Theoretical Background	3
2.1 Zirconium Diboride	3
2.1.1 Spark Plasma Sintering of ZrB ₂	4
2.1.2 Spacecraft Application	5
2.1.3 Thermal Properties	7
2.1.4 Surface Properties	9
2.2 Space Radiation	11
2.2.1 Interaction of Radiation with Materials	12
2.2.2 Deterioration of Materials by Irradiation	16
2.2.3 Radiation Studies of ZrB ₂	19
2.3 Expected Outcome of Electron Irradiation	19
3 Experimental Procedure	21
3.1 Spark Plasma Sintering	21
3.1.1 Preparation	22
3.1.2 SPS Parameters	22
3.2 Polishing and Cutting	24
3.3 Radiation Exposure	26
3.4 Material Characterization	28
3.4.1 Densification Measurements	28
3.4.2 XRD Analysis	28
3.4.3 SEM Analysis	29
3.4.4 Thermal Properties	30
3.4.5 Surface Roughness	32
3.4.6 Optical Properties	33
4 Results and Discussion	35
4.1 Pre-Irradiation Characterization	35
4.1.1 Densification Measurements	35
4.1.2 XRD-Analysis	36
4.2 Microstructure SEM Analysis	38
4.3 Thermal Conductivity	42
4.4 Coefficient of Thermal Expansion	45
4.5 Surface Roughness	50
4.6 Optical Measurements	52
4.6.1 Surface Roughness and Optical Properties Investigation	56
5 Conclusions	59

6 Further Recommendations	61
References	63
A X-ray Diffraction Reference Data in Vesta	68
B Reflectance Spectra of ZrB₂ Samples from Spectrophotometer	70
C CTE of ZrB₂ Samples	71
D Thermal Conductivity Data	72
E Transient temperature increase in Hot Disk	73
F Raw emittance data	74
G Calculated Lattice Parameters	76

List of Figures

2.1	Zirconium diboride hexagonal crystal structure [4]	3
2.2	Diagram of the spark plasma sintering set-up [10]	5
2.3	ZrB ₂ grain size and relative densities at different SPS temperatures [9]	5
2.4	Temperature capability and thermal conductivity of various high-temperature materials with a heat balance diagram of leading edge [11]	6
2.5	Electron (red line), phonon (blue line) and total thermal conductivity contribution (black line) in W m ⁻¹ K ⁻¹ as a function of temperature [17]	8
2.6	Roughness profile depicting R_a , R_t and the mean line [30]	10
2.7	Radiation intensities in space in terms of flux density and particle energy [31]	11
2.8	Trapped proton fluxes (>10 MeV) (left) and trapped electron fluxes (>1 MeV) (right) over Earth radii [33]	12
2.9	Mass stopping power for carbon (C) and lead (Pb) as a function of electron energy. The black line represents the critical energy E_c [41].	14
2.10	Longitudinal energy deposition for an electron and proton radiation source [41]	15
2.11	Stopping power of electron radiation in Zirconium Diboride [43]	16
2.12	Point defects of particle radiation [44]	17
2.13	Influence of radiation on thermal conductivity of Uranium Oxide [47]	17
2.14	Diagram of the sputtering process [51]	18
2.15	Reflectance spectra of olivine under irradiation [49]	18
3.1	Spark plasma sintering machine	21
3.2	Graphite die containing graphite foil	22
3.3	Sintering parameters temperature, piston force, average piston feed, and average relative piston translation	23
3.4	Plasma from sintering inside SPS	24
3.5	Diamond edge cutter	25
3.6	Samples in the Van de Graaf accelerator. Top left: Samples 1 and 2. Top right: Sample 3 and 4. Bottom: Sample 5-11.	26
3.7	Van de Graaf Accelerator at TU Delft [56]	27
3.8	Working principle of Van de Graaf accelerator [57]	27
3.9	Measured dose distribution profile of Van de Graaf accelerator	28
3.10	Fritsch Spartan pulverisette	29
3.11	Rigaku MiniFlex 600 XRD	29
3.12	JEOL JSM7000F scanning electron microscope	30
3.13	Hot Disk TPS 2200 setup	31
3.14	PerkinElmer TMA 4000	31
3.15	Cut location of ZrB ₂ samples indicated by dotted line	32
3.16	Surface roughness lines analyzed with Keyence laser microscope	32
3.17	Agilent UV-VIS-NIR spectrophotometer used for absorptance measurements	33
3.18	ET-100 thermal handheld emissometer	34
4.1	Relative densification of ZrB ₂ at various sintering temperatures	36

4.2	XRD pattern of crushed ZrB_2 sample (blue), raw purchased ZrB_2 powder (orange), reference ZrB_2 data (grey) and reference carbon data (yellow)	37
4.3	Left: LEM 400 X image of the unirradiated sample. Right: SEM 10,000 X image of the unirradiated sample.	39
4.4	Left: LEM 400 X image of the unirradiated sample. Right: SEM 10,000 X image of the unirradiated sample.	39
4.5	Left: LEM 400 X image of the unirradiated sample. Right: SEM 10,000 X image of the unirradiated sample.	39
4.6	Left: LEM 400 X image of the irradiated sample. Right: SEM 10,000 X image of the irradiated sample.	40
4.7	Left: LEM 400 X image of the irradiated sample. Right: SEM 10,000 X image of the irradiated sample.	40
4.8	Left: LEM 400 X image of the irradiated sample. Right: SEM 10,000 X image of the irradiated sample.	40
4.9	Left: SEM 100,000 X image of the irradiated sample. Right: SEM 100,000 X image of the irradiated sample.	41
4.10	TEM images of helium-irradiated ZrB_2 under different temperatures [53]	42
4.11	Thermal conductivity versus irradiation dose of ZrB_2	43
4.12	Thermal conductivity versus sintering temperature of ZrB_2	44
4.13	Thermal conductivity versus densification percentage of ZrB_2	45
4.14	Temperature and time of Sample 5 I in TMA	46
4.15	CTE versus electron irradiation dose of ZrB_2	47
4.16	CTE versus sintering temperature of ZrB_2	48
4.17	CTE versus densification percentage of ZrB_2	49
4.18	Temperature and dose rate of neutron, proton, electron and nickel irradiation and radiation-induced segregation [38]	49
4.19	Total profile and roughness profile of Sample 5 UI	51
4.20	Arithmetic mean roughness and irradiation dose	52
4.21	Solar absorptance and emittance of ZrB_2 plotted against irradiation dose	54
4.22	Emittance and sintering temperature of ZrB_2	55
4.23	Solar absorptance and sintering temperature of ZrB_2	56
4.24	Solar absorptance versus mean arithmetic roughness of ZrB_2	57
4.25	Emittance versus mean arithmetic roughness of ZrB_2	58
A.1	XRD ZrB_2 Reference [59]	68
A.2	XRD C Reference [60]	69
B.1	Reflectance spectra of ZrB_2 samples	70
E.1	Transient temperature increase during 2.5s	73

List of Tables

2.1	Overview of various TPS systems with regards to complexity, re-usability, and commercial use [12]	6
2.2	Coefficient of thermal expansion for ZrB_2 in lattice planes a and c as a function of temperature [22]	9
2.3	Comparison of the various radiation sources in space [34]	12
3.1	Overview of ZrB_2 sample batches	23
3.2	Sintering temperature of ZrB_2 samples	23
3.3	Polishing steps for ZrB_2 samples	24
3.4	Simulated years in the Van Allen belt converted to Van de Graaf dose and irradiation time of the samples using the Van de Graaf dose rate	27
4.1	ZrB_2 samples' sintering temperatures, density, and densification	36
4.2	Peak positions in XRD data and Vesta, and calculated interplanar spacing	38
4.3	Calculated lattice parameters c and a	38
4.4	Grain sizes of irradiated and unirradiated ZrB_2 samples	41
4.5	Hot Disk calculated values and parameters for sample 5 UI	43
4.6	Arithmetic mean roughness and maximum roughness of unirradiated and irradiated samples	50
4.7	Directional thermal emittance at angles of 20° and 60° and total hemispherical emittance	53
C.1	CTE of unirradiated and irradiated samples	71
D.1	Thermal conductivity of unirradiated and irradiated samples	72
F.1	Reflectance values (R) for emittance angles of 20° and 60°	75
G.1	Calculated lattice parameters and average values	76

Nomenclature

Symbols

Description	Symbol	Value
Electronvolt	eV	$1.6 \times 10^{-19} \text{ J}$
Lorenz number	L	$2.44 \times 10^{-8} \text{ V}^2\text{K}^2$
Speed of light in vacuum	c	$299,792,458 \text{ m s}^{-1}$
Solar heat radiation at Earth	SF_s	1358 W m^{-2}
Stefan-Boltzmann constant	σ	$5.67 \times 10^{-8} \text{ W K}^{-4} \text{ m}^{-2}$
Area	A	-
Temperature	T	-
Sievert	Sv	-
Kelvin	K	-
Arithmetic Mean Roughness	R_a	-
Maximum Roughness	R_z	-
Gray	Gy	-

Abbreviations

CTE	Coefficient of Thermal Expansion
SPE	Solar Particle Events
CMC	Ceramic Matrix Composite
CME	Coronal Mass Ejection
GCR	Galactic Cosmic Rays
TEM	Transmission Electron Microscopy
SEM	Scanning Electron Microscopy
LET	Linear Energy Transfer
PKA	Primary Knock-on Atom
SPS	Spark Plasma Sintering
TPS	Thermal Protection System
TBC	Thermal Barrier Coating
HP	Hot Pressing
UHTC	Ultra-High Temperature Ceramic
LEO	Low Earth Orbit
HZE	High atomic number (Z) and Energy
SRIM	Stopping and Range of Ions in Matter
XRD	X-ray Diffraction
I	Irradiated
UI	Unirradiated

1

Introduction

Over the last century, the worldwide space industry has been expanding quickly, necessitating an increased need for research into innovative materials for space. Due to their inherent strong material characteristics, such as a high melting temperature, medium to high thermal conductivity, and high strength, UHTCs (ceramics with melting temperatures above 3000 °C) such as ZrB_2 are a potential option for spacecraft and rocket applications.

One of the most common uses of UHTCs in space is for reentry heat shields, but ZrB_2 has not been widely used yet for this purpose. Although ZrB_2 is a promising material for TPS systems in space applications, it faces several problems. It is critical for the future of space exploration that TPSs can be manufactured on a larger scale, which is difficult for ZrB_2 . In addition, UHTCs are exceedingly brittle on their own. Hence, strategies to improve this must be researched in the future. In this case, using additives or ultra-high temperature ceramic matrix composites (UHTCMCS) could make ZrB_2 more practical as a TPS [2] which, however, will not be in the scope of this thesis. In this study, the intrinsic material property degradation of monolithic ZrB_2 under extreme conditions will be the main focus. Furthermore, a TPS system should have adequate thermal (thermal conductivity and thermal expansion), optical (emittance and absorption), and mechanical qualities for its intended use [2]. In addition, the TPS system should preferably be reusable for several reentries, which means it must withstand repeated degradation from oxidation in the atmosphere, heat extremes, and radiation.

In many ways, especially given its radioactive environment, space is harsh. It is crucial to understand the shielding potential of outer materials for spacecraft to prevent damage to essential electronics, optical systems, and payloads. However, radiation will also interact with these outer materials, which could cause deterioration, particularly over a longer mission duration [3]. Understanding how these materials are affected by the radioactive environment of space is crucial for developing new spacecraft. How high energy electron radiation might affect the material properties of ZrB_2 has yet to be studied, a type of radiation prevalent in the Van Allen belts surrounding Earth.

The primary research objective of the thesis is to investigate the influence of 3 MeV electron radiation on ZrB_2 samples created by spark plasma sintering. This will be conducted using electron radiation dosage levels to simulate increasing durations in the Van Allen belt. Next, the production properties of the UHTC, such as its sintering temperature and density, will be varied during processing to evaluate its influence on the radiation resistance. This is conducted to investigate how the processing of ZrB_2 can be optimized to limit radiation damage.

The two main research questions are formulated based on the mentioned research objectives, each containing several sub-research questions.

- **What is the effect of increasing 3 MeV electron radiation dose on the degradation of ZrB₂?**
 - How is the micro-structure of ZrB₂ altered by 3 MeV electron radiation?
 - What are the effects on thermal properties such as thermal conductivity and thermal expansion?
 - What are the effects on surface properties such as surface roughness, solar absorptance, and emittance?
- **How does increasing the sintering temperature of the spark plasma sintering (SPS) process of ZrB₂ affect its radiation resistance?**
 - What are the effects of a varying density on its thermal properties after irradiation?
 - How does sintering temperature affect the optical properties of ZrB₂?

Chapter 2 will explain the underlying material science theory of ZrB₂, how space radiation interacts with materials and radiation-induced degradation. In Chapter 3, the experimental procedure of this study will be presented. Chapter 4 will analyze and compare the material properties of irradiated and unirradiated ZrB₂ samples. This is followed by the conclusions drawn from this study in Chapter 5, and recommendations for future work in Chapter 6.

2

Theoretical Background

This chapter will discuss the fundamental background theory on the research topic of this thesis. Initially, zirconium diboride and its primary material properties will be discussed, followed by its use as a thermal protection system in space and the thermo-optical properties of the UHTC. The following sections will explain the space radiation environment, its interaction with materials, and radiation-initiated material deterioration. Finally, existing research into the radiation impacts of ZrB_2 will be analyzed, from which the hypotheses of this study are formed.

2.1. Zirconium Diboride

Since the 1950s, zirconium diboride has been investigated for use in nuclear and aerospace applications. Due to its excellent thermal qualities, including a high melting temperature and high thermal conductivity, it has also been studied for its possible use in hypersonic flight and reentry spacecraft.

The UHTC has a hexagonal crystal structure, in which zirconium atoms occupy the corners and Boron atoms occupy the interstitial sites, depicted in Figure 2.1. ZrB_2 is a metal diboride (MB_2) ceramic which is similar in crystal structure as the other variations; AlB_2 , HfB_2 and MgB_2 . Their proximity in the periodic table also coincides with a similarity in material properties. They are considered superior alternatives within specific high-temperature applications compared to carbides and nitrides, as they have excellent mechanical properties, thermal properties, and oxidation resistance [4].

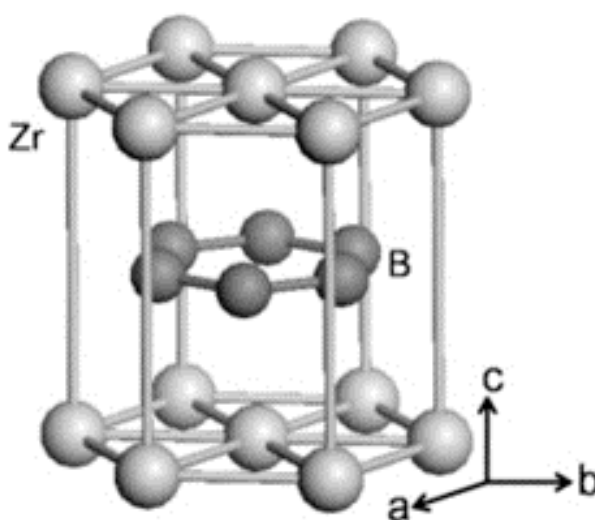


Figure 2.1: Zirconium diboride hexagonal crystal structure [4]

The base unit has a six-membered ring of boron atoms, and the zirconium atom plane has seven atoms in a hexagonal structure. Six other in-plane zirconium atoms surround each zirconium atom, with 12 nearest boron atom neighbors in adjacent planes. Each boron atom is surrounded by three boron atoms in the plane and six zirconium nearest neighbors in adjacent planes [4]. The crystal structure contains covalent, ionic, and metallic bonds. This allows the diboride to have a high melting point, hardness, thermal conductivity, and electrical conductivity. The boron sub-lattice and Zr-B bonds are connected through covalent bonding. On the other hand, Zr atoms are connected through metallic bonding, which provides high thermal and electrical conductivity [5]. Due to the crystal structure's anisotropic nature, the diboride's thermal conductivity differs for various lattice directions [6].

2.1.1. Spark Plasma Sintering of ZrB_2

The synthesis method of ZrB_2 largely depends on the UHTC's end use and the required production scale. For coating applications, chemical/physical vapor deposition is often utilized. However, this research will focus on bulk samples of ZrB_2 . For bulk production of ZrB_2 with high purities, reactive or chemical synthesis through densification is utilized [7]. Material parameters such as density, grain size, and stoichiometry are manipulated through various production methods. The following are the most common densification methods of zirconium diboride: hot pressing, arc melting, sintering, and spark plasma sintering, with spark plasma sintering being the densification method used to produce the ZrB_2 samples in this research.

Spark plasma sintering (SPS), which allows for exceptionally high melting temperatures, is frequently utilized for UHTCs. It uses a combination of heat, pressure, and current to densify materials. In addition to requiring a lower heat than traditional sintering, it also reduces the time needed to sinter the material, often resulting in smaller grain sizes. In SPS, graphite rods exert a uniaxial pressure on the powdered material as a direct current (DC) flows through it. The current causes heating of several thousand degrees. Next, Joule heating occurs on the borders between the particles due to the material's resistance [8]. Figure 2.2 displays the setup of an SPS system. The graphite mold entirely surrounds the sintered powder to create an isolated and homogenous thermal environment.

There are several advantages of using SPS in UHTC production. First, the microstructure can have superior mechanical properties as the grain growth can be controlled, and the density is typically higher. For ZrB_2 , spark plasma sintering can clean the oxides of the powders through a local spark discharge. Next, SPS heats the sample from the center, whereas other methods heat the sample externally, allowing for a more homogeneous heating. The grain growth is also lower from the increased rate of heating and the external force. A smaller grain size makes the material mechanically stronger [7]. The grain size and density of the ceramic can be manipulated in the processing stage by changing the sintering temperature, but also by varying the holding time and heating rate [9]. This can be seen in Figure 2.3, where the grain size and relative density of ZrB_2 for sintering temperatures of 1800 °C, 1850 °C, 1900 °C and 1950 °C is shown [9]. It can be observed that both properties follow a positive correlation with the sintering temperature.

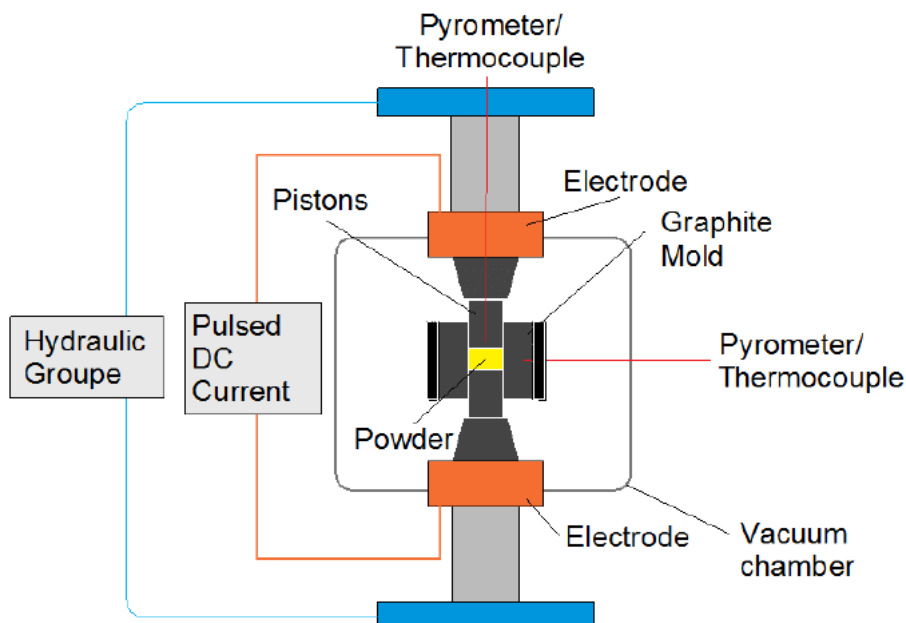


Figure 2.2: Diagram of the spark plasma sintering set-up [10]

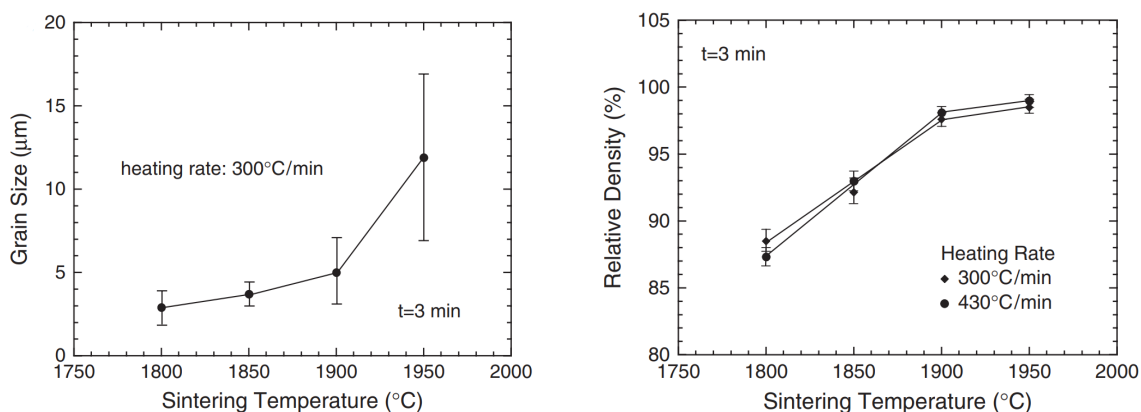


Figure 2.3: ZrB_2 grain size and relative densities at different SPS temperatures [9]

2.1.2. Spacecraft Application

This study's main scope is to research the radiation resistance of bulk ZrB_2 as a potential material in space applications. One of the most common uses of ceramics in space is in refractory reentry heat shields or thermal protection coating. There is excellent potential for UHTC heat shields to increase the reusability of reentry spacecraft, in contrast to ablative heat shields which need to be continuously replaced. However, zirconium diboride has not been widely used in space compared to other ceramics. This is mainly due to the material's current challenges in becoming commercially viable. Figure 2.4 displays various ceramic-based materials' temperature capability and thermal conductivity. It also shows the heat transfer mechanisms on the leading edge of a reentry vehicle. It can be seen that UHTC carbides, carbon-carbon composites, and UHTC borides show the highest temperature capability but have higher thermal conductivities.

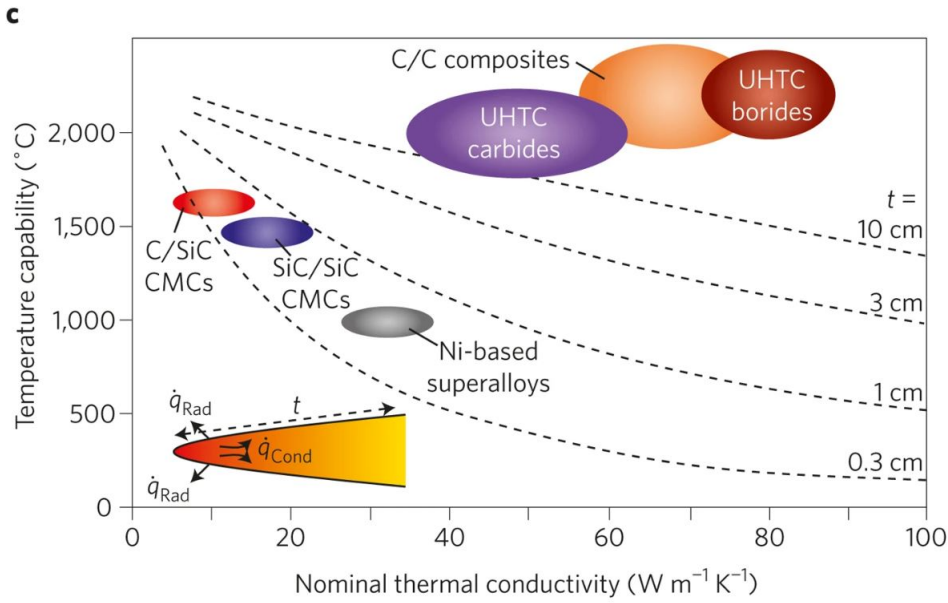


Figure 2.4: Temperature capability and thermal conductivity of various high-temperature materials with a heat balance diagram of leading edge [11]

Thermal protection systems (TPS) are divided into three different categories; passive, semi-passive, and active. The various types of TPS within these are listed in Table 2.1. Ablative TPS burn their layers as the spacecraft re-enters, dissipating thermal energy through chemical reactions. These are often made from materials such as cork with very low thermal conductivity to prevent heat flow into the spacecraft. Refractory re-entry shields (hot structures) are often made with materials such as ceramics and have been used in the Space Shuttle. These materials must have a very high melting point but low thermal conductivity. Cooled systems use active cooling methods to redirect heat from the heat shield material back into the atmosphere or to coolants [12] [2]. A UHTC-based TPS is a type of passive hot structure since it does not require power to operate. As seen in Table 2.1, this has not been implemented to a great degree commercially, but has a relatively low integration complexity and also has a high reusability potential.

TPS	Example mechanisms	Complexity	Reusability	Commercial use
Passive	Heat sink	Low	High	Low
	Hot structure			
	Insulated structure			
Semi-passive	Heat pipes	Medium	Low	High
	Ablators			
Active	Transpiration cooling	High	Medium	Low
	Film cooling			
	Convective cooling			

Table 2.1: Overview of various TPS systems with regards to complexity, re-usability, and commercial use [12]

The primary heat sources for a reentry vehicle are convection between hot surrounding gas and the vehicle and radiative heating from the shock layer on the body. The following equations (Equation 2.1, 2.2, 2.3, and 2.4) show the derivation of the heat balance at the leading edge of a reentry spacecraft. Here, q_{conv} is the convective heating, q_R is the radiative heating, and q_{rad} is the radiative cooling. Both heat sources depend on the velocity V and radius R of the spacecraft and the density ρ of the

medium. Radiative cooling depends on the thermal emittance ε_0 of the surface, Stefan-Boltzmann constant σ , and the temperature of the body T . The temperature on the spacecraft's surface can be calculated by balancing the outward radiative cooling with radiative and convective heating [13]. The optical properties of the material influence the radiative heating and cooling. Next to this, the amount of heat transported to the spacecraft and its components is tied to the thermal conductivity of the heat shield. Therefore, these two properties are fundamental to the viability of ZrB_2 as a heat shield material.

$$q_{conv} \propto V^3 \left(\frac{\rho}{R}\right)^{0.5} \quad (2.1)$$

$$q_R \propto V^8 \rho^{1.2} R^{0.5} \quad (2.2)$$

$$q_{rad} = \varepsilon_0 \sigma T^4 \quad (2.3)$$

$$q_{rad} = q_{conv} + q_R \quad (2.4)$$

From the above discussion, it can be understood that the TPS's thermo-optical material qualities are essential to their functionality and thermal control. In addition, solar absorptivity and emittance are also necessary for the heat balance of a spacecraft in orbit. Therefore, the main emphasis of this thesis is on these qualities of ZrB_2 .

2.1.3. Thermal Properties

Thermal conductivity describes the ability of a material to conduct heat and is measured in $\text{W m}^{-1} \text{K}^{-1}$. For a reentry heatshield, this is an important parameter to determine the heat transport to its spacecraft interfaces. The thermal conductivity of MB_2 ceramics is similar for different temperatures due to their similarity in crystal structure. Due to the anisotropic nature of ZrB_2 , the thermal conductivity is different for the various planes. In the *c*-plane, the thermal conductivity of single crystal ZrB_2 has been measured to be $95\text{--}102 \text{ W m}^{-1} \text{K}^{-1}$ while perpendicular to this plane, it is $132\text{--}145 \text{ W m}^{-1} \text{K}^{-1}$ at room temperature [6]. This is comparable to metals of high conductivity such as aluminum ($205 \text{ W m}^{-1} \text{K}^{-1}$), steel ($50.2 \text{ W m}^{-1} \text{K}^{-1}$), and substantially higher than other materials such as glass ($0.8 \text{ W m}^{-1} \text{K}^{-1}$) [14]. This parameter is closely related to the material's crystal structure and has electron and phonon (lattice vibration) contributions. Figure 2.5 displays the thermal conductivity of ZrB_2 contributed by the electron movement (red), phonon (blue), and total conductivity (black). It can be seen that the electron movement contributes to the majority of the thermal conductivity for ZrB_2 , and both contributions decrease with temperature. The phonon contribution is inversely proportional to temperature, and according to theory, the electron contribution is linearly related to temperature as seen in Equation 2.5. However, this is not reflected in Figure 2.5. This is because as the temperature of metals increases, there are more collisions between electrons and atoms due to increasing lattice vibrations [15]. Next to this, higher densities are generally accompanied by higher thermal conductivities due to a decrease in the mean free path of electrons and higher phonon densities [16].

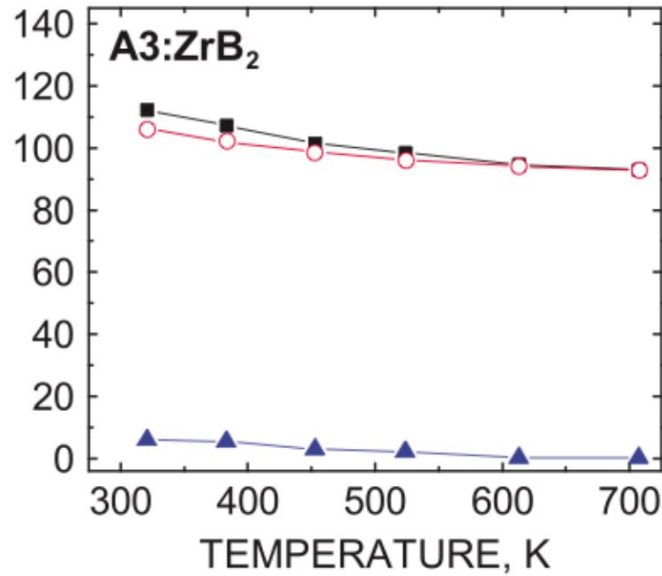


Figure 2.5: Electron (red line), phonon (blue line) and total thermal conductivity contribution (black line) in $\text{W m}^{-1} \text{K}^{-1}$ as a function of temperature [17]

$$\lambda_e = L\sigma T \quad (2.5)$$

A material undergoing numerous heating and/or cooling cycles suffers from thermal fatigue caused by the thermal expansion and contraction of the material. The extent to which a material expands or contracts is connected to its **coefficient of thermal expansion** (CTE). Typically UHTCs such as ZrB_2 have a low coefficient of thermal expansion. This can be advantageous in applications where material displacements have to be minimized over smaller periods. Yet, with interfaces to materials with different expansion coefficients, this could lead to high stress at certain locations. As seen in Equation 2.6, the CTE (α_l) depends on the initial and final temperature (T_1 and T_2), as well as the initial and final elongation (l_1 and l_2). Because ZrB_2 is anisotropic, there are different coefficients of expansion depending on the lattice direction, as seen in Table 2.2, which also increases with increasing temperatures. This is due to an increased disruption in the interatomic forces and increased anharmonicity of phonons [18]. At room temperature, the CTE of ZrB_2 is $6.7\text{E-}6 \text{ K}^{-1}$ in the a-plane and $6.9\text{E-}6 \text{ K}^{-1}$ in the c-plane. Comparitively, steel has a CTE of $12\text{E-}6 \text{ K}^{-1}$, aluminium has a CTE of $20\text{E-}6 \text{ K}^{-1}$ and nickel has a CTE of $13\text{E-}6 \text{ K}^{-1}$ [19]. The coefficient of thermal expansion is highly related to the crystal bonds of the material, with higher energy (stronger) bonds having lower coefficients of thermal expansion [18]. In addition, denser solids and solids that have more closely packed crystal structures generally have lower thermal expansion coefficients [20][21].

$$\frac{l_2 - l_1}{l_1} = \alpha_l(T_2 - T_1) \quad (2.6)$$

Temperature K	α_a 10^{-6} K^{-1}	α_c 10^{-6} K^{-1}
300	4.17	4.55
400	4.68	4.98
500	5.19	5.41
600	5.70	5.83
700	6.20	6.26
800	6.71	6.68
900	7.21	7.10
1000	7.71	7.52
1100	8.21	7.95

Table 2.2: Coefficient of thermal expansion for ZrB_2 in lattice planes a and c as a function of temperature [22]

2.1.4. Surface Properties

The previous section highlighted the importance of optical properties in the heat balance of spacecraft. Optical properties refer to the interaction between a material's surface and electromagnetic radiation and include parameters such as an object's transmissivity, absorption, and reflectivity. The conservation of energy is the sum of the intensity of transmissivity, reflectivity, and absorptivity, which is equal to 1. For opaque materials such as ZrB_2 , I_T is 0 [23]. Next to this, the **emittance** of material measures the thermal energy emitted by an object through blackbody radiation and can take on a value between 0 and 1. A perfect black body is a material that absorbs all incident radiation and hence $\epsilon_0 = 1$ and $I_A = 1$. There are several different measures of emittance depending on the wavelength (spectral or full-wavelength), as well as the direction of radiation (directional, normal, and hemispherical) [23]. Hemispherical emittance is the emittance across half a sphere. It is defined by the ratio of the total hemispherical emittance of a material and that of a black body [24]. Additionally, The hemispherical emittance ϵ_0 can be derived using a weighted average of the directional emissivities [25]. **Solar absorptivity** is the absorption of electromagnetic radiation of a material in the spectrum between 250-2000 nm. For ZrB_2 , the solar absorptivity is $\alpha = 0.47$ and the hemispherical emittance is $\epsilon_0 = 0.18$ [26]. This can be used to estimate the heat radiated using Equation 2.3.

The optical properties of a material are closely tied to the temperature of the material as well as surface impurities. These properties are highly dependent on the **surface roughness** of the sample as well as the effect of oxidation. There are two classifications of the surface of a material: optically smooth and rough. An optically smooth surface is an ideal case, and for a rough surface, there are three subcategories: a specular region, an intermediate region, and a geometric region. The region depends on the ratio of the root mean square of the surface roughness of the material to the wavelength of the radiation $\frac{\sigma}{\lambda}$ [27]. The surface roughness of a material can be measured using several parameters. The most common of these is R_a , the mean arithmetic roughness, and R_t , the maximum distance between the peak and the valley of the surface. Equations 2.7 and 2.8 show how these variables are calculated, where l_r is the evaluation length and $Z(x)$ is the roughness profile [28]. Figure 2.6 depicts these parameters in the roughness profile. It has also been found that with decreasing emittance values, the surface roughness has a higher influence on the heat transfer ability of a material [29].

$$R_a = \frac{1}{l_r} \int_0^{l_r} |Z(x)| dx \quad (2.7)$$

$$R_z = \text{Min}(Z(x)) + \text{Max}(Z(x)) \tag{2.8}$$

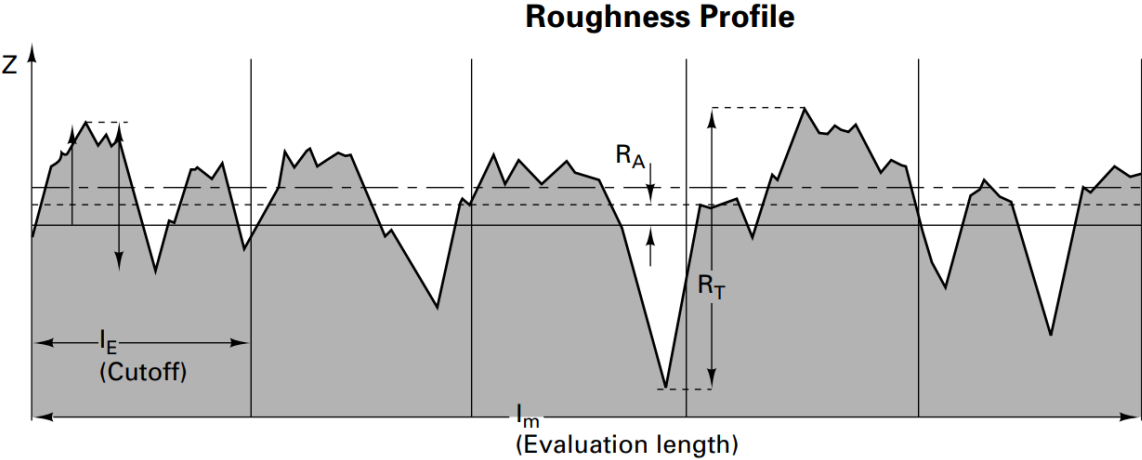


Figure 2.6: Roughness profile depicting R_a , R_t and the mean line [30]

2.2. Space Radiation

There are several sources of high-energy radiation present throughout the solar system. Some sources are more consistent in their particle fluxes, such as that in the Van Allen belt, while others are single events, such as solar particle events. The measured particle flux density and energies of the various types of radiation encountered in space can vary greatly, as shown in Figure 2.7. It can be seen that there is a general trend across the radiation sources, where lower flux densities accompany higher particle energy. The three primary sources of radiation experienced by spacecraft in the solar system are:

- Solar particle events
- Galactic cosmic rays
- Van Allen belt radiation

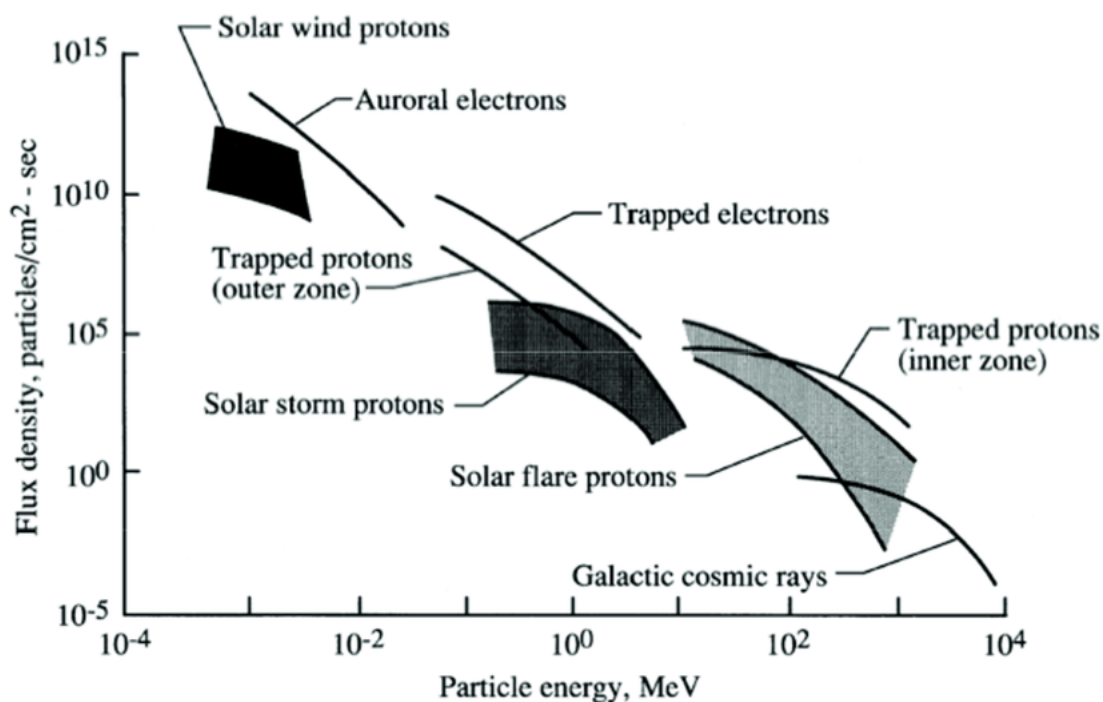


Figure 2.7: Radiation intensities in space in terms of flux density and particle energy [31]

A region containing radioactive particles surrounds the Earth, known as the Van Allen belt. The zone is split into an outer zone, which primarily includes electrons, and an inner zone, which contains protons and electrons. Earth's magnetic field traps these charged particles, produced mainly by solar wind and cosmic rays. The particle fluxes are variable depending on the sunspot number and peak during the decline from the solar maximum [32]. However, it is a significantly more steady radiation environment than solar wind and cosmic rays. The location of the Van Allen belt is critical to understanding in planning space missions. The inner belt begins at about 500 km and extends to over 12,000 km. The outer zone starts at a minimum altitude of approximately 13,000 km and extends to more than 60,000 km [33]. Additionally, electron energies range between 10 keV to more than 100 MeV in the Van Allen belt. On the other hand, the proton energies range from 100 keV to more than 100 MeV [33]. Figure 2.8 displays the trapped electrons and proton flux distribution in the Van Allen belt.

Table 2.3 highlights the essential characteristics of the aforementioned radiation sources in terms of location, energy, duration, particle composition, and relative dose rate. Because of their continuous nature, the GCR and Van Allen belt radiation are the most destructive radiation sources for a re-entry

spacecraft that may remain in orbit for an extended time, or be reused for multiple missions. The radiation type that will be replicated in this study is electron radiation, specifically that present in the Van Allen belt's outer rim. These electrons have energies ranging from 0.1 to 10 MeV, whilst the electron source employed in this study is a 3 MeV Van de Graaf source. This is especially relevant for geostationary satellite deployment, Moon missions, or deeper space missions [34]. With an increasing need for space exploration and reusability concerns, there is a clear need for research into the effects of radiation on spacecraft materials. Other particle sources, such as helium sources, gamma rays, or protons, can simulate radiation such as SPEs and GCRs. However, this is not within the scope of this study.

Radiation source	Location	Max. energy	Duration	Particle Types	Dose rate
SPE	Solar system	1 GeV	Hours/days	Protons, electrons and alpha particles	High
Van Allen belt	Earth orbit	100 MeV	Continuous	Protons and electrons	High
GCR	Solar system	10 GeV	Continuous	85% protons 14% alpha particles 1% HZE particles	Low

Table 2.3: Comparison of the various radiation sources in space [34]

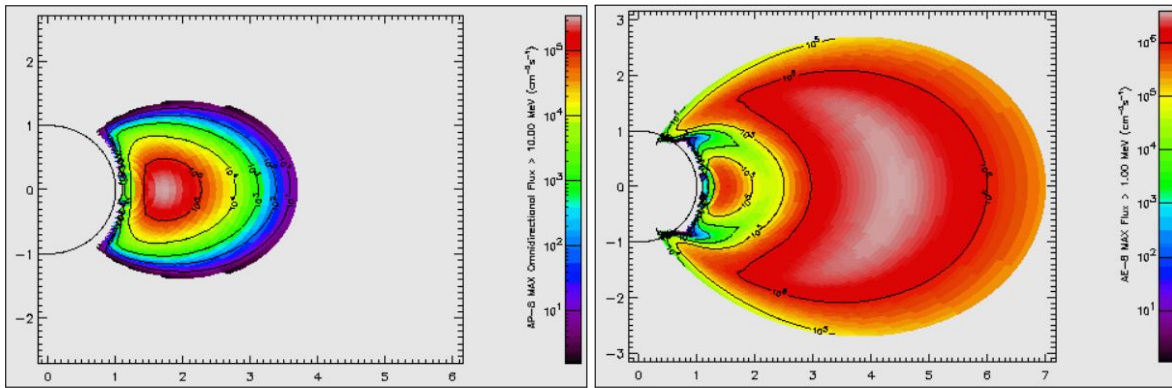


Figure 2.8: Trapped proton fluxes (>10 MeV) (left) and trapped electron fluxes (>1 MeV) (right) over Earth radii [33]

2.2.1. Interaction of Radiation with Materials

Particles have different interactions with material depending on the nature of the irradiating particle and the target material. Ions can interact with electrons and nuclei, and the cross-section σ depends on the energy E , proton number Z , and mass number A , as seen in Equation 2.9. When ions interact with matter, three main processes can occur depending on the energy of the particle:

$$\sigma = \sigma(E, A, Z) \quad (2.9)$$

- Nuclear fragmentation
- Ionization loss
- Radiative energy loss

In nuclear fragmentation, the nucleus of the target body is fragmented and the fragment projectiles have the same direction as the incident ion. This is the main damage mechanism of ions in materials. In

particle-electron collisions, the particles can also cause ionization (loss of an electron) and excitation of the electron, where an excited electron goes to a higher energy state. The energy loss, dE , per unit path length, dx , from ionization loss is given by the quantum-mechanical Bethe-Bloch relationship in Equation 2.10. Here, m_e is the electron rest mass, z is the irradiating particle charge, n is the electron number density, c is the speed of light in vacuum, ϵ_0 is the vacuum permittivity and I is the mean excitation energy. Generally, the mean excitation energy of a particle decreases with increasing atomic Z number, but there are also outliers. The electron number density depends on the atomic number of the material Z , the density of the material ρ , the Avagadro number N_A , the atomic mass A and the molar mass constant M_u [35].

$$-\left\langle \frac{dE}{dx} \right\rangle = \frac{4\pi}{m_e c^2} \cdot \frac{nz^2}{\beta^2} \cdot \left(\frac{e^2}{4\pi\epsilon_0} \right)^2 \cdot \left[\ln \left(\frac{2m_e c^2 \beta^2}{I \cdot (1 - \beta^2)} \right) - \beta^2 \right] \quad (2.10)$$

where,

$$\beta = \frac{v}{c} \quad \text{and} \quad n = \frac{N_A \cdot Z \cdot \rho}{A \cdot M_u} \quad (2.11)$$

The equation reduces to the following form for lower particle energies where $\beta \ll 1$.

$$-\frac{dE}{dx} = \frac{4\pi n z^2}{m_e v^2} \cdot \left(\frac{e^2}{4\pi\epsilon_0} \right)^2 \cdot \ln \left(\frac{2m_e v^2}{I} \right) \quad (2.12)$$

The radiation source used in this study is an electron source (beta particle). As opposed to ions and neutrons, electrons do not cause nuclear fragmentation. For electrons, the Bethe-Bloch formula changes due to their indistinguishability, small mass, and energy loss as a result of the Bremsstrahlung effect. As a result of this, additional terms are added to the equation, as well as the stopping power resulting from the Bremsstrahlung effect as seen in Equation 2.13 [36][37]. Here, T is the kinetic energy of the electron.

$$\begin{aligned} -\left\langle \frac{dE}{dx} \right\rangle &= \frac{4\pi}{m_e c^2} \cdot \frac{nz^2}{\beta^2} \cdot \left(\frac{e^2}{4\pi\epsilon_0} \right)^2 \cdot \left[\ln \left(\frac{2m_e c^2 \beta^2}{I \cdot (1 - \beta^2)} \right) - \beta^2 + (1 - \beta^2) \right. \\ &\quad \left. - \left(2\sqrt{1 - \beta^2} - 1 - \beta^2 \right) \ln 2 + \frac{1}{8} \left(1 - \sqrt{1 - \beta^2} \right)^2 \right] + \left\langle \frac{dE}{dx} \right\rangle_r \end{aligned} \quad (2.13)$$

where,

$$\left\langle \frac{dE}{dx} \right\rangle_r = \left(\frac{e^2}{4\pi\epsilon_0} \right)^2 \frac{Z^2 N_A (T + m_e c^2) \rho}{137 m_e^2 c^4 A} \left[4 \ln \frac{2(T + m_e c^2)}{m_e c^2} - \frac{4}{3} \right] \quad (2.14)$$

As mentioned before, the ionization potential of the radiation increases with mass, therefore the damage caused by electron irradiation is not as severe as that of ions. The penetration depth of electrons is also deeper because of a lower ionization potential. There are three interaction mechanisms of electron radiation with materials; knock-on damage, radiolysis, and heating effect. With knock-on damage, the electron scatters elastically with a nucleus which creates a point defect which is the main damage mechanism of electrons. The transferred energy to the atom is given by Equation 2.15 where E_0 is the incident electron energy, θ is the electron's deflection through the nucleus and Z is the atomic number. The minimum radiation energy to knock out an atom from its lattice site can be estimated by taking $\theta=180^\circ$ and $E = E_d$: the displacement energy of the specified element. For zirconium and boron, this

is 40 eV and 19.36 eV respectively [38] [39]. On the other hand, inelastic scattering leads to radiolysis where chemical bonds are broken, as well as heating effects [40].

$$E = E_0 \frac{\sin^2 \theta / 2 (1.02 + E_0 / 106)}{465.7 Z} \quad (2.15)$$

Compared to larger particles, radiation losses dominate at lower energies for electrons. This can be seen in Figure 2.9, plotting the mass stopping power in carbon and lead for electrons. For the 3 MeV radiation source used in this study, it could be understood that the loss of ionization would likely dominate with a ZrB_2 density of approximately 6.119 g/cm^2 . The critical energy E_c describes the transition between the domination of ionization losses and radiation losses. For zirconium, the critical energy is 14.74 eV, while for boron, it is 93.94 eV and it generally decreases with increasing Z -number [41]. To calculate the radiation length of electrons X_0 , Equation 2.16 can be used with the material density ρ , atomic number Z , and mass number A [41]. The radiation length is the mean distance required to decrease the irradiating electron by a factor of $1/e$ as given by Equation 2.17.

$$X_0 = \frac{716.4 \text{ g/cm}^2 A \rho}{Z(Z + 1) \ln(287/\sqrt{Z})} \quad (2.16)$$

$$\langle E(x) \rangle = E_0 \cdot \exp\left(-\frac{x}{X_0}\right) \quad (2.17)$$

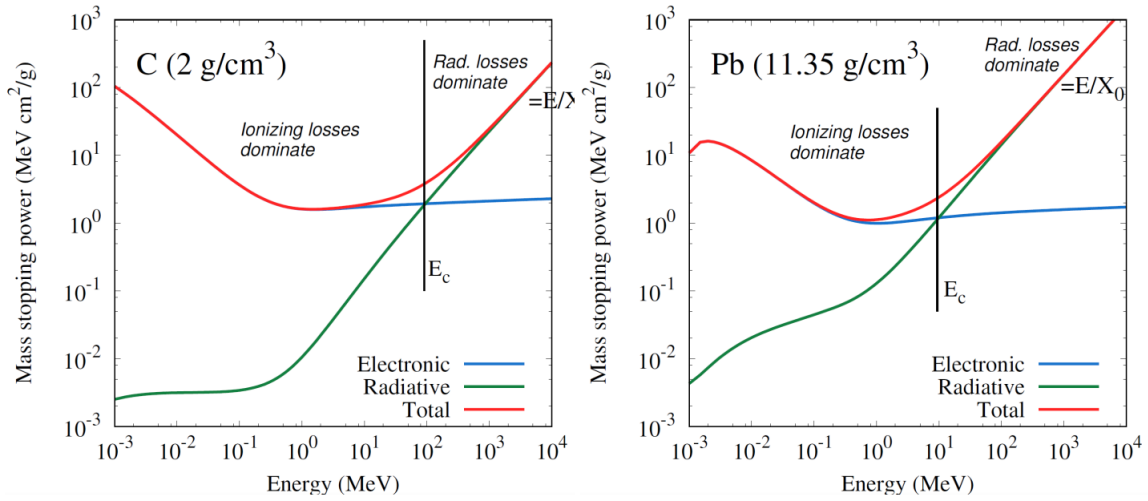


Figure 2.9: Mass stopping power for carbon (C) and lead (Pb) as a function of electron energy. The black line represents the critical energy E_c [41].

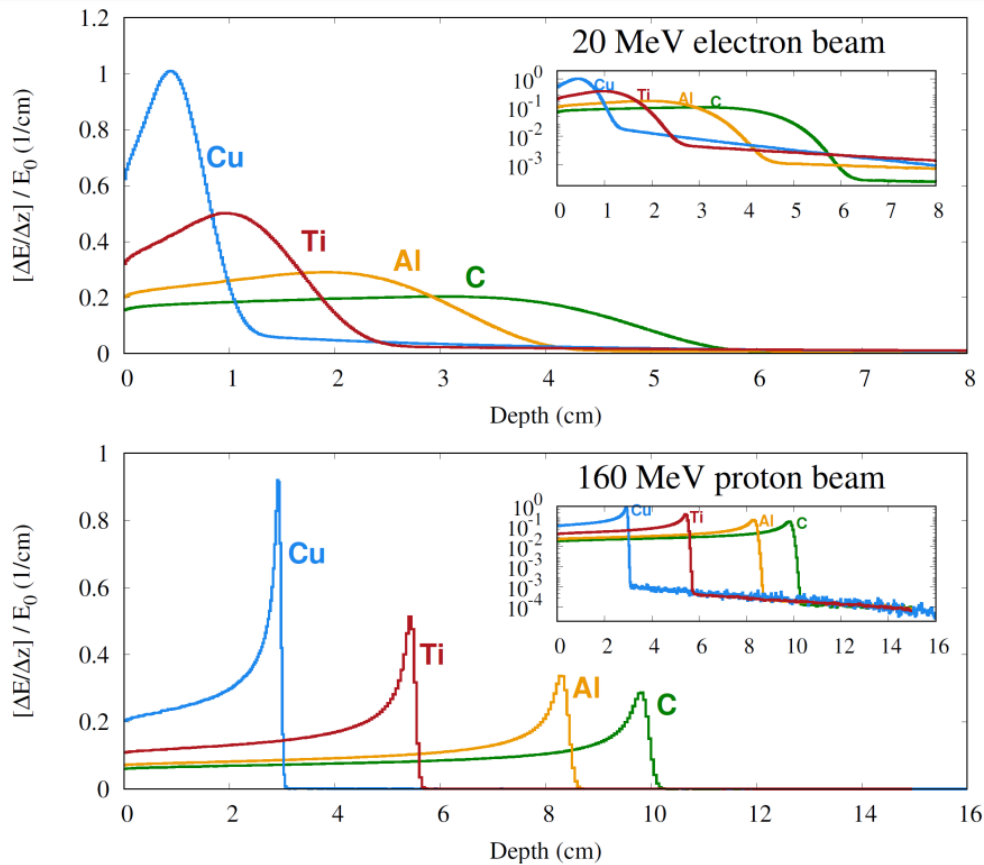


Figure 2.10: Longitudinal energy deposition for an electron and proton radiation source [41]

Studying particle interactions within materials experimentally can be tedious and require accurate equipment. To gain an improved understanding of the interaction, computer simulations can be used as well. This is done using molecular dynamics simulations and simulating the potentials between the atoms. The most common method to simulate this interaction is the Monte Carlo particle transport method. Displacement cascades can be modeled using Binary Collision Approximation, commonly used by SRIM (Stopping and Range of Ions in Matter) [42]. There are also methods to predetermine the stopping power of various materials to electron radiation. One way is using the Bethe-Block theory to calculate the electronic stopping power and a Bremsstrahlung energy spectrum to calculate radiative stopping power. This is implemented in the ESTAR program by NIST [43] and can be used to estimate the total stopping power in specific elements. Using the density and chemical formula, the stopping power for other materials can also be calculated, as seen in Figure 2.11.

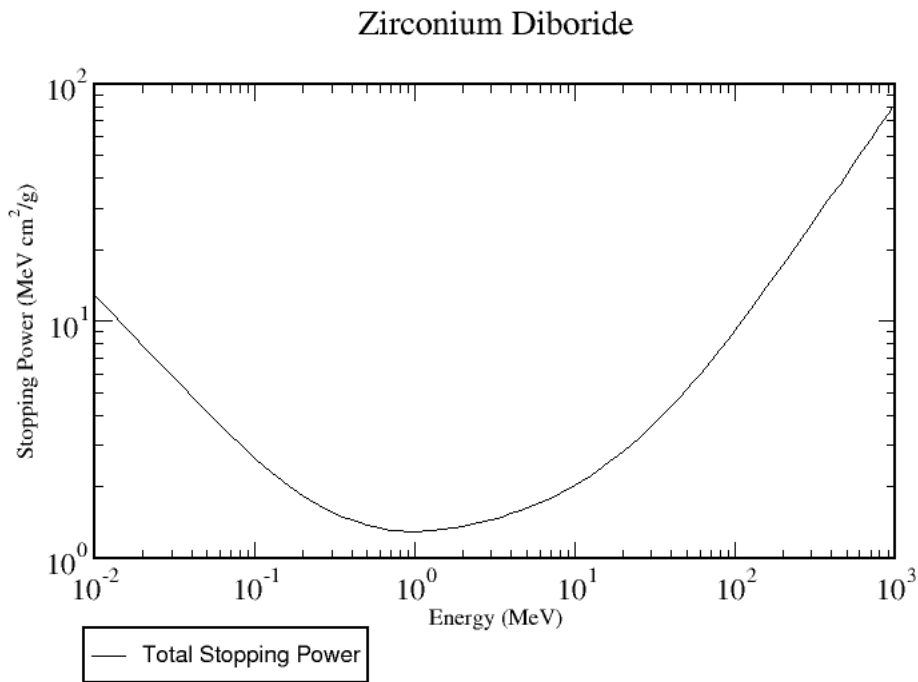


Figure 2.11: Stopping power of electron radiation in Zirconium Diboride [43]

2.2.2. Deterioration of Materials by Irradiation

Depending on the type, intensity, and duration of the ionizing radiation, radiation can influence spacecraft materials. This may have a long-term effect on the structure and influence the density, thermal conductivity, compressive strength, surface characteristics, and elastic modulus of the materials. Nuclear stopping power, which causes primary knock-on atom (PKA) effects and cascade reactions inside the material, is the primary cause of material degradation. Thus, electrons do not harm materials to the same degree as ions as the location where nuclear stopping and cascade reactions occur experiences a spike in the local temperature. Figure 2.12 displays the various point defects induced by radiation onto silicon. Here, a) represents a substitutional defect where the particle takes the silicon's place, b) represents an interstitial defect where the particle moves in the free space around the crystal structure, c) represents a silicon vacancy defect, and d) represents a Frenkel defect [44]. The material's crystal structure is also highly influential in the deterioration due to radiation. Radiation has the most significant impact on covalent bonds and less effect on ionic and metallic bonds. This is due to the destruction of the molecules, by breaking up pairs of electron bonds. On the other hand, in ionic bonding, electrons are held in atomic orbits so damage is limited. Lastly, in metallic bonding, free electrons can replace stripped electrons which minimizes the damage caused [45].

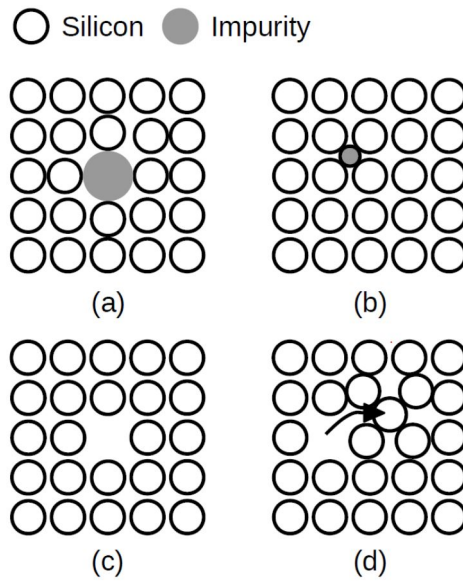


Figure 2.12: Point defects of particle radiation [44]

In metals and ceramics, irradiation reduces thermal and electrical conductivity. This is because radiation damage creates a more unorganized crystal lattice that, in turn, slows heat and electricity transport [46]. Weisensee, Feser, and Cahill investigated how increasing Argon radiation doses influenced the thermal conductivity of a thin film of uranium oxide, which can be seen in Figure 2.13. This was done for samples at various irradiation temperatures, where the thermal conductivity was measured through time-domain thermorefectance. It can be observed that the conductivity decreases under higher irradiation doses, and is generally higher at lower temperatures [47].

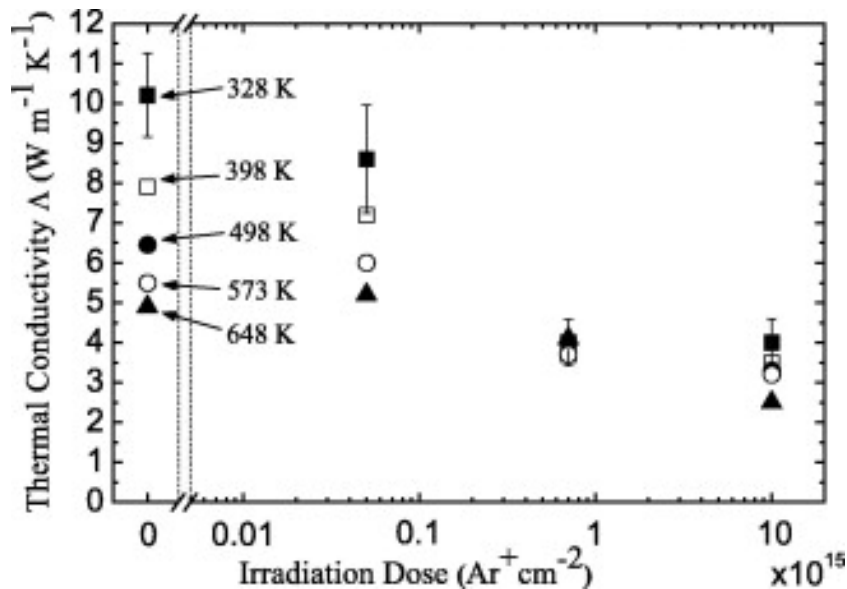


Figure 2.13: Influence of radiation on thermal conductivity of Uranium Oxide [47]

For space applications, it is essential to understand the possible surface effects of radiation as this could influence the heat transfer ability of the surface. In space, there are cases where radiation affects optical properties, such as the decreasing albedo on the moon due to radiation [48]. For ceramics, there are no existing studies investigating the optical effects of radiation. However, this has been studied exper-

imentally with olivine pellets to simulate asteroid surfaces. The olivine was under proton and argon irradiation, where it can be seen that the reflectance spectrum shifts rightwards with increasing fluences (Figure 2.15) [49]. Since most irradiation damage originates from nuclear stopping or ionization loss, there are limited surface defects. However, sputtering could occur in which impingement particles collide with surface atoms, causing cascades from which atoms are ejected from the material, as seen in Figure 2.14. This could be due to electron sputtering, where electrons are the incident particle. In addition to this, ion implantation could also take place with ion irradiation. This describes the phenomena where the incident radiation takes the place of irradiated material's location [50].

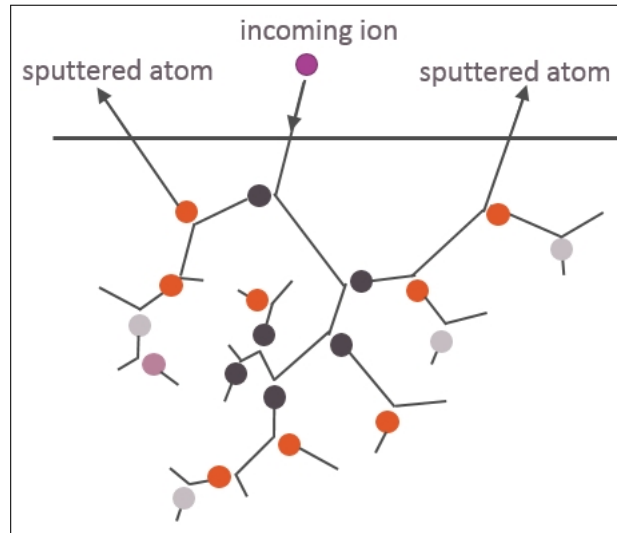


Figure 2.14: Diagram of the sputtering process [51]

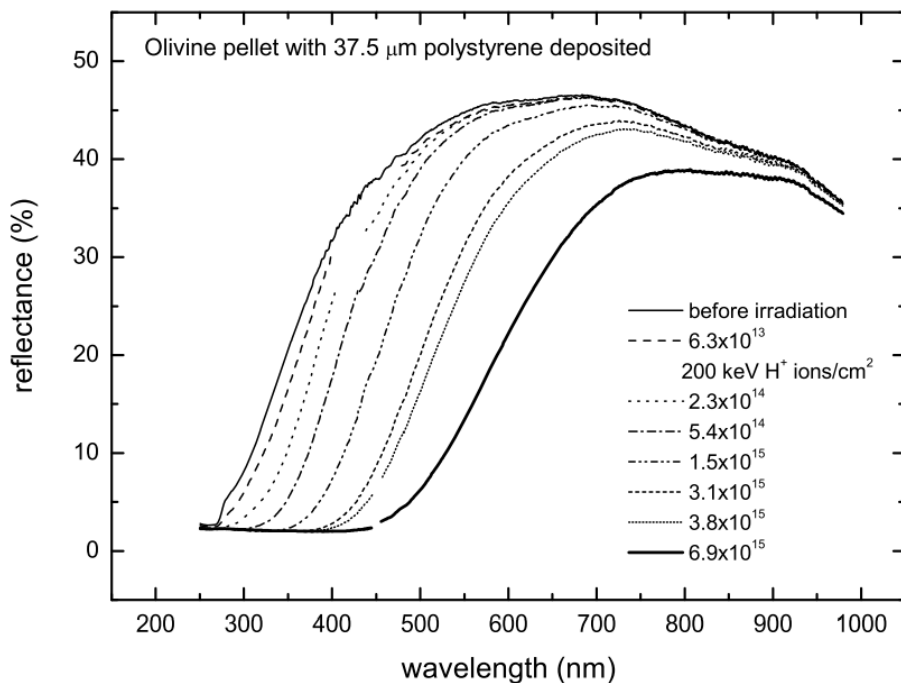


Figure 2.15: Reflectance spectra of olivine under irradiation [49]

2.2.3. Radiation Studies of ZrB₂

The majority of previous radiation studies of ZrB₂ have focused on its nuclear energy application, using heavier ion radiation such as neutron, helium, and gold particles. Therefore, no published studies have investigated the interaction of ZrB₂ with electron irradiation. Nevertheless, it is helpful to analyze similar studies to understand the type of damage that can arise and their implemented methods.

Bao et al. studied ion irradiation of ZrB₂ for nuclear applications. To simulate neutron radiation effects in materials such as cascades and to avoid creating radioactive materials, surrogates can be used to mimic the impact [52]. An example of such a material is Gold (Au). The study used 4 MeV Au ions with a dose rate of 2.5×10^{16} ions/cm² to irradiate ZrB₂ samples created by hot pressing. The study found that the crystal structure was well-maintained after irradiation. Through various analysis methods, it was found that there was some damage to the lattice, including interstitials, boron vacancies, and dislocations. This was accompanied by an increase in the lattice constant *a* and a decrease in the lattice constant *c*, leading to a volume shrinkage of 0.46 %. There were also extended dislocations at the shallow depths of the material (<250 nm) and minor dislocations further into the material (750-1150 nm) [39].

Garrison et al. investigated the damage to ZrB₂ by 30 keV He irradiation for plasma-facing materials in fusion reactors. This was done at temperatures between 920-1120 K and two different Helium fluences of 8.4×10^{21} He/m² and 5×10^{22} He/m² with six samples. Surface morphology changes, such as ripples and pores, were elevated at higher irradiation fluences. It was also found that the surface of the ZrB₂ samples changed from a matte grey to blue and brown in the irradiated areas. It was observed that the intensity of the color change was more significant at higher fluences. There was also a mass loss from ion implantation and sputtering mechanisms, but no apparent relationship with the irradiation fluence or temperature was observed. In the mass loss calculation, the effects of oxidation were also included to ensure that they did not affect the results. The exact source of the color change was not experimentally verified. Yet, it was hypothesized to be sourced in nanostructures caused by the irradiation, which were comparable in size to the wavelength of light causing interference. Through x-ray photoelectron spectroscopy (XPS), it was found that there was a high amount of carbon on the ZrB₂ samples' surface. However, the study fails to explain the high presence of carbon by the surface >25% and the possibility that this could have influenced the color changes [53].

It has previously been found that irradiation of ZrB₂ can affect surface characteristics by changing the color and causing mass loss, but also bulk features by influencing lattice parameters. This is closely tied to thermal properties such as thermal conductivity and expansion, but these were not studied. Additionally, none of the previous studies have investigated the influence of electron radiation on ZrB₂, which is especially critical for its application in space environments such as the Van Allen belt.

2.3. Expected Outcome of Electron Irradiation

Although there is limited published research into the influence of electron irradiation on the material properties that will be investigated in this thesis, closely related research can still be analyzed to formulate a hypothesis on the study's outcome.

Based on research on particle irradiation of ZrB₂ and the underlying theory of electron radiation effects in materials, it is expected that the electron irradiation will influence the surface properties through electron sputtering and the bulk thermal properties of the material by creating point defects. However, the extent to which this will be detectable is uncertain. The irradiation energy is higher than in previous studies with ZrB₂ (MeV range), but electrons will have more penetration power and less interaction with the material. It is expected that the surface roughness will increase due to electron scattering, subsequently influencing the absorptance and emittance. As seen with the particle irradiation of olivine, the reflectance spectrum shifted rightwards with higher irradiation fluences in the wavelength range 250-1000 nm [49]. This would have influenced the solar absorptance as it is within its wavelength range.

Based on the shift in the reflectance spectra, it is therefore expected that the solar absorptance would increase with increasing fluences. It is also expected that the emittance will be influenced as well, but the possible relationship with increasing doses is difficult to presume due to a lack of similar studies.

Next, with a more disorganized lattice caused by increased irradiation, the thermal conductivity is expected to decrease, and the coefficient of thermal expansion is expected to increase. A more disorganized lattice will decrease the electron transport speed and hence reduce the electron conductivity [54]. It has also been seen that the thermal conductivity reduces with increased Argon irradiation doses [47]. On the other hand, it is expected that the CTE will increase due to weaker bonding and more room for expansion due to a higher presence of defects.

It is expected that with increased sintering temperatures, ZrB_2 will have a higher density as seen in Figure 2.3, and have bulk properties more influenced by irradiation (a decreased radiation resistance). The irradiation is expected to affect bulk thermal parameters more prominently as the UHTC will have a higher stopping power as given by Equation 2.13. On the other hand, the optical properties' radiation resistance is not expected to be significantly influenced by higher sintering temperatures, but the properties themselves could be affected by the different sintering temperatures. Additionally, higher densities are expected to increase the thermal conductivity and decrease the CTE of ZrB_2 as explained in Section 2.1.

The microstructure of ZrB_2 is expected to show irradiation effects, similar to what was reported by Bao et al. in the Gold irradiation study. It is expected that the effects of electron sputtering will lead to visible dislocation effects on the surface. These will be less visible than with ion irradiation, but they are expected to be present due to the high energy levels of the electron radiation.

Nevertheless, it is expected that electron irradiation of ZrB_2 will have a lessened effect on the material properties compared with ion irradiation. This is mainly attributed to the lack of nuclear interaction and the higher penetration power of electrons. Nevertheless, since it is an unexplored area of research, it is important to confirm that the damage onto ZrB_2 is minimized. In the following chapter, the experiments conducted to investigate the electron irradiation influence on ZrB_2 will be described.

3

Experimental Procedure

This chapter will describe the experimental procedure for the thesis research. Here, equipment, setups, and measurement methods related to the various steps of the experiments will be explained. There were three primary phases to the experiments: 1. the spark plasma sintering of ZrB_2 , 2. radiation exposure of ZrB_2 , and 3. pre- and post-irradiation characterization of ZrB_2 . Before conducting experiments to answer the research question, a preparatory investigation into the SPS procedure, the thermal measurement methods, and material characterization techniques were done.

3.1. Spark Plasma Sintering

The spark plasma sintering machine from FCT Systeme GmbH used to produce the ZrB_2 samples can be seen in Figure 3.1. The main features displayed in this image are the vacuum chamber on the right side and the operating screen on the left.



Figure 3.1: Spark plasma sintering machine

3.1.1. Preparation

For spark plasma sintering of the samples, ZrB_2 powder from Nanografi was used. The powder had a purity of 99.5%, a particle size of $5.5 \mu\text{m}$, and was made of 80% zirconium and 18.9% boron.

The powder was inserted into a graphite die to produce the ZrB_2 samples. Two graphite punches were also inserted into the die, in which thin graphite foil was placed between the die and powder to ensure a uniform electric current. Figure 3.2 displays the graphite die with the foil inside it. The foil was rolled up to ensure two cylindrical layers between the punches and the die. Two circular graphite foils were also placed between the punches and the powder to ensure that the graphite foils surrounded the powder. After the powder was filled inside the mold, the graphite die and punches were mounted onto the pistons in the SPS machine.

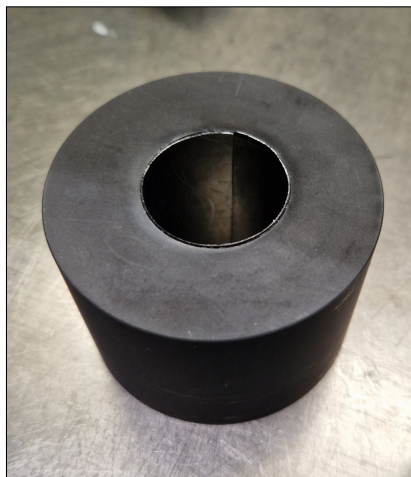


Figure 3.2: Graphite die containing graphite foil

3.1.2. SPS Parameters

The sintered samples had a diameter of 30 mm and a thickness of 3 mm. This was assured using a graphite die and punches with 30 mm diameter, and by weighing 12.7 g of ZrB_2 powder (assuming a density of 6). This sample size was chosen to allow for uniform heat distribution in the sintering phase, as samples with larger diameters could have impurities caused by non-homogeneous temperature gradients throughout the SPS process.

Three batches of samples were produced, which are listed in Table 3.1. The sintering parameters were kept constant for the first batch, but the radiation exposure doses varied. In the second batch, the sintering temperature was varied to change the density of the samples. Based on previous research, this was determined to be the most impactful production parameter [9]. The sintering temperature was varied between 1800-2000 °C at increments of 50 °C (1800 °C, 1850 °C, 1900 °C, 1950 °C, 2000 °C) where one sample was made for each temperature as seen in Table 3.2. This was done to vary the densification between samples as demonstrated in Figure 2.3 [9]. Additionally, two extra samples were made at a sintering temperature of 2000 °C for XRD and SEM (Samples 11 and 12 in Batch 3). One sample was used for XRD to investigate impurities, while another sample was used for SEM analysis for microstructure analysis. All the samples were cut into two halves, one exposed to radiation and one unirradiated to analyze the influence of the radiation.

	Batch 1	Batch 2	Batch 3
Sample number	1-5	6-10	11-12
Sintering temperature °C	2000	1850-2000	2000
Radiation dose	Varying	Constant	Constant

Table 3.1: Overview of ZrB₂ sample batches

Samples	Sample 1	Sample 2	Sample 3	Sample 4	Sample 5	Sample 6
Temperature (°C)	2000	2000	2000	2000	2000	1800
Samples	Sample 7	Sample 8	Sample 9	Sample 10	Sample 11	Sample 12
Temperature (°C)	1850	1900	1950	2000	2000	2000

Table 3.2: Sintering temperature of ZrB₂ samples

The holding duration, force (pressure), and heating rate were other sintering parameters set besides temperature. The overall sintering time was altered due to the temperature change, while the heating and cooling rates remained constant. Some of the sintering parameters for samples produced at 2000 °C can be seen in Figure 3.3. The heating was carried out in two stages, the first of which lasted six minutes and involved a rise in temperature from 400 °C to 1500 °C for 15 minutes. After this point, the temperature increased from 1500 °C until 2000 °C (for Batch 1) over 2 minutes and 30 seconds (200 °C/min). Subsequently, the temperature was kept at 2000 °C for 10 minutes, after which it was cooled to 400 °C for 64 minutes (25 °C/ min). On the other hand, the punch force was kept at 5 kN for 21 minutes, then held at 56 kN for 15 minutes and 30 seconds. After that, it was reduced back to 5 kN for the remaining time. The plasma created in the vacuum chamber during sample production can be seen in Figure 3.4.

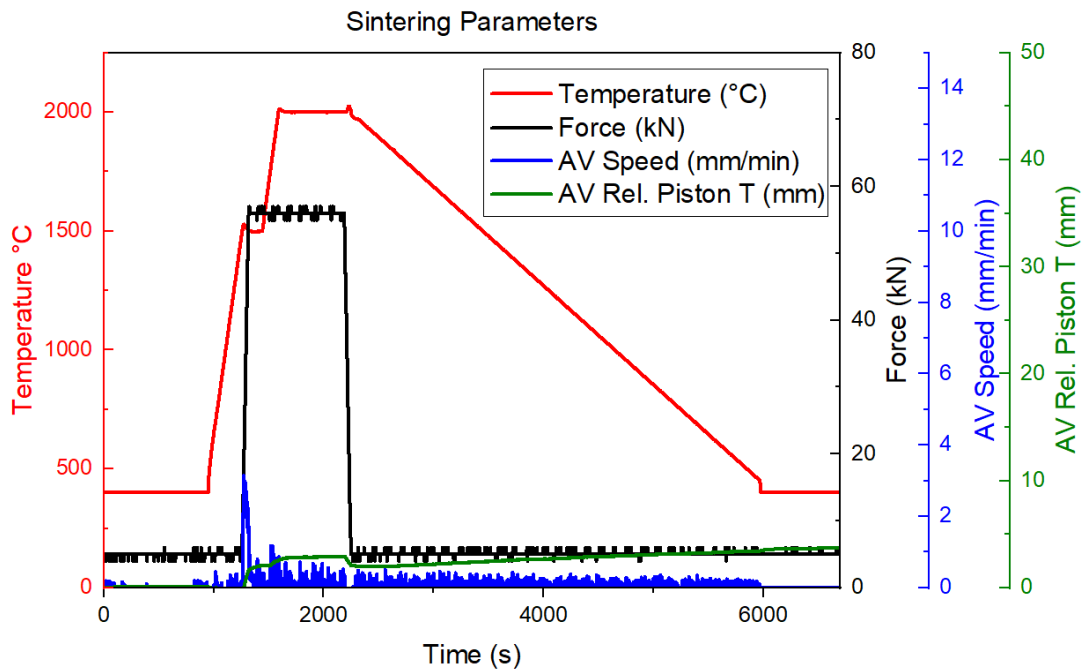


Figure 3.3: Sintering parameters temperature, piston force, average piston feed, and average relative piston translation



Figure 3.4: Plasma from sintering inside SPS

3.2. Polishing and Cutting

The samples had to be prepared for characterization after being synthesized using the SPS procedure. There was an excessive amount of graphite embedded on the surface of the ZrB_2 samples after SPS which had to be removed. To ensure that the embedded graphite in the ceramic did not affect the material analysis, polishing was required to remove it. The following steps were taken to polish the ZrB_2 samples in 3ME using a diamond-embedded polishing paper:

- Polishing the edges for 2 minutes
- Polishing both faces of the sample for 5 minutes
- Polishing both faces of the sample for 5 minutes while pressing a metal cylinder on the sample

About 0.2 mm of material was removed after the polishing steps above were carried out. After the samples were polished to remove the embedded graphite at 3ME, they were re-polished using a standardized polishing procedure at the aerospace faculty. Table 3.3 lists the standardized process of polishing papers and lubricants.

Surface	Lubricant	Duration (min:s)
SiC foil 320	Water	1:00
SiC foil 1000	Water	1:00
SiC foil 2000	Water	1:00
Dur3	DiaP	4:00
Dur1	DiaP	3:00
Chem	NonDry	1:00

Table 3.3: Polishing steps for ZrB_2 samples

The samples were then cut using a diamond edge cutter displayed in Figure 3.5. Here, the center line of the samples (at 1.5 cm) was marked, and the sample was held steady using a tool. The wheel speed was set to 2000 rpm, the feed speed was set to 0.075 mm/s, and the cut length was set to 75 mm. The ZrB_2 samples exposed to radiation can be seen in Figure 3.6.



Figure 3.5: Diamond edge cutter

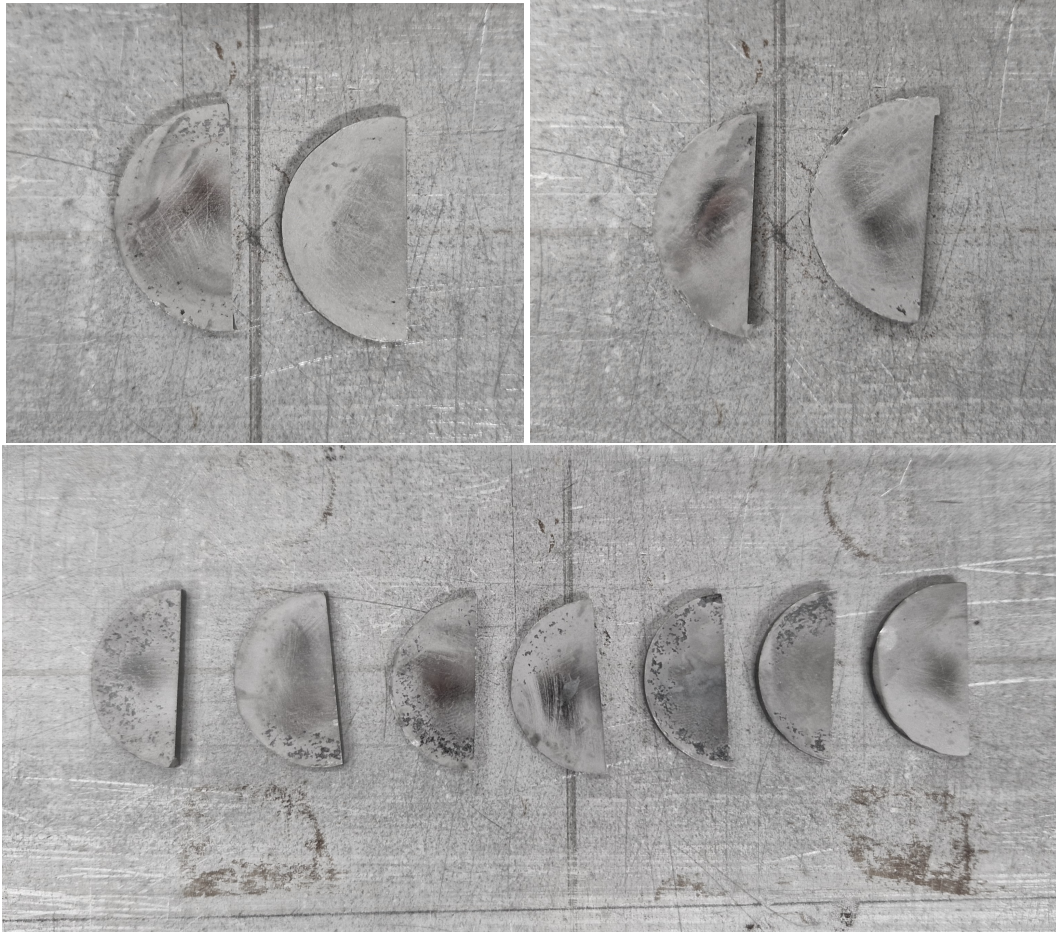


Figure 3.6: Samples in the Van de Graaf accelerator. Top left: Samples 1 and 2. Top right: Sample 3 and 4. Bottom: Sample 5-11.

3.3. Radiation Exposure

The electron radiation exposure was conducted using a Van de Graaf accelerator in the reaction institute at TU Delft, which can be seen in Figure 3.7. It uses a moving belt that collects charges on an insulated sphere, creating a high potential difference. The potential difference accelerates the electrons to high energies by creating an electron source which is shown in Figure 3.8. The ZrB_2 samples were exposed to electrons with an energy of 3 MeV at three different doses. Doses were varied by changing the irradiation time between 283.54 s (Sample 1 and 2), 466 s (Sample 3 and 4), and 1886.97 s (Sample 5-11). This was meant to simulate outer Van Allen belt radiation exposure for 5, 10, and 50 years, respectively, and was estimated by assuming an electron fluence of 1×10^6 as calculated in Equation 3.1 [55]. This coincided with the van de Graaf fluences in Table 3.4. The Van de Graaf fluence was calculated assuming a $29.0 \mu\text{A}$ beam current which resulted in an average dose of 66.6 kGy/cm^2 in 240 s. The electron beam produced inside the Van de Graaf accelerator did not have a perfectly homogeneous beam, as seen in the dose distribution in Figure 3.9. For this reason, the samples were placed along the center of the beamline to ensure a similar radiation environment.

$$\frac{50 \times 365 \times 24 \times 3600 \times 1 \times 10^6}{8.35 \times 10^{11}} = 1886.97 \quad (3.1)$$



Figure 3.7: Van de Graaf Accelerator at TU Delft [56]

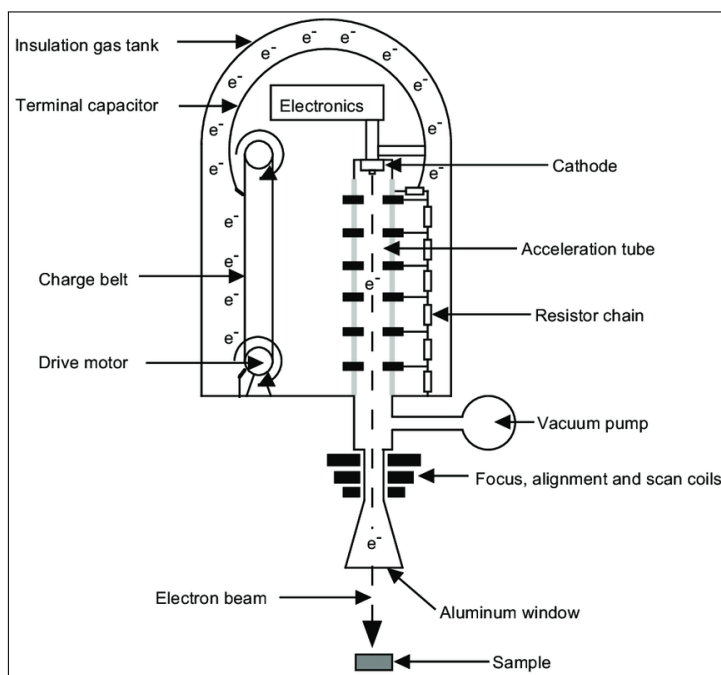


Figure 3.8: Working principle of Van de Graaf accelerator [57]

Simulated dur. (years)	Dose rate ($e^- \text{ cm}^{-2} \text{ s}^{-1}$)	Dose ($e^- \text{ cm}^{-2}$)	Irradiation time (s)
5	$5.55\text{E}+11$	$1576.9\text{E}+11$	283.54
10	$6.76\text{E}+11$	$3153.8\text{E}+11$	466.00
50	$8.35\text{E}+11$	$15769.4\text{E}+11$	1886.97

Table 3.4: Simulated years in the Van Allen belt converted to Van de Graaf dose and irradiation time of the samples using the Van de Graaf dose rate

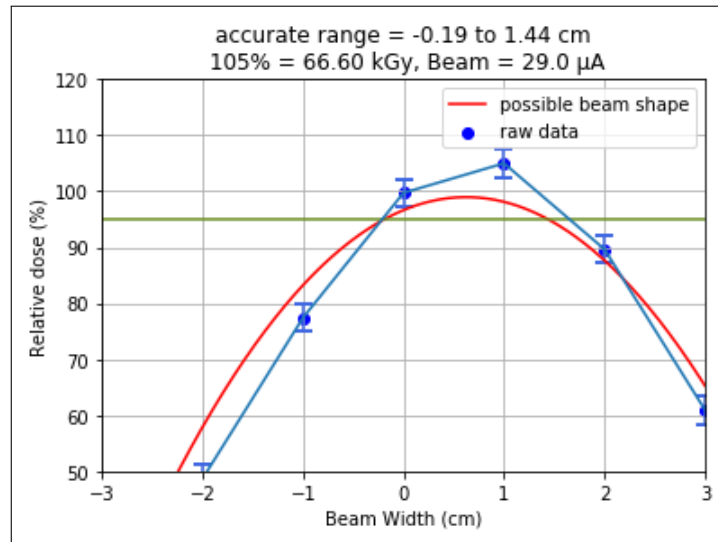


Figure 3.9: Measured dose distribution profile of Van de Graaf accelerator

3.4. Material Characterization

3.4.1. Densification Measurements

The samples' densities were measured using the Archimedes method with the Mettler Toledo AB204-S weight scale. By weighing the object's weight in and outside of distilled water, the density of the samples was calculated using Equation 4.1. Density measurements were conducted before cutting the samples. By dividing the measured density by the theoretical density of ZrB_2 of 6.09 g cm^{-3} , the relative densification was calculated as well. The accuracy of the weight scale was $\pm 0.0001 \text{ g}$, which was carried through the density calculation.

$$\frac{\rho_{object}}{\rho_{water}} = \frac{W_{object}}{W_{displaced\ water}} \quad (3.2)$$

3.4.2. XRD Analysis

X-ray diffraction (XRD) was used for the purchased powder and a crushed sample to determine the amount of impurities present and the lattice parameters. The sample was crushed using a Pulverisette, as seen in Figure 3.10. This was done using a tungsten ball for 5 minutes, after which the sample turned into a fine powder. Subsequently, the powders were inserted into the Rigaku Miniflex 600, as seen in Figure 3.11. This was carried out at 2θ angles between 10° and 90° , with increments of 0.02° . The wavelength of the x-ray radiation was 1.54059 nm . It was assumed that radiation effects that occurred on the surface of the sample would not be visible in XRD after pulverizing. Therefore, XRD analysis was not conducted for irradiated samples.



Figure 3.10: Fritsch Spartan pulverisette



Figure 3.11: Rigaku MiniFlex 600 XRD

3.4.3. SEM Analysis

The surface microstructure of ZrB_2 was examined using a JEOL JSM7000F scanning electron microscope (SEM) seen in Figure 3.12 to investigate if the irradiation had an observable impact. This was accomplished with a sample produced at 2000 °C (Sample 12). In this instance, one-half of the sample received radiation exposure, whereas the other was unirradiated. Using the diamond cutter, the samples were cut into three 5 mm × 5 mm squares, then embedded into an epoxy resin and polished using the procedure shown in Table 3.3. The embedded samples were thereafter sputtered in a 15 nm gold coating and had aluminum foil applied to the sides before being inserted into the SEM.



Figure 3.12: JEOL JSM7000F scanning electron microscope

3.4.4. Thermal Properties

The thermal properties of ZrB_2 investigated in this study were the thermal conductivity and CTE. The thermal conductivity was measured using the Hot Disk TPS 2200 at the Faculty of Civil Engineering, while the CTE was measured using the PerkinElmer thermo-mechanical analyzer (TMA) at the Aerospace Engineering physics laboratory seen in Figure 3.14. The Hot Disk TPS 2200 setup can be seen in Figure 3.13. The disc is slowly heated, and the temperature change at each end of the sample is measured with time. This estimates the thermal conductivity using pre-existing parameters such as the materials' thickness and thermal diffusivity. To measure the thermal conductivity, a reference sample created at $2000\text{ }^\circ\text{C}$ was placed underneath the probe, and the measured sample was placed on top. This was done to allow more conduction from the probe to ensure the heating power could be increased to 800 W. Insulating Styrofoam blocks were placed outside each sample to minimize external thermal influence. Since ZrB_2 is a highly conductive material, it was essential to keep the measurement time low and the heating power high for accurate measurements. The accuracy of the measurements was $\pm 5\%$ as provided by the manufacturer [58].

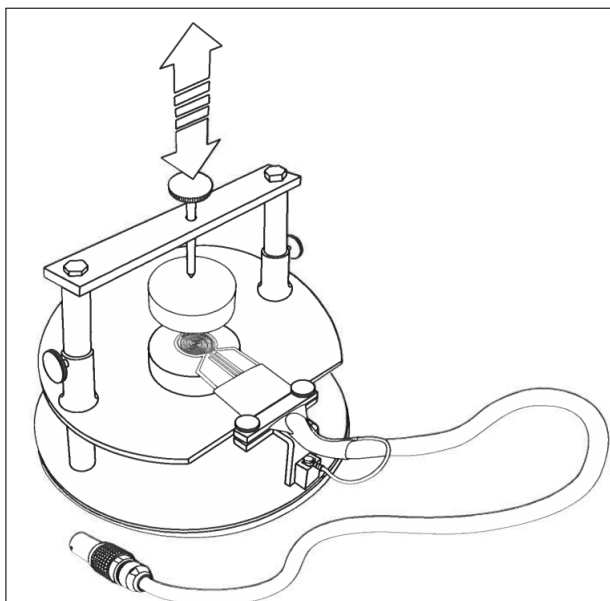


Figure 3.13: Hot Disk TPS 2200 setup



Figure 3.14: PerkinElmer TMA 4000

The CTE was measured using smaller, cut samples of the ceramics to allow for placement in the TMA. The samples were cut 5 mm from the edge of the samples as sketched in Figure 3.15. Inside the TMA, the samples were heated to 600 °C in a Nitrogen environment to avoid oxidation. The CTE was measured between 100-600 °C as this allowed efficient testing of 20 samples with a heating rate of 20 °C/min. The quartz probe was placed on top of the samples with a pre-load of 0.5 N and as the material expanded, the probe was pushed upwards and the displacement was measured. The probe had an accuracy of \pm

0.0005 mm, which gave an uncertainty in the CTE measurement of $\pm 7.07\text{E-}7$ mm.

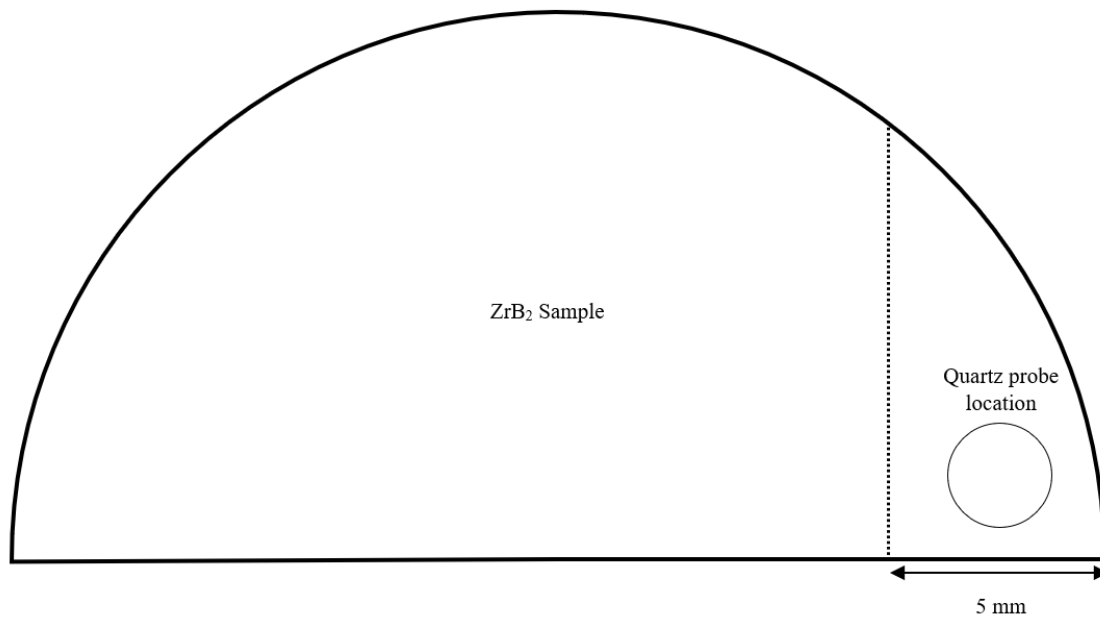


Figure 3.15: Cut location of ZrB₂ samples indicated by dotted line

3.4.5. Surface Roughness

The surface roughness of the samples was characterized using a 3D laser scanning microscope from Keyence. By characterizing the surface, the roughness parameters mean arithmetic roughness, R_a , and maximum roughness, R_z , were measured. Thirty parallel lines were made with lengths of 10 mm to cover the area used for thermo-optical measurements. These were created at the center of the sample as displayed in Figure 3.16.

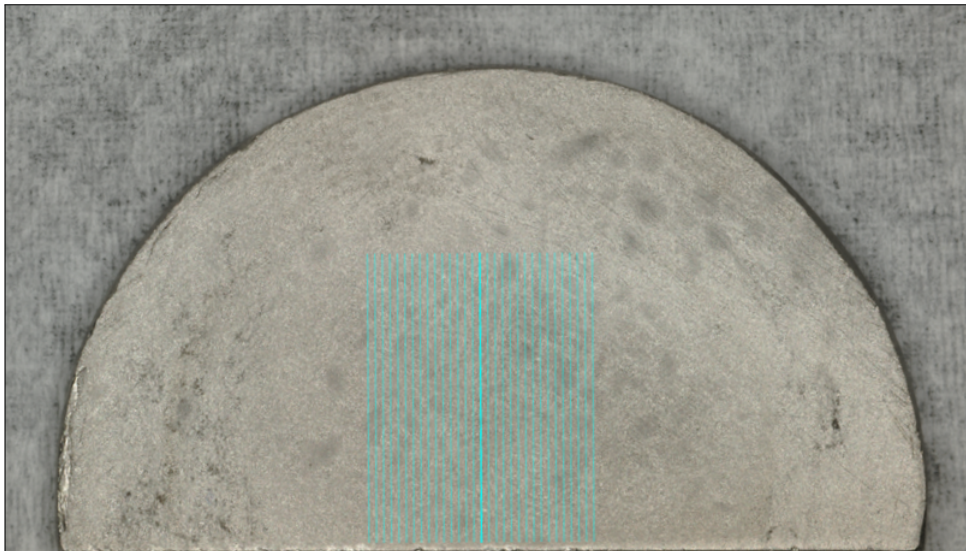


Figure 3.16: Surface roughness lines analyzed with Keyence laser microscope

3.4.6. Optical Properties

The optical properties of the samples measured were the hemispherical emittance and the solar absorptance. This analysis was conducted at ESTEC in Noordwijk with the material science division. The solar absorptance was measured using a spectrophotometer (seen in Figure 3.17) and integrated with the absorption spectrum. Here, the samples are assumed to be perfectly opaque such that the absorption spectra are 1 minus the reflection spectrum. To calculate the solar absorption spectra, the absorption spectra were multiplied by the sun spectrum based on the ASTM E490-00a standard, which is gathered by satellite data. This excludes atmospheric absorptance peaks and has an air mass of zero. The previously multiplied spectra were integrated to arrive at a solar absorptance constant.

Before the samples could be measured, a reference mirror sample with known optical properties was measured, after which no object was placed before the beam. The reference spectrum and background spectrum were used to correct the spectrum of the ZrB_2 samples which was measured between 250-2500 nm. The reflectance spectra for all the ZrB_2 samples can be seen in Appendix B.



Figure 3.17: Agilent UV-VIS-NIR spectrophotometer used for absorptance measurements

The hemispherical thermal emittance of the ZrB_2 samples was measured using the emissiometer shown in Figure 3.18. For the emittance measurements, the device was first calibrated using a standardized metal with known optical properties. Here, the emittance of the material and the background were measured three times each until the value came within 0.05 of the calibration values. Thereafter, the samples were measured three times each. During measurements, it was vital to minimize the temperature fluctuations in the room as this would significantly influence the measurements.

The device measured the directional thermal emittance at angles of 20° and 60° . For each of these angles, the reflectance spectra were integrated at five different wavelength ranges; 2-3.5 μm , 3-4 μm , 4-5 μm , 5-10.5 μm and 10.5-21 μm . From these values, the hemispherical thermal emittance was calculated.



Figure 3.18: ET-100 thermal handheld emissometer

4

Results and Discussion

This chapter presents and discusses the results from analyzing ZrB_2 's material properties. First of all, the pre-irradiation characterization analysis including the densification and XRD measurements is presented. Secondly, the irradiated and unirradiated microstructure of ZrB_2 is compared. After that, thermo-optical results of the irradiated and unirradiated ZrB_2 samples are presented. Lastly, an investigation into the relationship between surface roughness and optical properties is carried out.

4.1. Pre-Irradiation Characterization

4.1.1. Densification Measurements

Table 4.1 lists the densities and relative densification of the ZrB_2 samples. The density measurements yielded unexpected results compared to Figure 2.3. The expected positive correlation between sintering temperature and densification was absent, as seen in Figure 4.1. Additionally, the variation in density with different sintering temperatures is comparable to the error in the measurement device. Likewise, samples made at the same sintering temperature of 2000 °C had a more significant variation in densification than those of differing sintering temperatures. A possible reason for this could be that the polishing routine removed a varying amount of graphite from each sample which would have significantly influenced the density measurement.

$$\frac{\rho_{object}}{\rho_{water}} = \frac{W_{object}}{W_{displaced\ water}} \quad (4.1)$$

Sample	Sintering temperature (°C)	Density (g cm ⁻³)	Densification (%)
1	2000	5.83 ± 0.02	95.79 ± 0.40
2	2000	5.86 ± 0.02	96.14 ± 0.39
3	2000	5.64 ± 0.03	92.65 ± 0.44
4	2000	5.92 ± 0.03	97.19 ± 0.42
5	2000	5.85 ± 0.03	96.08 ± 0.43
6	1800	5.91 ± 0.02	96.98 ± 0.40
7	1850	5.89 ± 0.03	96.64 ± 0.43
8	1900	5.93 ± 0.03	97.38 ± 0.42
9	1950	5.93 ± 0.03	97.44 ± 0.42
10	2000	5.88 ± 0.03	96.63 ± 0.43
11	2000	5.97 ± 0.03	98.02 ± 0.42
12	2000	5.87 ± 0.03	96.37 ± 0.43

Table 4.1: ZrB₂ samples' sintering temperatures, density, and densification

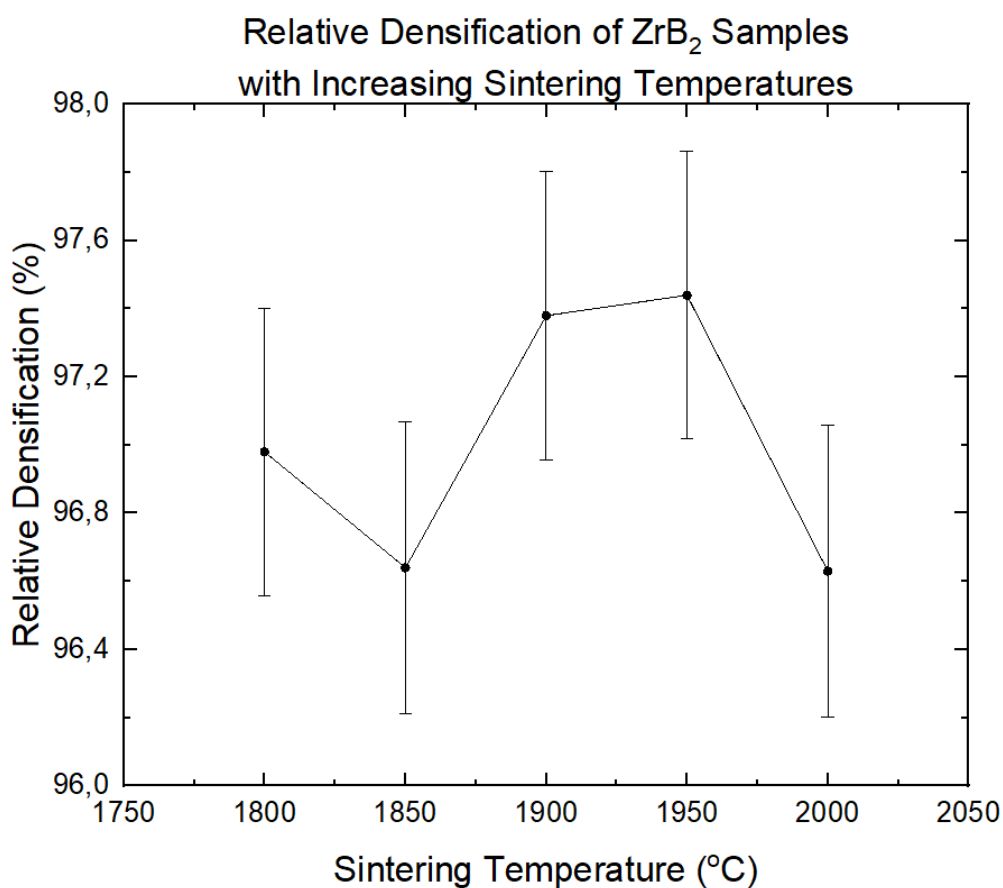


Figure 4.1: Relative densification of ZrB₂ at various sintering temperatures

4.1.2. XRD-Analysis

Figure 4.2 shows the XRD-data of the crushed ZrB₂ samples, raw purchased ZrB₂ powder as well as reference data for ZrB₂ and carbon. It can be seen that the top three patterns closely coincide with each other, signifying no significant impurities in the ZrB₂ sample. However, at some angles, there are minuscule peaks in the crushed sample data (blue), which likely originate from graphite (carbon)

impurities. This can be seen next to the first and third peaks of the crushed ZrB₂ data.

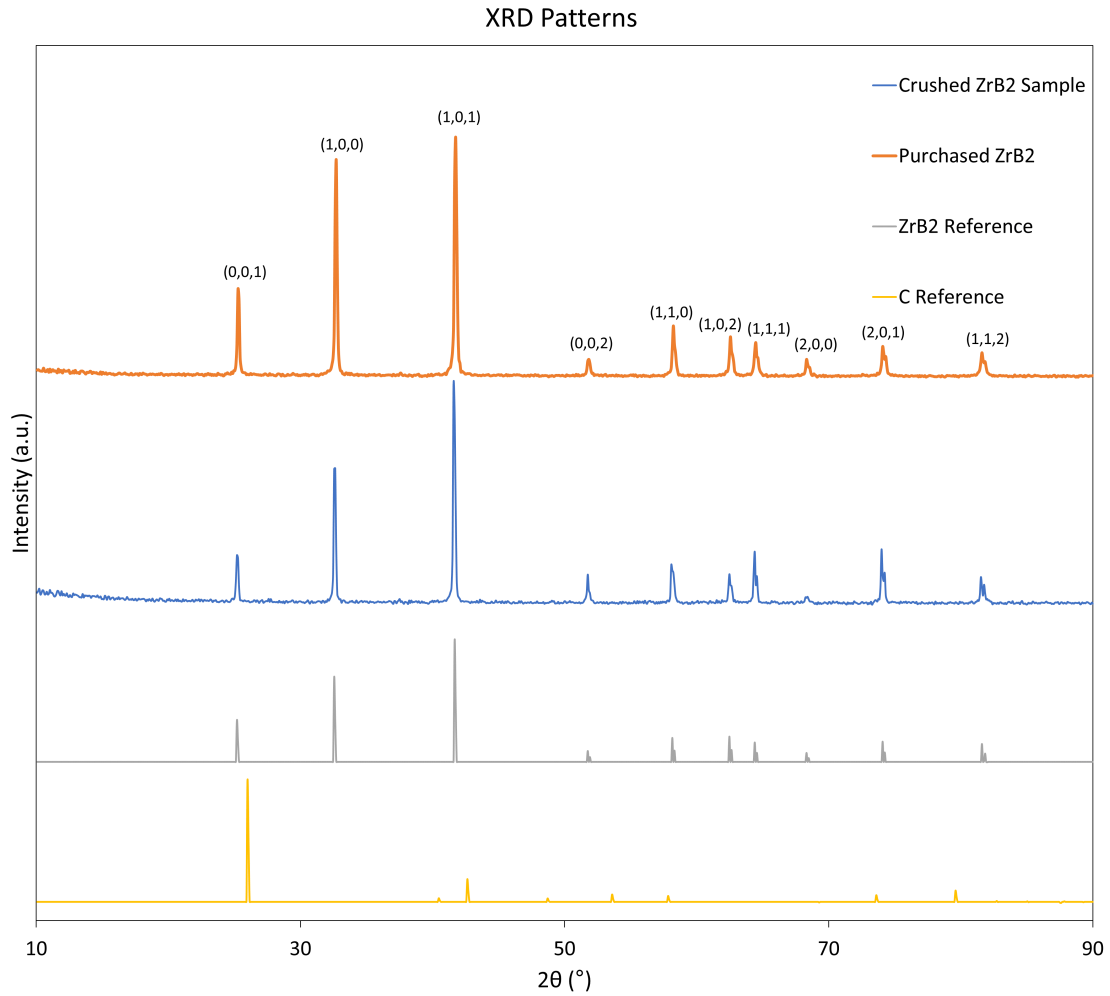


Figure 4.2: XRD pattern of crushed ZrB₂ sample (blue), raw purchased ZrB₂ powder (orange), reference ZrB₂ data (grey) and reference carbon data (yellow)

The peaks in the XRD-data seen in Figure 4.2 were used to calculate the lattice parameters of ZrB₂. This was done by using Equation 4.2, which relates the inter-planar spacing (d_{hkl}) of the crystal lattice to the peak angles found in the XRD pattern (2θ). Here, the wavelength of the x-ray λ and order of diffraction n were also used where the order of diffraction is $n=1$. The peak positions and the calculated inter-planar spacing values are listed in Table 4.2. The peak locations were analyzed through a pseudo-voigt peak fit and to calculate the lattice parameters, Equation 4.3 was used for hexagonal lattices. This was done for various Miller indices of multiple peaks, as seen in Figure 4.2. The XRD data in the present study was compared to reference data in Vesta (Visualisation for Electronic and Structural Analysis). The reference XRD data for ZrB₂ and C can be found in Appendix A and were plotted in Figure 4.2 as well [59] [60].

$$d_{hkl} = \frac{n\lambda}{2 \sin \theta} \quad (4.2)$$

$$\frac{1}{d_{hkl}^2} = \frac{4}{3} \frac{h^2 + hk + k^2}{a^2} + \frac{l^2}{c^2} \quad (4.3)$$

Using the peak locations in Appendix G, the average lattice parameters c and a were calculated to be 3.524 Å and 3.166 Å, respectively. Table 4.3 shows these values are very close to those found with the Vesta software. The uncertainty of these values was based on the standard deviation of the lattice parameters.

Peak Position (°)	Peak Position (Vesta) (°)	(h k l)	Interplanar Spacing d_{hkl} (Å)
25.28	25.20	(001)	3.52
32.66	32.59	(100)	2.74
41.70	41.64	(101)	2.16
51.80	51.74	(002)	1.76
58.22	58.16	(110)	1.58
62.54	62.50	(102)	1.48
64.42	64.38	(111)	1.45
68.32	68.28	(200)	1.37
74.10	74.05	(201)	1.28
81.62	81.56	(112)	1.17

Table 4.2: Peak positions in XRD data and Vesta, and calculated interplanar spacing

Lattice Parameter c (Å)		Lattice Parameter a (Å)	
Calculated Value	Vesta Value	Calculated Value	Vesta Value
3.524 ± 0.004	3.531	3.166 ± 0.001	3.169

Table 4.3: Calculated lattice parameters c and a

4.2. Microstructure SEM Analysis

SEM was used to analyze the two halves of Sample 11 to investigate whether microstructural changes in ZrB_2 occurred after irradiation. They were produced at 2000 °C, one was unirradiated, and the other was exposed to irradiation at a fluence of $1576.9 \cdot 10^{11} \text{ e}^- \text{ cm}^2$ (equivalent to 50 years of outer Van Allen belt radiation).

The following figures (Figure 4.3, 4.4, 4.5) display 400 X magnified (light emitting microscope (LEM)) and 10,000 X (scanning electron microscope (SEM)) magnified images of the border of unirradiated ZrB_2 samples. Because the images are looking at the border in the vertical plane (since this is equivalent to the irradiation surface of the irradiated half) the border is not in complete focus. In Figures 4.3 and 4.5, the surface is smooth with some ZrB_2 grains visible in the 10,000 X magnified images. In Figure 4.4, a significant amount of ZrB_2 grains are visible on the surface, indicating a rougher surface as the level of polishing was not consistent across the various borders.

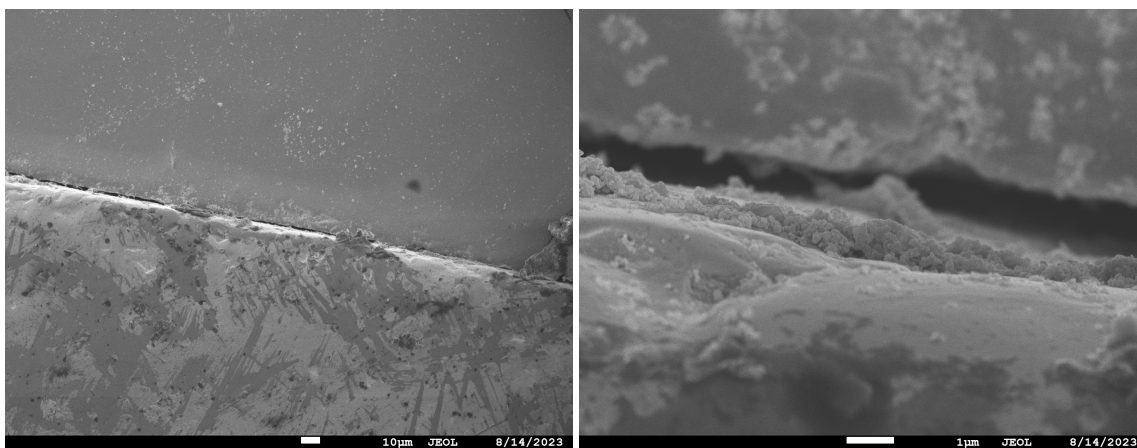


Figure 4.3: Left: LEM 400 X image of the unirradiated sample. Right: SEM 10,000 X image of the unirradiated sample.

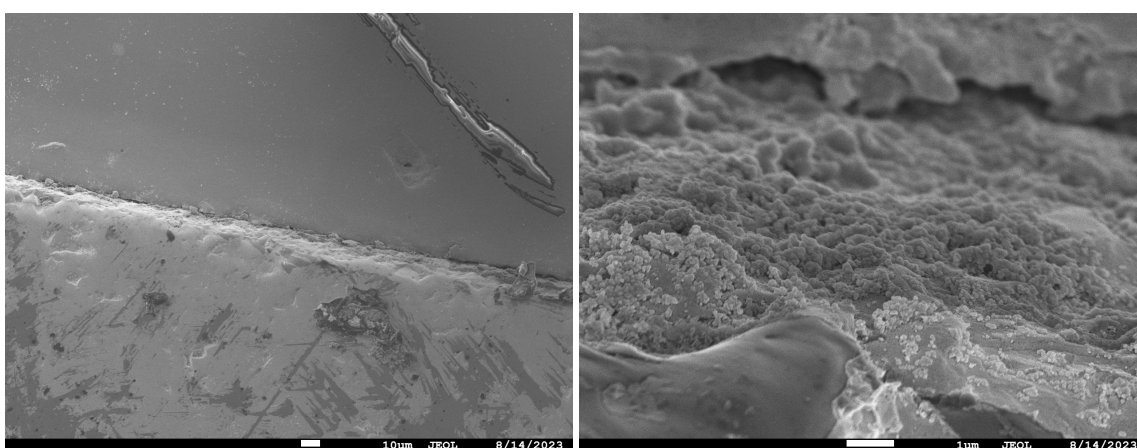


Figure 4.4: Left: LEM 400 X image of the unirradiated sample. Right: SEM 10,000 X image of the unirradiated sample.

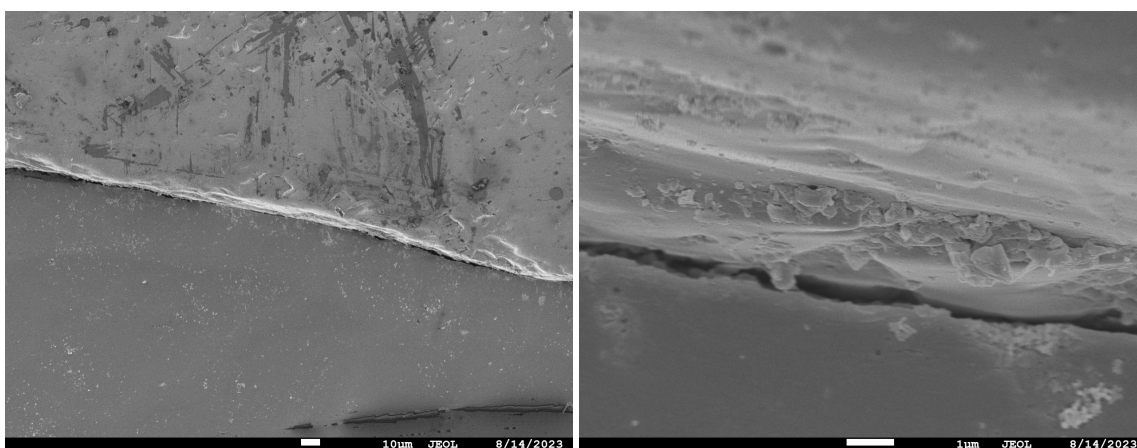


Figure 4.5: Left: LEM 400 X image of the unirradiated sample. Right: SEM 10,000 X image of the unirradiated sample.

Figures 4.6, 4.7, and 4.9 show images of the borders of the irradiated samples (irradiated ZrB_2 on the right side and epoxy resin on the left). Except for Figure 4.6, no apparent difference between these borders and those of the unirradiated samples can be seen. Again, there are ZrB_2 grains visible in

clusters on a generally smooth surface with some troughs. However, Figure 4.6 shows a unique structure protruding from the sample. This could be a result of damage accumulated during the handling process after irradiation, or a result of poor polishing.

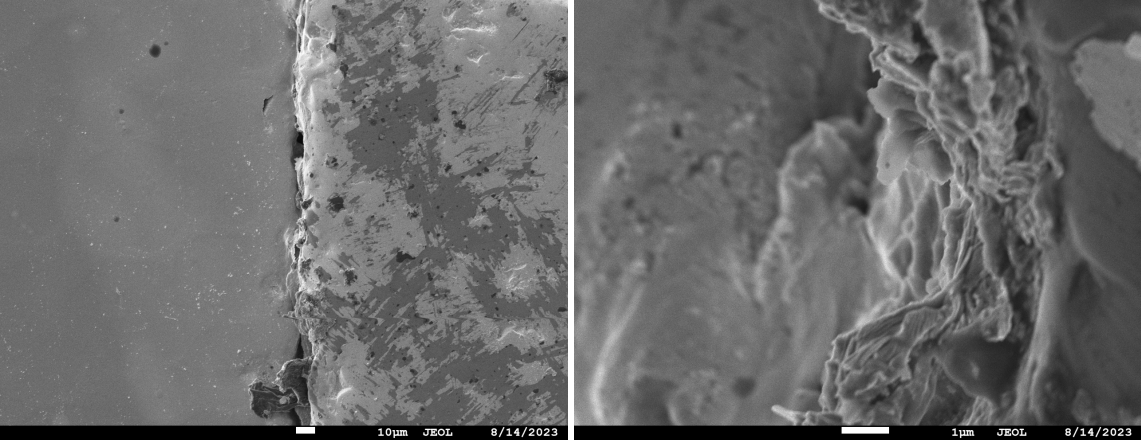


Figure 4.6: Left: LEM 400 X image of the irradiated sample. Right: SEM 10,000 X image of the irradiated sample.

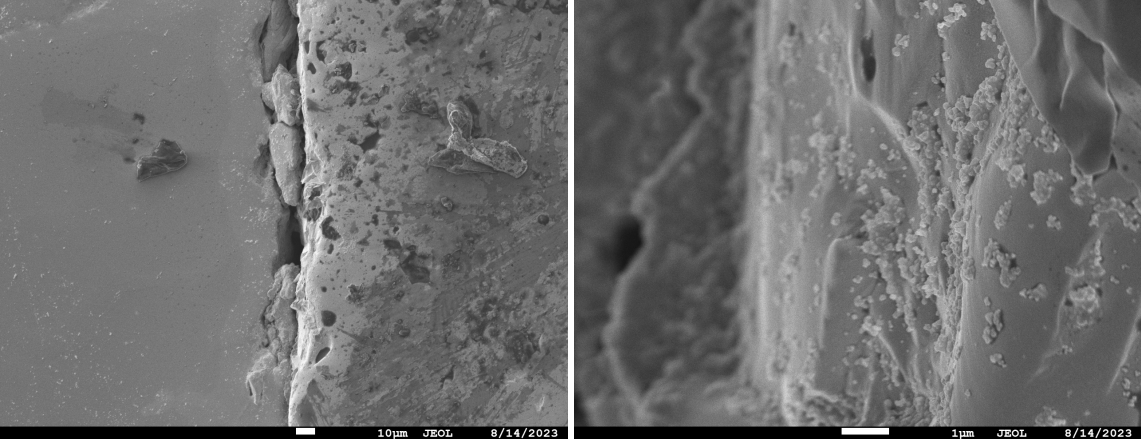


Figure 4.7: Left: LEM 400 X image of the irradiated sample. Right: SEM 10,000 X image of the irradiated sample.

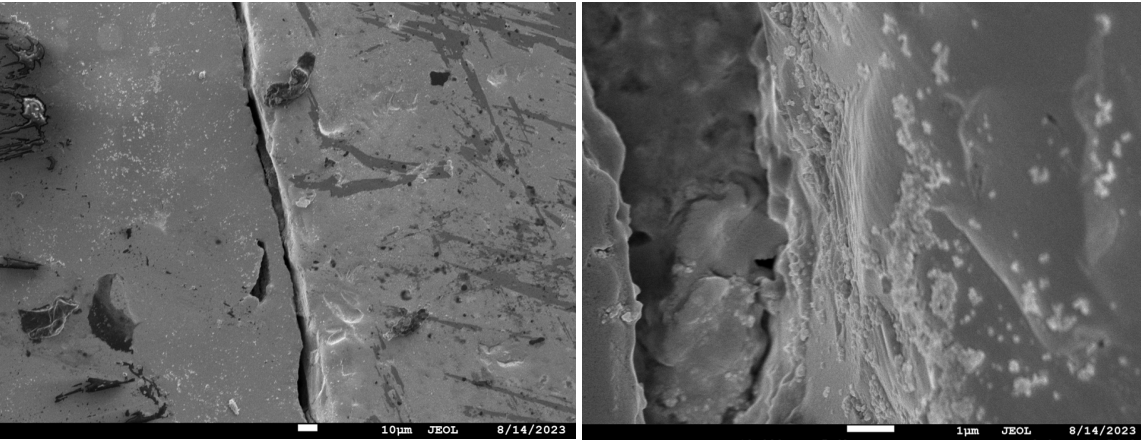


Figure 4.8: Left: LEM 400 X image of the irradiated sample. Right: SEM 10,000 X image of the irradiated sample.

The following two images depict SEM images with 100,000 X magnification of an irradiated and unirradiated sample. This was done to analyze if changes could be detected at a nanometer scale. Here, detailed grain structures can be seen on the border of the ZrB_2 samples. The particular cluster of ZrB_2 grains on the irradiated sample is much larger than the unirradiated sample. However, no apparent difference between the grains was seen in these images. The diameter of the grain structures for the irradiated and unirradiated were measured using ImageJ. The following table (Table 4.4) lists the average grain size on the border's surface calculated from 10 grains per image for each cut sample. On average, the irradiated grain size was 88.69 nm, whilst the unirradiated grain size was 92.96 nm. However, following a large standard deviation, the difference in grain size is negligible.

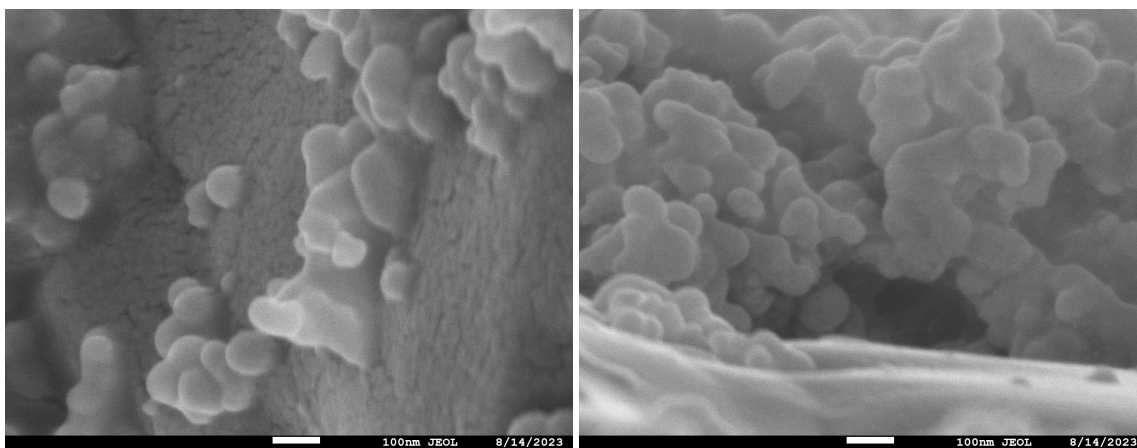


Figure 4.9: Left: SEM 100,000 X image of the irradiated sample. Right: SEM 100,000 X image of the irradiated sample.

Irradiated ZrB_2 grain size (nm)	Unirradiated ZrB_2 grain size (nm)
84.63	91.956
83.35	89.891
98.094	97.046

Table 4.4: Grain sizes of irradiated and unirradiated ZrB_2 samples

Based on the SEM images provided in this report and the probing of the border with the SEM, no distinct microstructural damage of ZrB_2 from irradiation was observed. In contrast, a previous Helium radiation study of ZrB_2 observed microstructural changes in transmission electron microscope (TEM) images as seen in Figure 4.10. Here, ripple and pore structures on the surface were seen through different magnification levels. Such structures were not seen with electron irradiation. The pores in the study were thought to be caused by the insolubility of He ions, which clustered together on the surface [53]. At the same time, the ripples are standard ion bombardment features when the ion beam is impinging on an angle, as observed with Xenon ion bombardment of silicon [61]. It is also important to note that the temperature could have influenced the size of these morphology changes, which was not explored with electron irradiation. It was expected that some damage would be visible in SEM images, but that it would be less evident than that observed in ion irradiation. A reason for why no damage was seen, could be that the radiation might have caused effects through electron sputtering, but it was too minuscule to observe. Also, due to the presence of metallic bonding in ZrB_2 , free electrons replace electrons split from their atom which could have annealed the radiation damage [45].

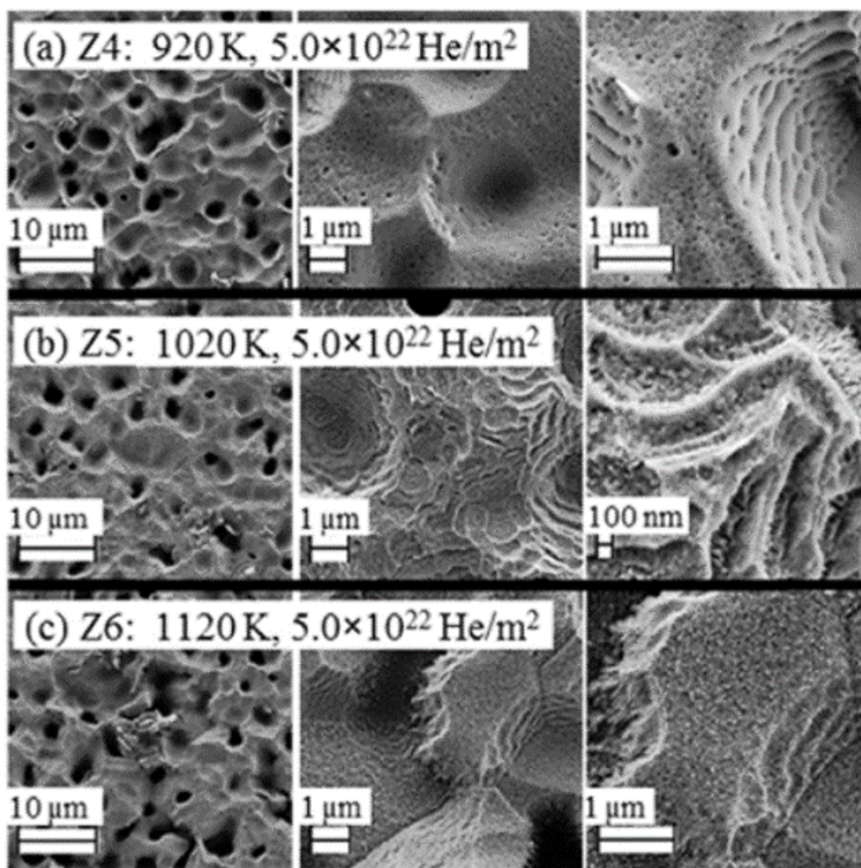


Figure 4.10: TEM images of helium-irradiated ZrB_2 under different temperatures [53]

4.3. Thermal Conductivity

The average thermal conductivity of three measurements per ZrB_2 sample can be seen in Appendix D. Measurement parameters set in the Hot Disk, and the resulting conductivity and diffusivity for Sample 5 UI are shown in Table 4.5. The heating power, measurement time, and temperature remained constant throughout the measurements, to ensure a controlled experiment. Figure 4.11 displays the thermal conductivity of the ZrB_2 samples under varying levels of irradiation doses. First, it can be seen that the thermal conductivity values are low compared to those of the literature presented earlier in the report. Nonetheless, literature-reported values are as low as $56 \text{ W m}^{-1} \text{ K}^{-1}$ [62]. However, it could also have been due to significant errors in the measurement method. Since the temperature range from which the thermal conductivity was calculated was subjectively selected from the graph in Appendix E, the results were not consistent for each test.

Additionally, it can be observed that the thermal conductivity was higher for the medium and highest irradiation dose compared to the lowest dose. However, given the significant measurement errors, and the large discrepancies in thermal conductivity at the same irradiation dose, these changes were not representative of a trend. Snead, Zinkle, and White investigated neutron irradiation of various ceramics and found that thermal conductivity decreased with increasing doses [63]. This was the expected result of the present study and coincides with what is found in other literature as well [47][54]. However, neutrons and electrons have different interactions with materials due to the charge, indistinguishability, and significantly smaller mass of electrons. It is possible that the electron irradiation damage did not cause sufficient disorganization and defects of the crystal lattice to influence the thermal conductivity of ZrB_2 .

Temperature	Thermal Conductivity	Thermal Diffusivity	Heating Power	Measurement time
21	51.68	6.187 mm ² /s	800	2.5 s

Table 4.5: Hot Disk calculated values and parameters for sample 5 UI

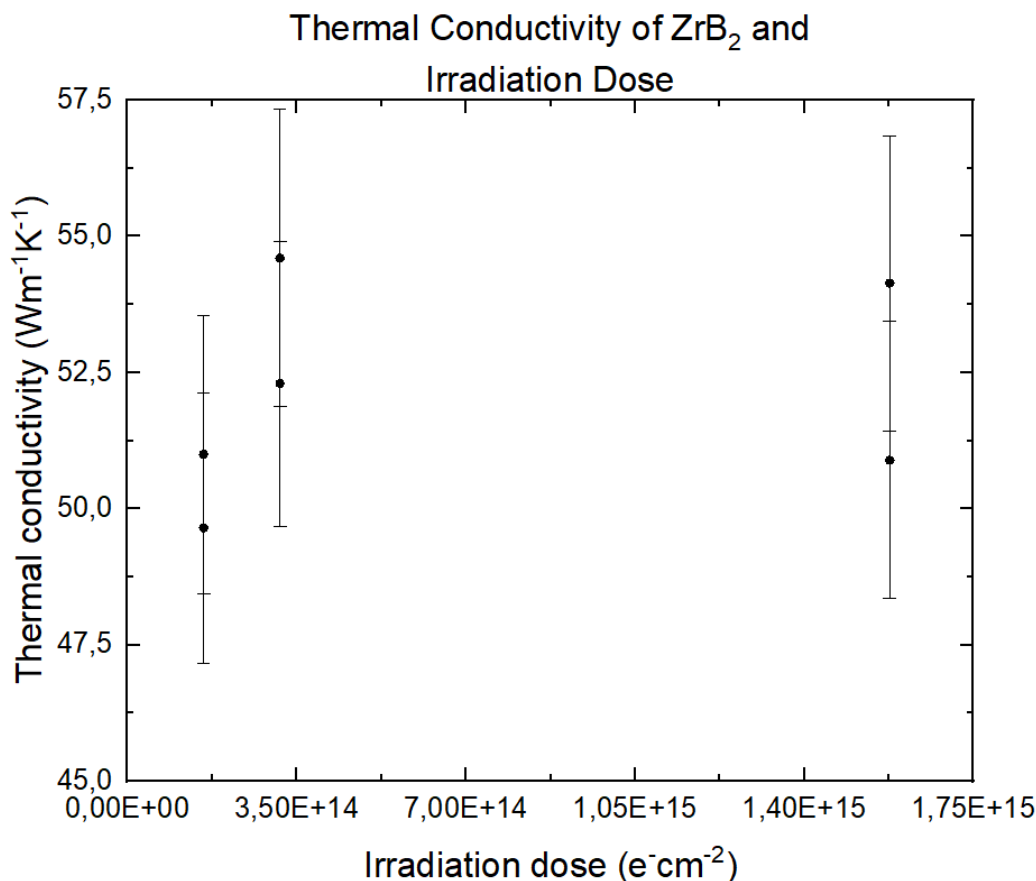


Figure 4.11: Thermal conductivity versus irradiation dose of ZrB₂

Figure 4.12 displays the thermal conductivity of the irradiated and unirradiated ZrB₂ samples produced under varying sintering temperatures, where the irradiated samples were exposed to the same irradiation dose of $157.7 \cdot 10^{11} \text{ e}^- \text{ cm}^2$. If Sample 6 UI is treated as an outlier, there is a negative relationship between thermal conductivity and sintering temperature. This was the expected outcome, as it was expected that with higher sintering temperatures, there was a higher density and, hence, lower conductivity. However, the density measurements showed no such relationship, which might indicate that other bulk properties of the UHTC such as grain size changed with higher sintering temperatures. Due to possible impurities of graphite, the density measurements did not reflect this difference. Additionally, in Figure 4.13, there is no relationship between the measured density of the samples and the thermal conductivity.

Furthermore, the irradiation did not influence the results of samples with various sintering temperatures differently. The irradiated ZrB₂ samples had a higher thermal conductivity for two temperatures, whereas, for the other three temperatures, the unirradiated samples had a higher conductivity. Therefore, there was no clear improvement in the radiation resistance property of ZrB₂'s thermal conductivity as a result of increasing sintering temperature.

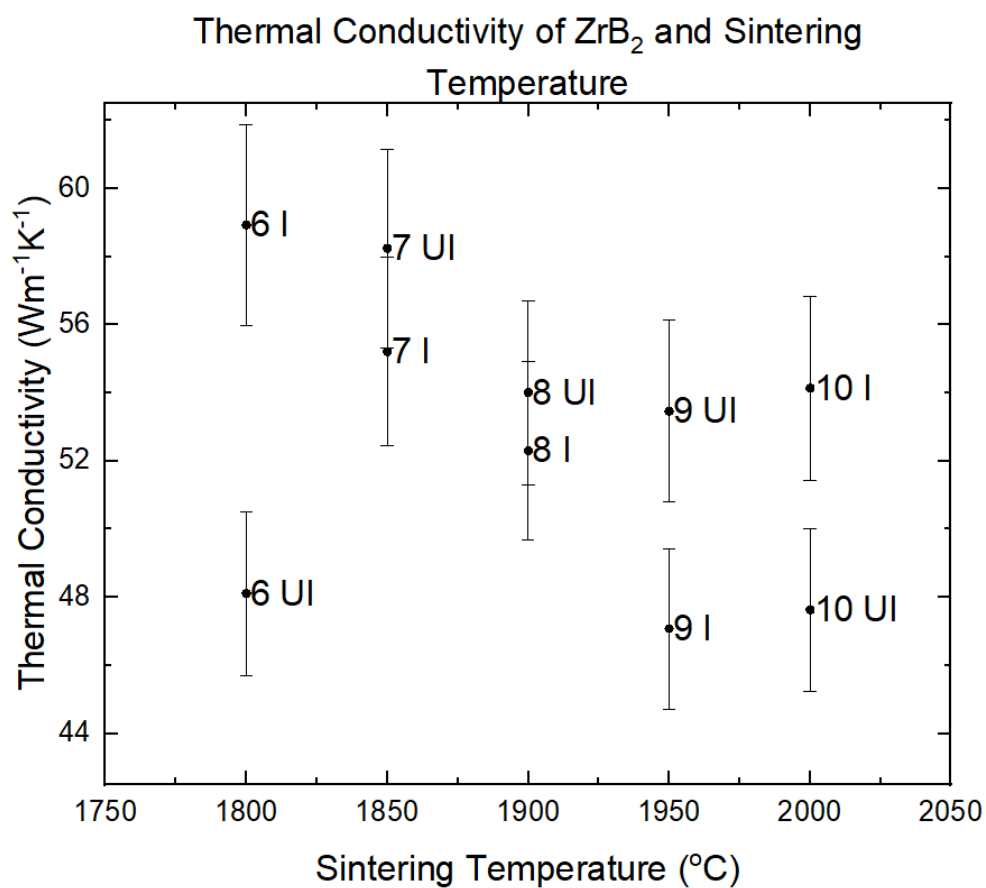


Figure 4.12: Thermal conductivity versus sintering temperature of ZrB₂

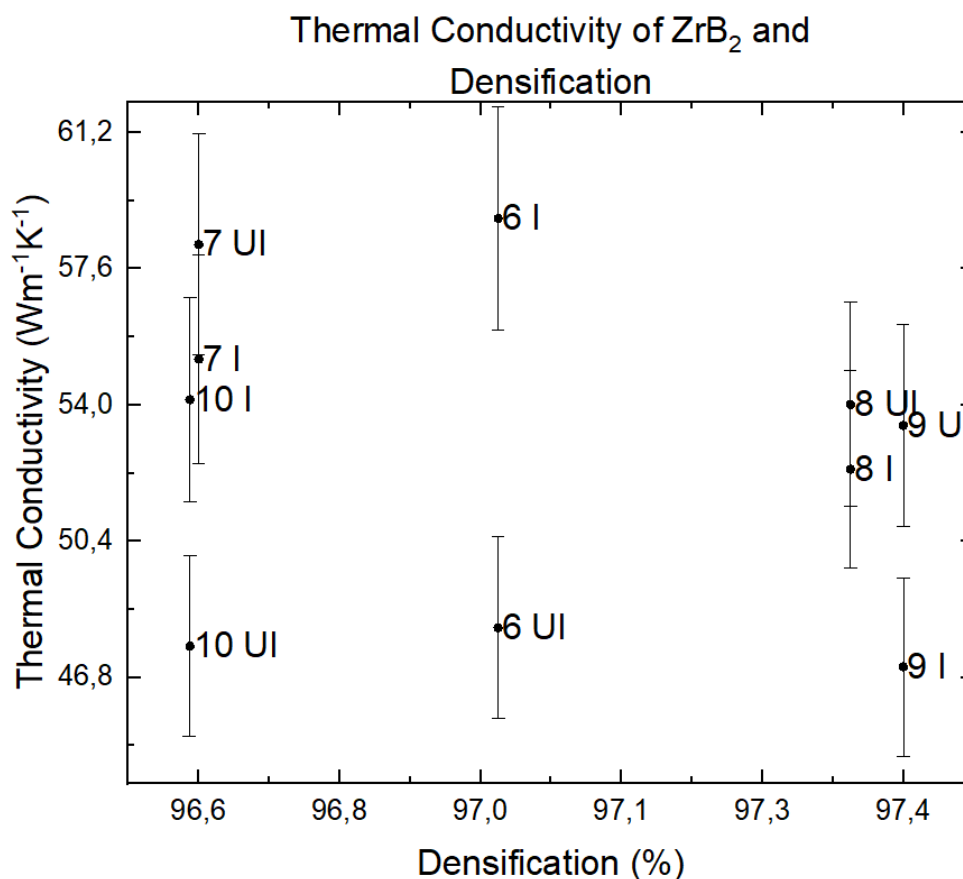


Figure 4.13: Thermal conductivity versus densification percentage of ZrB₂

4.4. Coefficient of Thermal Expansion

Figure 4.14 displays the temperature and the maximum z-position of the ZrB₂ sample during the TMA analysis. It can be observed that the z-position does not follow a strictly linear relationship with time or temperature. This is likely due to slight changes in the CTE under heating that have been observed in previous literature, where the CTE of ZrB₂ tends to increase with temperature [22]. The raw tabulated data of the CTE measurements are listed in Appendix C. Using this data, the CTE was plotted against the irradiation dose levels in Figure 4.15 and the sintering temperature in Figure 4.16. Due to the low CTE of Sample 10 UI, it can be neglected in these results and attributed to a measurement error.

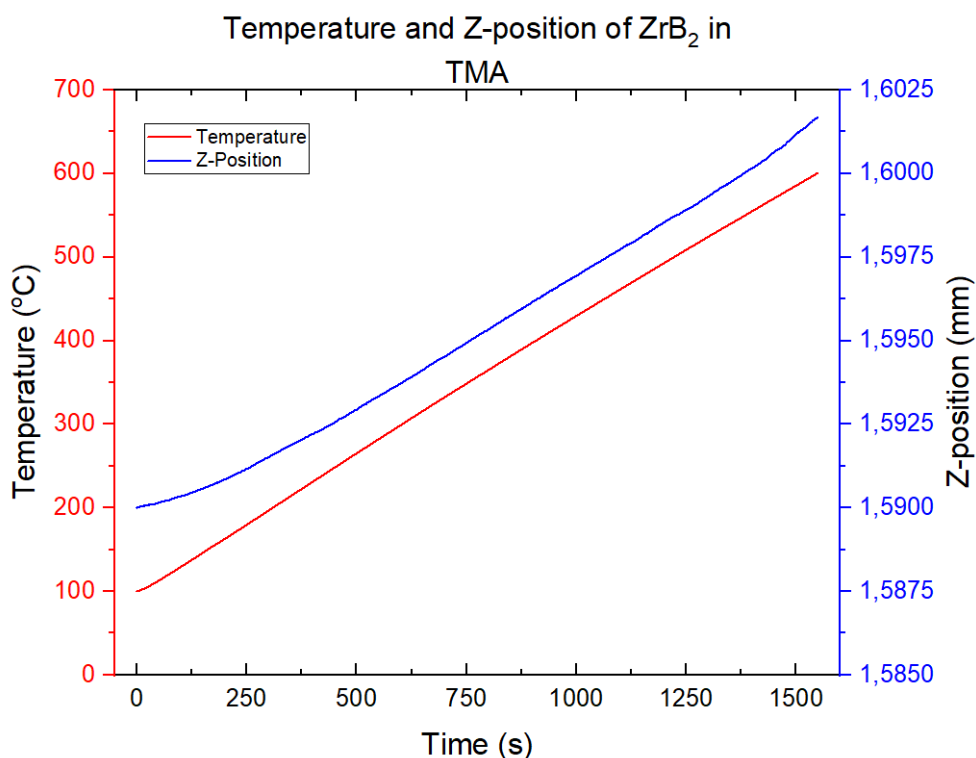


Figure 4.14: Temperature and time of Sample 5 I in TMA

The data in 4.15 displayed no relationship between the CTE and irradiation dose levels, contradicting the expected positive relationship. Initially, the CTE decreases when the dose increases to the medium dose level, then decreases for samples exposed to the maximum dose level. In addition to this, the difference between the CTE of two samples under the same irradiation environment decreases with increasing irradiation dose. The variance between the CTEs of samples under the same irradiation doses was more significant than the change between doses as well. This indicates a more significant structural difference between samples produced at the same temperatures and irradiated with the same doses or a measurement error in the CTE measurement. More considerable structural differences between the samples could be due to the various graphite impurities from the production phase. It is also important to note that the CTE measurements in the TMA require heating, which could anneal the damage caused by irradiation.

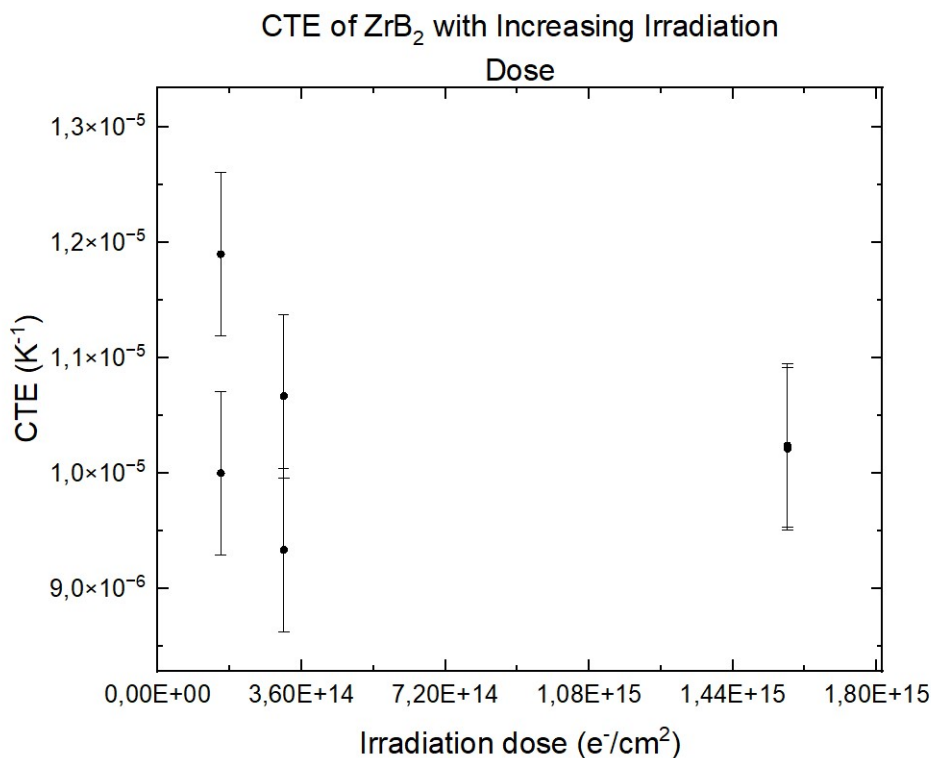


Figure 4.15: CTE versus electron irradiation dose of ZrB₂

There was no relationship observed between the sintering temperature and CTE. This contradicted the expected result of a decreasing thermal expansion as the sintering temperature increased, due to an expected increase in density. On the other hand, Figure 4.17 displays the CTE of the ZrB₂ samples versus their relative densification. It can be observed that with higher densifications, the CTE is lower. In some cases, such as for Sample 7, the difference between the CTE of irradiated and unirradiated samples was significantly larger. This contradicted the expected result of a decreasing thermal expansion coefficient as the densification increased. Again, a reason for this result could be the presence of graphite impurities in the ZrB₂ samples. There was also no radiation resistance effect of the changing sintering temperature or density on the CTE.

A limited number of studies have investigated the influence of irradiation on the CTE of ceramics. However, Higby et al. examined the CTE of various glass-ceramic and ceramic materials such as ultra-low expansion (ULE) glass, SiO₂, and SiC under 10 MeV electron radiation. It was found that simple ceramic materials had less radiation response than more complex materials such as Zerodur and Astrositall whose CTE decreased under radiation. In this case, the CTE was measured using a Michelson interferometer between 180 K to 300 K, which was significantly narrower than the range used in the present study. Additionally, the study only measured the change in CTE between irradiated and unirradiated samples, and not with increasing dose levels. This prohibits the paper's ability to draw a conclusion on the relationship between CTE and radiation dose [64].

A cause of the lack of observable damage in the bulk thermal properties (thermal conductivity and CTE) of ZrB₂ could be that the electron irradiation was carried out in a room-temperature environment. Figure 4.18 displays the induced damage of various irradiation types on stainless steel, where it can be seen that electron irradiation requires a higher temperature to cause radiation-induced segregation compared to its heavier particle counterparts [38]. Additionally, NASA has reported that electron irradiation fluences

below $10^{18} \text{ e}^- \text{ cm}^{-2}$ do not cause significant degradation to structural and thermal properties of metals or ceramics [65]. However, the report fails to provide experimental data to support this claim, which could be due to its maturity or security reasons. Nonetheless, this fluence is nearly 1000 times the highest dose level that was simulated in the present study and would represent about 50,000 years in the outer Van Allen belt. This level of space radiation was not relevant for current space missions and it was not realistic to recreate in a Van de Graaf accelerator.

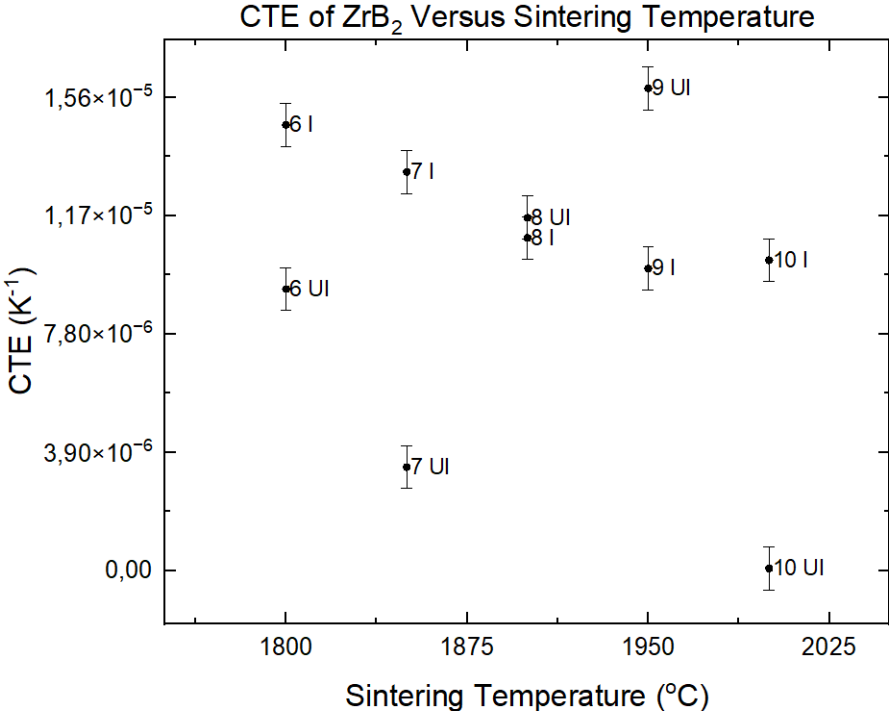


Figure 4.16: CTE versus sintering temperature of ZrB₂

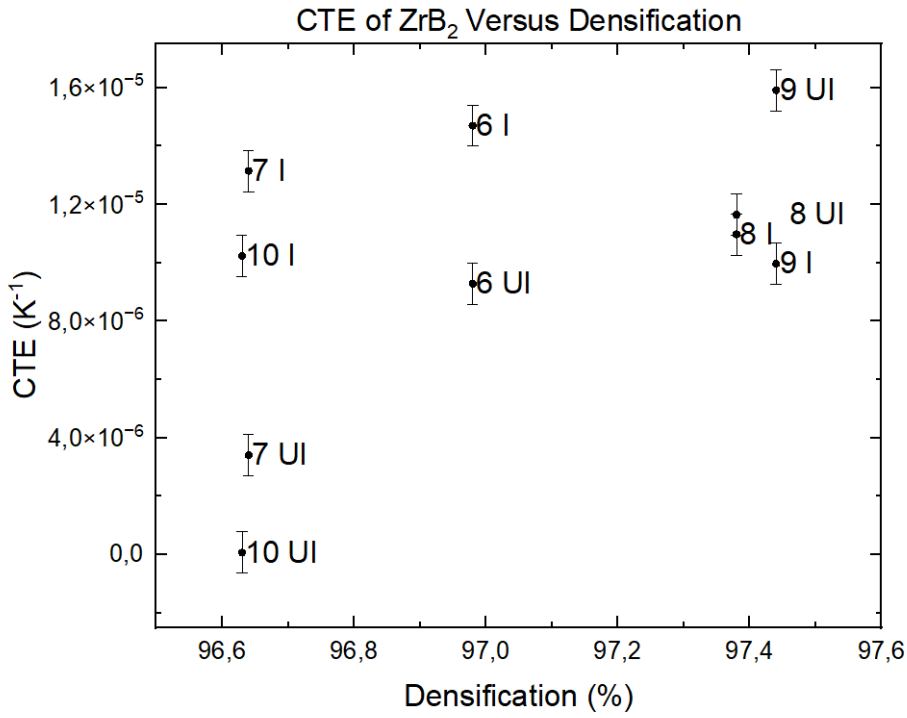


Figure 4.17: CTE versus densification percentage of ZrB₂

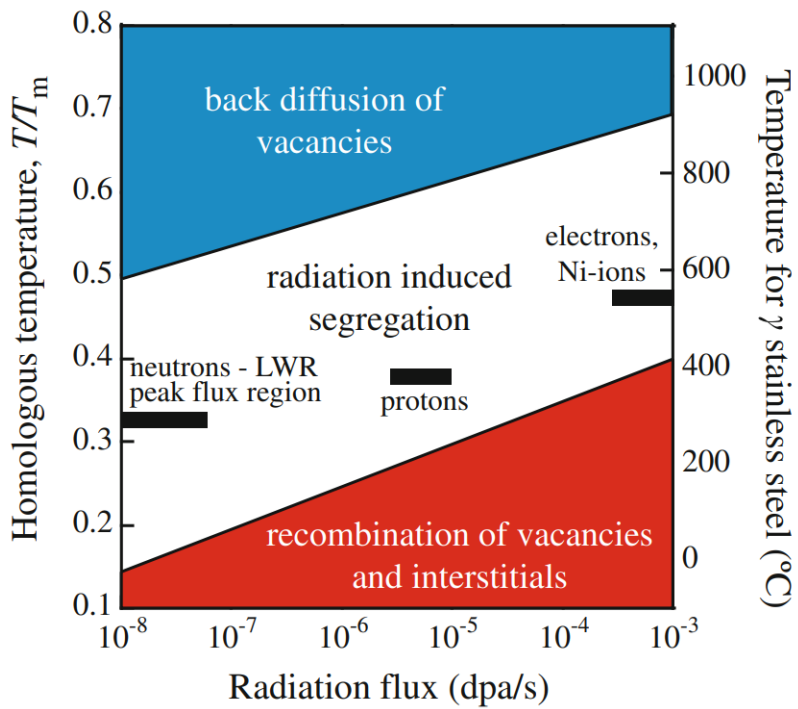


Figure 4.18: Temperature and dose rate of neutron, proton, electron and nickel irradiation and radiation-induced segregation [38]

4.5. Surface Roughness

This section presents the results from the surface analysis of the ZrB_2 samples which includes the roughness measurements using the laser microscope, which produced profiles as seen in Figure 4.19. Table 4.6 lists the arithmetic mean roughness R_a and maximum roughness R_z of the unirradiated and irradiated ZrB_2 samples. The uncertainty values were calculated by dividing the standard deviation, S , by the square root of the number of data points, N (30), as seen in the following equation:

$$\sigma = \frac{S}{\sqrt{N}} \quad (4.4)$$

From Table 4.6, it can be seen that R_a values fell between values of 0-2 μm , while the R_z values fell between values of 5-20 μm . The R_a values are ideal for comparing the surfaces between two samples and ideally, the R_z values would be more similar. However, in this case, some were significantly larger than others, indicating large gaps/troughs likely caused by more profound scratches/valleys not smoothed by polishing. From the table, it was calculated that the R_a values were 29% higher on average for the unirradiated samples than the irradiated samples. This could indicate a smoothing surface effect from electron sputtering, but it can also be seen that increasing doses do not have such an effect in Figure 4.20.

Sample	R_a (μm)	R_z (μm)	Irradiated Sample	R_a (μm)	R_z (μm)
Sample 1	1.47 ± 0.03	12.43 ± 0.72	Sample 1	1.70 ± 0.03	13.60 ± 0.92
Sample 2	1.91 ± 0.05	12.7 ± 0.80	Sample 2	1.51 ± 0.04	10.4 ± 0.25
Sample 3	1.87 ± 0.03	13.18 ± 0.34	Sample 3	1.36 ± 0.02	10.98 ± 0.29
Sample 4	1.29 ± 0.02	7.20 ± 0.19	Sample 4	0.86 ± 0.01	7.00 ± 0.30
Sample 5	2.01 ± 0.02	18.04 ± 0.73	Sample 5	1.23 ± 0.01	8.19 ± 0.36
Sample 6	1.45 ± 0.04	10.20 ± 0.65	Sample 6	1.47 ± 0.03	9.29 ± 0.51
Sample 7	1.03 ± 0.01	5.43 ± 0.17	Sample 7	1.16 ± 0.05	6.24 ± 0.23
Sample 8	2.58 ± 0.09	11.95 ± 1.11	Sample 8	0.67 ± 0.02	5.73 ± 0.21
Sample 9	2.28 ± 0.04	8.09 ± 0.54	Sample 9	1.05 ± 0.02	6.96 ± 0.35
Sample 10	1.35 ± 0.04	10.18 ± 0.83	Sample 10	1.24 ± 0.02	8.99 ± 0.39

Table 4.6: Arithmetic mean roughness and maximum roughness of unirradiated and irradiated samples

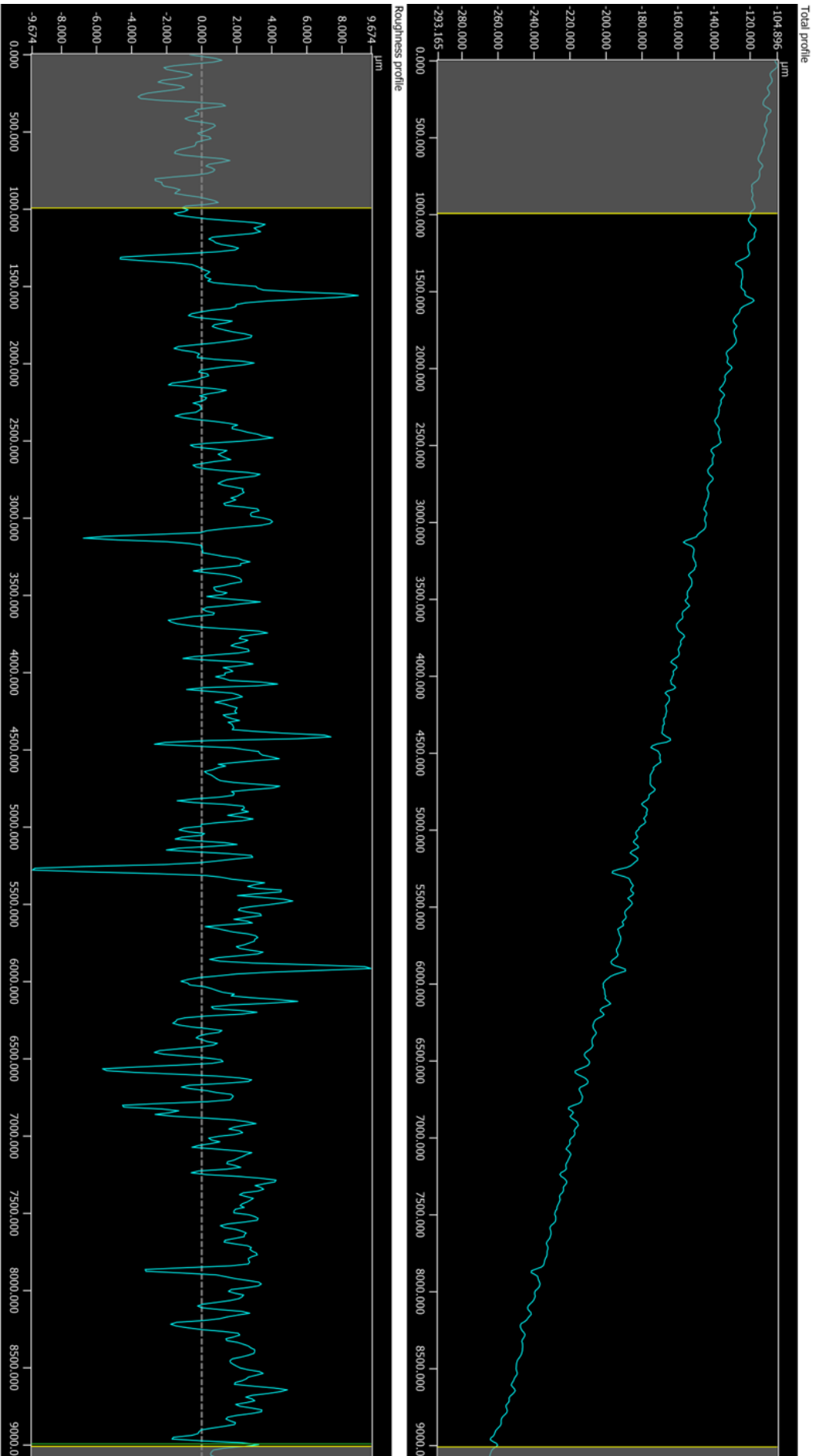


Figure 4.19: Total profile and roughness profile of Sample 5 UI

Figure 4.20 displays the R_a of the irradiated samples against the irradiation dose. This is only plotted for samples produced at the same sintering temperature of 2000 °C. No apparent influence on R_a can be observed from the three irradiation doses tested. Similarly, to the thermal property measurements, within the same irradiation dose (see $3.15E14 \text{ e}^-/\text{cm}^2$), there was a more significant change in R_a than with increasing doses. Limited research has investigated the influence of irradiation on the surface roughness of materials, and none with ZrB_2 . In the study by Carter and Vishnyakov, it was found that silicon had a significantly lower surface roughness under normal incidence Xe^+ -ion irradiation compared to irradiation with incidence angles between 0-40° [61]. Although surface roughness values were lower for irradiated samples in the present study, it is unlikely that this is caused by irradiation. The irradiation would have caused larger-scale damage to the surface of ZrB_2 which should have been visible in SEM imaging after irradiation. Therefore, this is likely a result of inconsistent polishing.

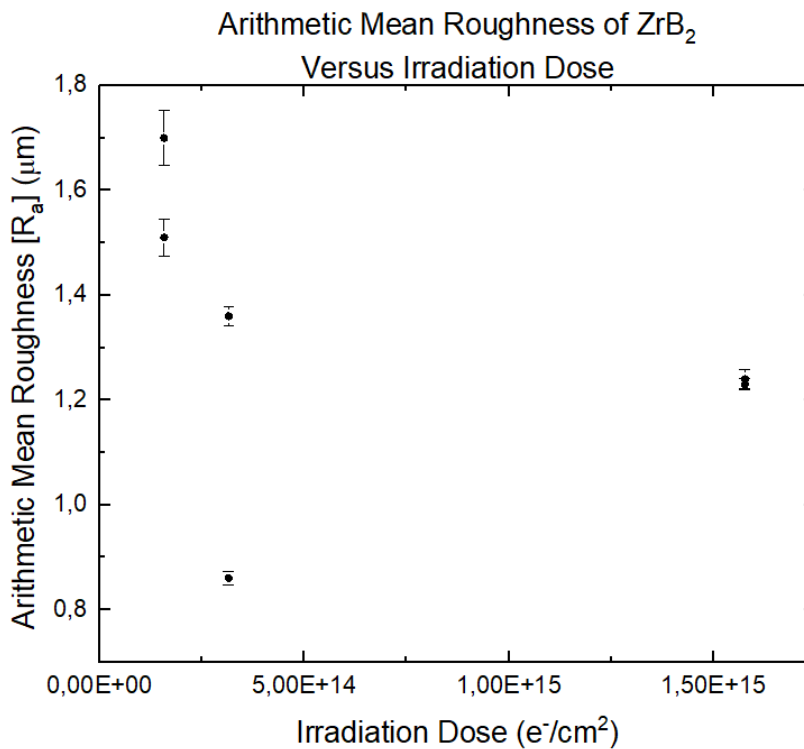


Figure 4.20: Arithmetic mean roughness and irradiation dose

4.6. Optical Measurements

The optical properties that were measured were the hemispherical thermal emittance and solar absorptance. Table 4.7 lists the directional thermal emittance at 20° and 60° as well as the hemispherical thermal emittance for the unirradiated and irradiated ZrB_2 samples. Appendix B lists the raw data used to calculate the emittance values. On the other hand, Appendix B displays the reflectance spectrum used to calculate the solar absorptance values. Figure 4.21 displays the solar absorptance and hemispherical thermal emittance of the ZrB_2 samples exposed to various irradiation doses. For easier clarity in the data visualization, error bars have been excluded from this image (± 0.05 for emittance and ± 0.03 for absorptance), but the upper and lower uncertainty levels are visualized. This was determined by the upper uncertainty of the lowest data points and the lower uncertainty of the highest data points. From this, it can be seen that the most extreme data points overlap each other, signifying the large errors relative to the fluctuation of the data.

Hemispherical thermal emittance readings were lower than expected when compared to literature values. They frequently fell below 0.10, but literature values have ranged as high as 0.18. The absorptivity measurements are also higher than expected. The values ranged between 0.54 and 0.61, while a reported value in the literature was 0.47 [26]. The differences in optical readings could be attributed to embedded graphite, polishing, or different synthesis procedures.

There was no significant influence on the optical properties of the increasing electron radiation dosage for the three doses studied. It is worth noting that the fluctuation in optical characteristics did not exceed the measurement devices' accuracy values. All the data points fell between the upper and lower uncertainty levels. On the other hand, the existing study that explored proton irradiation onto olivine observed a shift in the reflectance spectrum [49]. Since there are numerous differences between the present study and that (material used, irradiation particle, particle energy, particle fluence), it is difficult to pinpoint the reason why such an effect was not observed in this case. However, a previous study also witnessed a color change in ZrB_2 under Helium irradiation, which would coincide with a change in absorption properties in the visual spectrum range [53]. In this case, the irradiation energy was 30 keV, but the radiation fluence was significantly higher with values such as $8.4 \cdot 10^{21}$ He/m² and $5 \cdot 10^{22}$ He/m². The main difference between these studies and the present study was the use of heavier ion and neutron irradiation at higher doses instead of electron irradiation, which causes significantly more damage to the material. Therefore, the absence of ion implantation and ion sputtering could be contributing factors as to why there was no damage to the optical properties by electron irradiation. Additionally, the electron could have caused damage deeper in the ZrB_2 samples and limited damage on the surface. As seen with electron irradiation in Figure 2.10, the peak in the longitudinal energy deposition occurs after penetrating the surface, signifying more severe damage at this depth [66].

Sample	Unirradiated ZrB_2			Irradiated ZrB_2		
	DTE 20	DTE 60	HTE	DTE 20	DTE 60	HTE
1	0.10	0.11	0.12	0.07	0.08	0.09
2	0.07	0.08	0.08	0.08	0.08	0.09
3	0.07	0.07	0.08	0.08	0.08	0.10
4	0.08	0.09	0.10	0.09	0.09	0.11
5	0.04	0.06	0.05	0.07	0.07	0.09
6	0.07	0.11	0.09	0.09	0.10	0.11
7	0.06	0.07	0.07	0.06	0.07	0.08
8	0.09	0.11	0.11	0.08	0.10	0.09
9	0.08	0.09	0.10	0.06	0.09	0.08
10	0.08	0.08	0.09	0.07	0.08	0.08

Table 4.7: Directional thermal emittance at angles of 20° and 60° and total hemispherical emittance

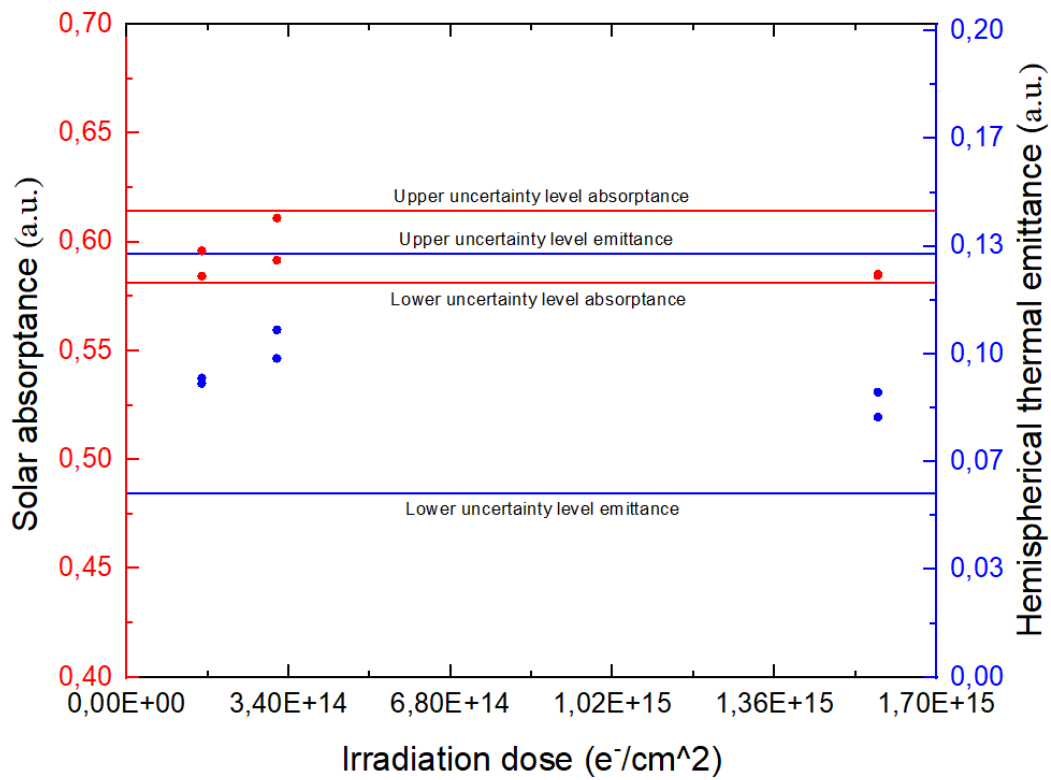
Solar Absorptance and Emittance of ZrB_2 Samples Versus Irradiation Dose

Figure 4.21: Solar absorptance and emittance of ZrB_2 plotted against irradiation dose

In Figure 4.22, the hemispherical thermal emittance is plotted against the sintering temperature of the ZrB_2 samples. Although Sample 7 I and UI deviate, there was a trend of decreasing emittance with increasing sintering temperatures. Nonetheless, due to the large measurement error of the emissiometer as seen with the upper and lower uncertainty levels, this trend is negligible. Additionally, it was expected that the sintering temperature would have a more prominent influence on the bulk properties than the optical properties of ZrB_2 .

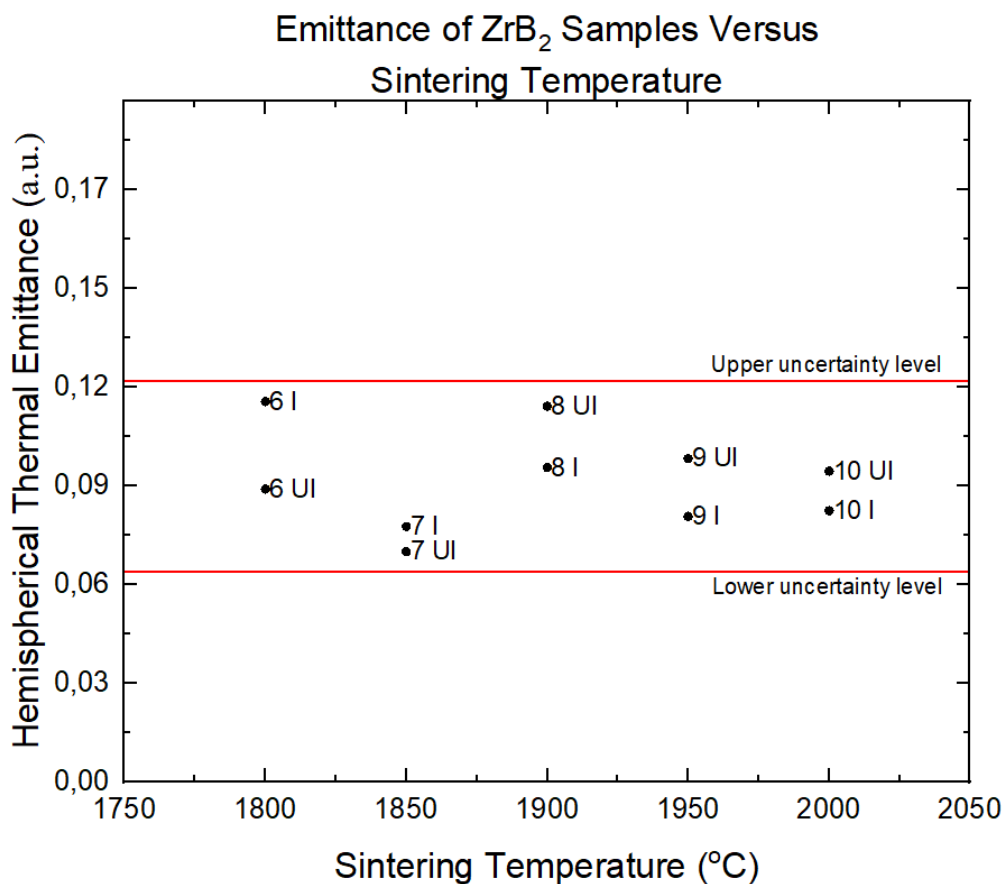


Figure 4.22: Emittance and sintering temperature of ZrB_2

Figure 4.23 displays the solar absorptance of ZrB_2 for various sintering temperatures. A positive correlation between the sintering temperatures and the absorptance was observed in this case. However, it can be seen that Sample 8's data points are outliers from this trend as the increase in absorptance is significantly larger. As with the emittance, the variation in solar absorptance between the ZrB_2 samples is negligible compared to the uncertainty of the measurement device. In this case, the uncertainty bars were included in the graph, as the data points exceeded the upper and lower uncertainty boundaries as opposed to the previous graphs. Similar to the thermal results, no radiation resistance effect of increasing the sintering temperature was seen with the optical properties. There was no clear deviating trend of the irradiated samples compared to the unirradiated samples.

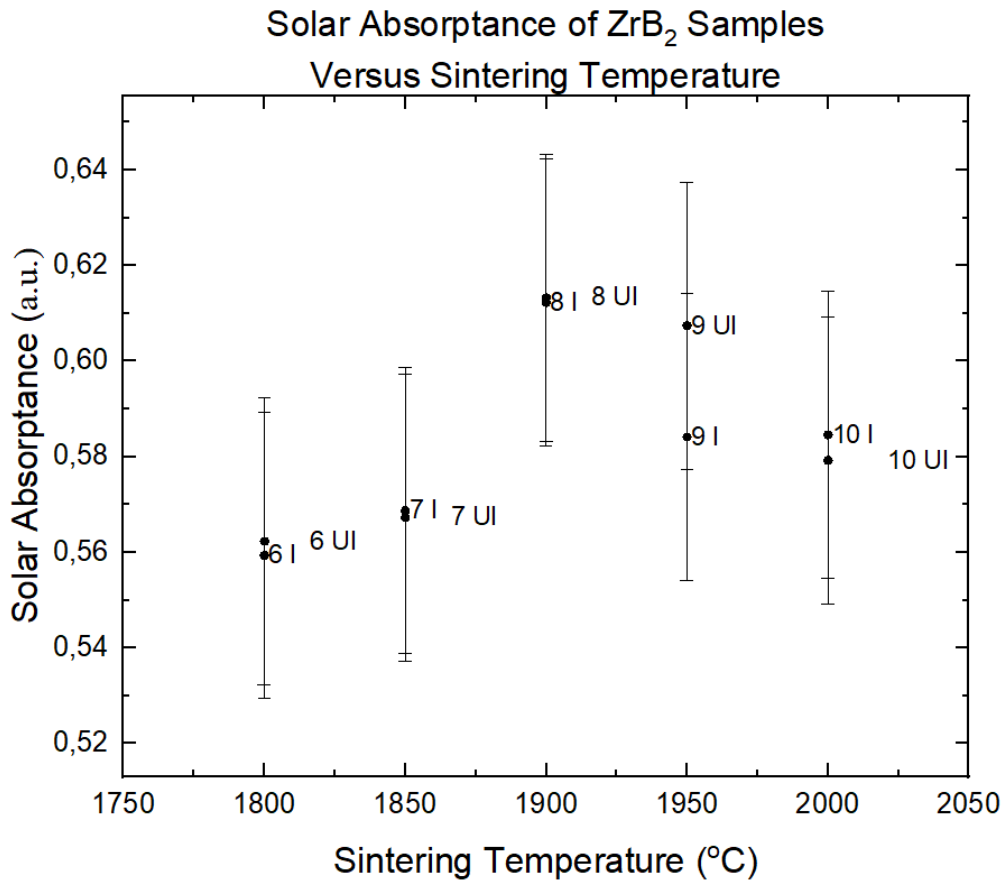


Figure 4.23: Solar absorptance and sintering temperature of ZrB₂

4.6.1. Surface Roughness and Optical Properties Investigation

As other studies indicated a correlation between roughness and optical properties; namely emittance and absorption, such an investigation was also carried out in the present study. This relationship was investigated by plotting the solar absorptance and hemispherical thermal emittance for ZrB₂ together with R_a . Figure 4.24 displays the absorptance and R_a for the measured samples. Based on the linear fit, there was a weak negative correlation between the two variables, but with a meager r-squared value, this can be neglected. In a previous study, it was found that for increasingly rough silicon surfaces, the absorption spectra shifted upwards. This would simultaneously lead to an increase in the solar absorption constant. The difference between surface roughness in silicon was smaller than in the ZrB₂ samples, and the mean arithmetic roughness itself was also smaller [67]. This could indicate a more robust polishing routine than that carried out with the ZrB₂ samples.

A similar case was seen with the hemispherical thermal emittance measurements in Figure 4.25, where a weak positive correlation was observed. Again, the r-squared value was too insignificant to conclude a relationship between the two variables. This was not the case with a prior study by Rozenbaum, Meneses, and Echegut that investigated the relationship between surface roughness and alumina emittance. It was discovered that with higher surface roughness, the emittance was higher due to a strengthening of surface scattering [68]. However, there are several possible reasons as to why this was not observed in the present study. First, the roughness values might not have varied to a sufficient degree to influence the optical surface properties. Additionally, the electron irradiation might not have caused sufficient surface effects to influence the surface roughness as explained earlier in this report. On the other hand, the study by Rozenbaum, Meneses, and Echegut does not directly connect surface roughness and emittance

but argues that an increase in porosity leads to a higher roughness. It would be helpful for comparison if the study had provided numerical data on the surface roughness.

As observed in the tabulated data, the irradiated samples generally had a lower mean arithmetic roughness than the unirradiated samples. Although the increasing irradiation dose does not increase the mean arithmetic roughness, this could indicate a smoothing surface effect from the irradiation originating from effects such as electron sputtering. There are outliers, such as Sample 7, which was unirradiated but had a low surface roughness. Additionally, to verify that the radiation influenced the surface roughness to such a degree, the roughness should have been measured pre and post-irradiation for the irradiated samples as well. Then, it could have been confirmed that minor variances in the polishing outcome were not the source of the differences. This would require the roughness measurements to be conducted in the exact same matter which could prove to be difficult to control as well.

There are certain limitations of this study originating from the experimental procedure. The difficulty in controlling the polishing outcome created large variations in the sample surfaces, which could have influenced the optical and thermal conductivity measurements. This was also likely reflected in the densification measurements. The samples had varying depths of graphite inclusions, which could not be removed entirely as the polishing routine was kept constant for all samples. One possibility would be determining an acceptable roughness for each sample after polishing. Minimizing graphite inclusions in the production phase could also be investigated. An alternative to this could also be to create thicker samples (10 mm thick) and cut them along the vertical axis. However, the issue of inhomogeneous heating during sintering would be an issue in this case.

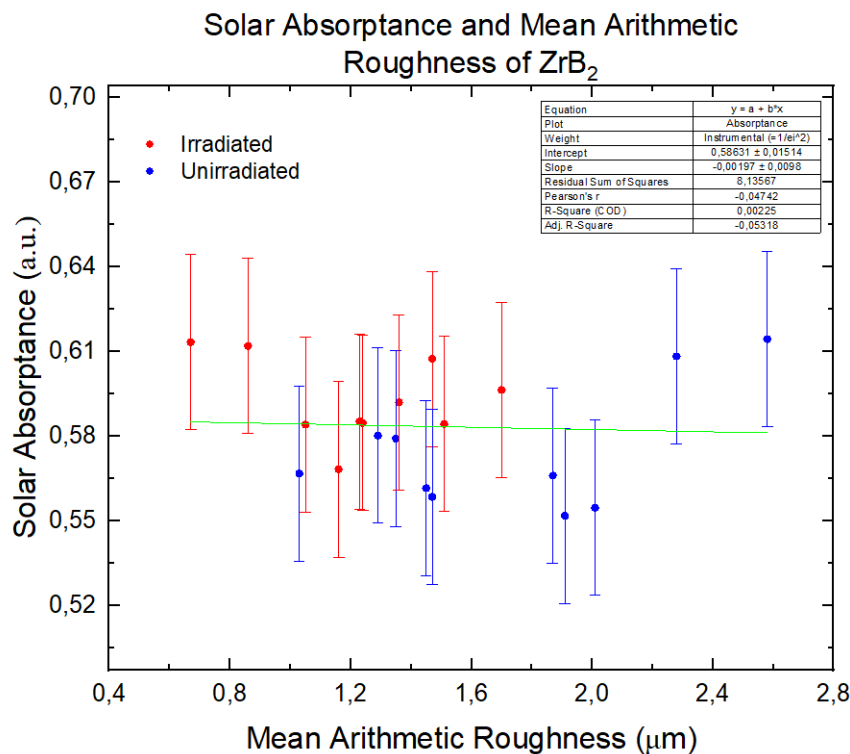


Figure 4.24: Solar absorbance versus mean arithmetic roughness of ZrB_2

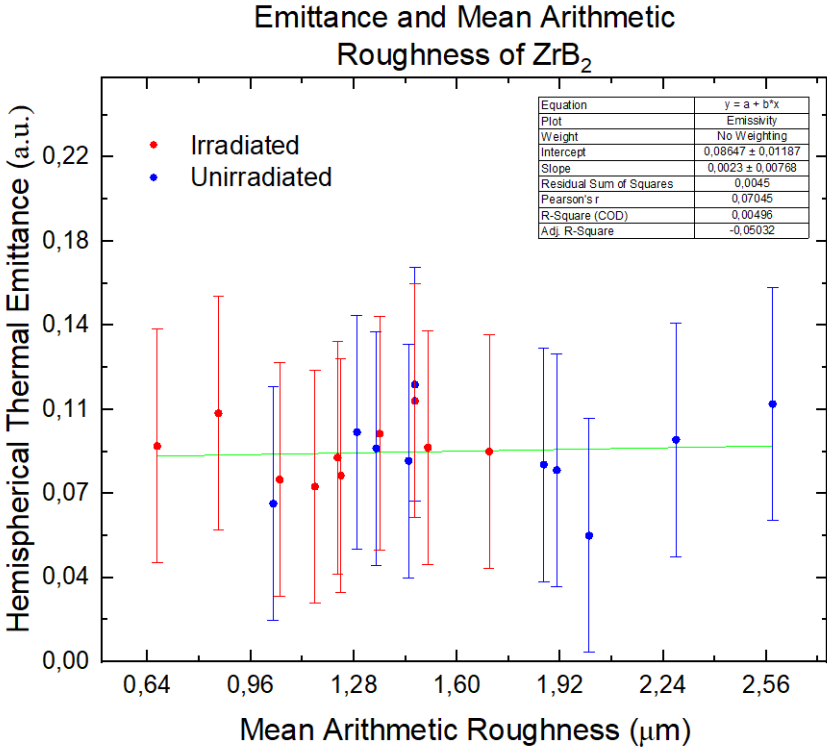


Figure 4.25: Emittance versus mean arithmetic roughness of ZrB₂

5

Conclusions

The main goal of this study was to investigate how exposure to electron radiation would influence zirconium diboride, specifically properties vital to its use as a thermal protection system. This was done by exposing spark plasma sintered ZrB_2 to 3 MeV electron radiation at fluences of $1.58\text{E}+14 \text{ e}^- \text{ cm}^{-2}$, $3.15\text{E}+14 \text{ e}^- \text{ cm}^{-2}$ and $1.58\text{E}+15 \text{ e}^- \text{ cm}^{-2}$. It can be concluded that the electron radiation had no significant influence on the thermo-optical characteristics of ZrB_2 and the material showed to be highly radiation resistant. Additionally, varying the sintering temperature did not influence the radiation resistance of ZrB_2 's thermo-optical properties. In view of its use as a thermal protection system in spacecraft, these are promising results, implying that long-term use in higher earth orbits such as geostationary orbit would cause negligible deterioration.

When analyzing the micro-structure of ZrB_2 , no significant differences were observed between the unirradiated and irradiated samples. Both samples had a relatively smooth boundary surface with some clusters of ZrB_2 grains visible. Effects seen in ion-irradiation such as ripples and pores were not visible, which could be due to limited damage by electron irradiation, or self-annealing of ZrB_2 originating from its metallic bonding.

The thermal conductivity of the ZrB_2 samples did not show any influence by the electron irradiation. It was expected to decrease with increasing irradiation doses, as explained by theory and previous studies. However, the absence of this relationship could be due to several differences in the studies, such as the type of irradiation, the significant inaccuracy in the thermal conductivity measurement method, and differences in the sintered materials themselves. However, it was also expected that electron irradiation would cause a less severe effect on the ceramic compared to neutron or ion irradiation. Additionally, the thermal conductivity measurement method had high inaccuracies. On the other hand, the thermal conductivity showed a negative relationship with sintering temperature, which was expected, based on the presumption that the density would increase as well. This was not the case, so the conductivity change was attributed to a possible difference in grain size.

As with thermal conductivity, the irradiation doses did not cause a significant change in the CTE of ZrB_2 . The CTE measurements could also have caused annealing of radiation damage, which could have influenced the data. On the other hand, CTE had a positive relationship with densification. This contradicted the expectation of a decreasing CTE with density. Furthermore, the electron irradiation doses in this study could have been insufficient to influence the bulk thermal properties as NASA indicated a significantly higher electron dose required to affect ceramics and metals. Lastly, there was no radiation resistance effect seen in the CTE and thermal conductivity of ZrB_2 from varying the sintering temperature.

No relationship was observed between the optical properties of ZrB_2 and the irradiation dose or sintering

temperature. The sintering temperature did not influence the resistance of the optical properties of the ceramic with increasing irradiation levels either. Although previous research had demonstrated a change in color in ZrB_2 due to irradiation, this was done with a heavier ion bombardment which could have stronger sputtering effects. However, the choice of irradiation doses was based on realistic mission lengths, and higher dose levels would deviate from the main scope of this project.

Under the simulated irradiation levels, it can be concluded that the electron radiation in the outer Van Allen belt will cause negligible thermo-optical property degradation of ZrB_2 , even over a 50-year period. Whether this would cause more damage to objects shielded by ZrB_2 is unknown, and was not within the scope of the present study. Nevertheless, based on the experiments conducted in this study, there are methods that can be improved upon and research directions that can build on this study. Examples of this will be described in the following chapter.

6

Further Recommendations

In this chapter, recommendations of topics for further research possibilities are detailed. These are based on topics and results mentioned in this thesis, but not explored further.

1. **Studying the influence of ion irradiation on the thermo-optical properties of ZrB₂**: Previous studies have used heavier particle irradiation onto ZrB₂ such as proton, helium, argon irradiation which have all demonstrated an influence on the material. This study observed no influence on the thermo-optical properties of ZrB₂ from electron irradiation. Therefore it would be compelling to investigate how heavier particle irradiation would influence its thermo-optical properties. It has already been shown that it can alter the color of ZrB₂, so it could affect the optical properties measured in this study.
2. **Investigating the influence of irradiation on mechanical properties of ZrB₂**: Additionally, other properties influenced by (electron) irradiation of ZrB₂ need to be explored. This includes other bulk properties of the material such as the mechanical properties. Examples of such properties would be the yield strength of the ceramic as well as the hardness and toughness.
3. **Simulating other space environment effects with ZrB₂**: Next to particle irradiation, other effects in the space environment can be explored for ZrB₂. For instance, the influence of atomic oxygen is critical to investigate, and would also be very relevant for hypersonic flight. The atomic oxygen damage belt is between 160 km to 700 km in altitude, making it especially relevant for LEO missions [69]. This causes oxidation, which could also be true for ZrB₂, especially under higher temperatures.
4. **Optical properties and surface roughness study**: No apparent relationship between the roughness and optical properties was observed in this study. However, this might result from the small range of roughness explored. With more significant differences in roughness, perhaps a relationship would be observed. This could be highly relevant for lunar missions, where lunar dust can cause significant damage to spacecraft components. It could also be expanded to other materials relevant to space exploration.
5. **Additives and irradiation of ZrB₂**: Several studies have investigated how additives could improve the material properties of ZrB₂, but none have investigated how this influences its irradiation resistance. Additionally, how such additives would influence other properties such as the oxidation of ZrB₂ has not been explored in detail. The optimal ZrB₂ based material in terms of withstanding radiation could be discovered through such a study.
6. **Changing other sintering parameters of ZrB₂**: Lastly, previous studies have investigated how changing sintering parameters such as sintering temperature, holding time, pressure and sintering time affect the grain size and density of ZrB₂. Investigating how varying such parameters would

affect the thermal, mechanical, and optical properties could be interesting for material optimization.

References

- [1] *PARKER SOLAR PROBE TOUCHES THE SUN FOR THE FIRST TIME, BRINGING NEW DISCOVERIES*. <https://hub.jhu.edu/2021/12/15/parker-solar-probe-touches-the-sun/>. Accessed: 2023-03-04.
- [2] Obinna Uyanna and Hamidreza Najafi. “Thermal protection systems for space vehicles: A review on technology development, current challenges and future prospects”. In: *Acta Astronautica* 176 (2020), pp. 341–356. ISSN: 0094-5765. DOI: <https://doi.org/10.1016/j.actaastro.2020.06.047>. URL: <https://www.sciencedirect.com/science/article/pii/S0094576520304148>.
- [3] *Space Radiation Effects On Electronics – Single Event Effects*. <https://spacetalos.com/news/space-radiation-effects-on-electronics-single-event-effects/>. Accessed: 2023-03-06.
- [4] Johnson Frank Guria, Ankit Bansal, and Vimal Kumar. “Effect of additives on the thermal conductivity of zirconium diboride based composites – A review”. In: *Journal of the European Ceramic Society* 41.1 (2021), pp. 1–23. ISSN: 0955-2219. DOI: <https://doi.org/10.1016/j.jeurceramsoc.2020.08.051>. URL: <https://www.sciencedirect.com/science/article/pii/S0955221920306932>.
- [5] Matthew J. Thompson. “Densification and thermal properties of zirconium diboride based ceramics”. PhD thesis. Missouri University of Science and Technology, Rolla, Jan. 2012.
- [6] Hiroyuki Kinoshita et al. “Zirconium Diboride (0001) as an Electrically Conductive Lattice-Matched Substrate for Gallium Nitride”. In: *Japanese Journal of Applied Physics* 40 (Dec. 2001). DOI: 10.1143/JJAP.40.L1280.
- [7] Tammana S. R. C. Murthy et al. “Boron-Based Ceramics and Composites for Nuclear and Space Applications: Synthesis and Consolidation”. In: *Handbook of Advanced Ceramics and Composites: Defense, Security, Aerospace and Energy Applications*. Ed. by Yashwant R. Mahajan and Roy Johnson. Cham: Springer International Publishing, 2020, pp. 703–738. ISBN: 978-3-030-16347-1. DOI: 10.1007/978-3-030-16347-1_22. URL: https://doi.org/10.1007/978-3-030-16347-1_22.
- [8] Ya F. Yang and Ma Qian. “13 - Spark plasma sintering and hot pressing of titanium and titanium alloys”. In: *Titanium Powder Metallurgy*. Ed. by Ma Qian and Francis H. (Sam) Froes. Boston: Butterworth-Heinemann, 2015, pp. 219–235. ISBN: 978-0-12-800054-0. DOI: <https://doi.org/10.1016/B978-0-12-800054-0.00013-7>. URL: <https://www.sciencedirect.com/science/article/pii/B9780128000540000137>.
- [9] Shu-Qi Guo et al. “Spark Plasma Sintering of Zirconium Diborides”. In: *Journal of the American Ceramic Society* 91.9 (2008), pp. 2848–2855. DOI: <https://doi.org/10.1111/j.1551-2916.2008.02587.x>. eprint: <https://ceramics.onlinelibrary.wiley.com/doi/pdf/10.1111/j.1551-2916.2008.02587.x>. URL: <https://ceramics.onlinelibrary.wiley.com/doi/abs/10.1111/j.1551-2916.2008.02587.x>.
- [10] Denis Yushin et al. “Modeling Process of Spark Plasma Sintering of Powder Materials by Finite Element Method”. In: *Materials Science Forum* 834 (Nov. 2015), pp. 41–50. DOI: 10.4028/www.scientific.net/MSF.834.41.
- [11] P. Sengupta and I Manna. “Advanced High-Temperature Structural Materials for Aerospace and Power Sectors: A Critical Review”. In: *Trans Indian Inst Met* 72 (2019), pp. 2043–2059.

- [12] Ya-zheng Yang, Jialing Yang, and Dai-ning Fang. “Research Progress on Thermal Protection Materials and Structures of Hypersonic Vehicles”. In: *Applied Mathematics and Mechanics* 29 (Jan. 2008), pp. 51–60. DOI: 10.1007/s10483-008-0107-1.
- [13] Sylvia M. Johnson et al. “Biologically-Derived Photonic Materials for Thermal Protection Systems”. In: 2014.
- [14] *Thermal Conductivity*. https://www.nde-ed.org/Physics/Materials/Physical_Chemical/SpecificGravity.xhtml. Accessed: 2023-09-18.
- [15] GÖRAN GRIMVALL. “CHAPTER 16 - THERMAL CONDUCTIVITY”. In: *Thermophysical Properties of Materials*. Ed. by GÖRAN GRIMVALL. Amsterdam: Elsevier Science B.V., 1999, pp. 255–285. ISBN: 978-0-444-82794-4. DOI: <https://doi.org/10.1016/B978-044482794-4/50017-6>. URL: <https://www.sciencedirect.com/science/article/pii/B9780444827944500176>.
- [16] Marsha A. Presley and Philip R. Christensen. “Thermal conductivity measurements of particulate materials: 4. Effect of bulk density for granular particles”. In: *Journal of Geophysical Research: Planets* 115.E7 (2010). DOI: <https://doi.org/10.1029/2009JE003482>. eprint: <https://agupubs.onlinelibrary.wiley.com/doi/pdf/10.1029/2009JE003482>. URL: <https://agupubs.onlinelibrary.wiley.com/doi/abs/10.1029/2009JE003482>.
- [17] Luning Zhang et al. “Thermal and Electrical Transport Properties of Spark Plasma-Sintered HfB₂ and ZrB₂ Ceramics”. In: *Journal of the American Ceramic Society* 94.8 (2011), pp. 2562–2570. DOI: <https://doi.org/10.1111/j.1551-2916.2011.04411.x>. eprint: <https://ceramics.onlinelibrary.wiley.com/doi/pdf/10.1111/j.1551-2916.2011.04411.x>. URL: <https://ceramics.onlinelibrary.wiley.com/doi/abs/10.1111/j.1551-2916.2011.04411.x>.
- [18] A. Nedoseka. “2 - Welding stresses and strains”. In: *Fundamentals of Evaluation and Diagnostics of Welded Structures*. Ed. by A. Nedoseka. Woodhead Publishing Series in Welding and Other Joining Technologies. Woodhead Publishing, 2012, pp. 72–182. ISBN: 978-0-85709-531-2. DOI: <https://doi.org/10.1533/9780857097576.72>. URL: <https://www.sciencedirect.com/science/article/pii/B9780857095312500023>.
- [19] *List of Thermal Expansion Coefficients (CTE) for Natural and Engineered Materials*. <https://www.msesupplies.com/pages/list-of-thermal-expansion-coefficients-cte-for-natural-and-engineered-materials>. Accessed: 2023-09-18.
- [20] V.N. Zharkov. “On the dependence of the coefficient of thermal expansion on density”. In: *Physics of the Earth and Planetary Interiors* 109.1 (1998), pp. 79–89. ISSN: 0031-9201. DOI: [https://doi.org/10.1016/S0031-9201\(98\)00115-0](https://doi.org/10.1016/S0031-9201(98)00115-0). URL: <https://www.sciencedirect.com/science/article/pii/S0031920198001150>.
- [21] Rasul Abdullaev et al. “Density and Thermal Expansion of High Purity Nickel over the Temperature Range from 150 K to 2030 K”. In: *International Journal of Thermophysics* 36 (Apr. 2015). DOI: 10.1007/s10765-015-1839-x.
- [22] William Paxton et al. “Anisotropic Thermal Expansion of Zirconium Diboride: An Energy-Dispersive X-Ray Diffraction Study”. In: *Journal of Ceramics* 2016 (Jan. 2016), pp. 1–5. DOI: 10.1155/2016/8346563.
- [23] Hu Ertao et al. “Optical Properties of Solar Absorber Materials and Structures”. In: Aug. 2021, pp. 1–165. ISBN: 978-981-16-3491-8. DOI: 10.1007/978-981-16-3492-5_1.
- [24] Etienne Blandre, Pierre-Olivier Chapuis, and Rodolphe Vaillon. “Spectral and total temperature-dependent emissivity of few-layer structures on a metallic substrate”. In: *Optics Express* 24 (Jan. 2016), A374. DOI: 10.1364/OE.24.00A374.
- [25] John Howell, M. Pinar Mengüç, and Robert Siegel. *Thermal Radiation Heat Transfer*. Sept. 2015. ISBN: 9780429190599. DOI: 10.1201/b18835.

- [26] Elisa Sani et al. “Optical properties of dense zirconium and tantalum diborides for solar thermal absorbers”. In: *Renewable Energy* 91 (June 2016), pp. 340–346. DOI: 10.1016/j.renene.2016.01.068.
- [27] Chang-Da Wen and Issam Mudawar. “Modeling the effects of surface roughness on the emissivity of aluminum alloys”. In: *International Journal of Heat and Mass Transfer* 49.23 (2006), pp. 4279–4289. ISSN: 0017-9310. DOI: <https://doi.org/10.1016/j.ijheatmasstransfer.2006.04.037>. URL: <https://www.sciencedirect.com/science/article/pii/S0017931006003152>.
- [28] Ajit Senapati. “A REVIEW ON THE EFFECT OF PROCESS PARAMETERS ON DIFFERENT OUTPUT PARAMETERS DURING MACHINING OF SEVERAL MATERIALS”. In: *International Journal of Engineering Science and Technology* (Mar. 2014).
- [29] R.G Hering and T.F Smith. “Surface roughness effects on radiant transfer between surfaces”. In: *International Journal of Heat and Mass Transfer* 13.4 (1970), pp. 725–739. ISSN: 0017-9310. DOI: [https://doi.org/10.1016/0017-9310\(70\)90046-3](https://doi.org/10.1016/0017-9310(70)90046-3). URL: <https://www.sciencedirect.com/science/article/pii/0017931070900463>.
- [30] Ronald A. Kohser E. Degarmo J. T. Black. *Materials and Processes in Manufacturing*. 2003. ISBN: 9780471429449.
- [31] Masoud Rais-Rohani. “On Structural Design of a Mobile Lunar Habitat with Multi-Layered Environmental Shielding (NASA/CR-2005-213845)”. In: (Apr. 2005). DOI: 10.13140/RG.2.1.3120.4962.
- [32] W. Li and M.K. Hudson. “Earth’s Van Allen Radiation Belts: From Discovery to the Van Allen Probes Era”. In: *Journal of Geophysical Research: Space Physics* 124.11 (2019), pp. 8319–8351. DOI: <https://doi.org/10.1029/2018JA025940>. eprint: <https://agupubs.onlinelibrary.wiley.com/doi/pdf/10.1029/2018JA025940>. URL: <https://agupubs.onlinelibrary.wiley.com/doi/abs/10.1029/2018JA025940>.
- [33] Paul Mark Thelen. “Introduction to the Space Radiation Environment.” In: (June 2018). URL: <https://www.osti.gov/biblio/1524958>.
- [34] Christa Baumstark-Khan and R. Facius. *Life under Conditions of Ionizing Radiation*. Jan. 2002, pp. 261–284. ISBN: 3-540-42101-7. DOI: 10.1007/978-3-642-59381-9_18.
- [35] Cary Zeitlin and Chiara La Tessa. “The Role of Nuclear Fragmentation in Particle Therapy and Space Radiation Protection”. In: *Frontiers in Oncology* 6 (Mar. 2016). DOI: 10.3389/fonc.2016.00065.
- [36] *Lecture : Particle Interactions with Matter*. <https://indico.cern.ch/event/145296/contributions/1381063/attachments/136866/194145/Particle-Interaction-Matter-upload.pdf>. Accessed: 2023-09-19.
- [37] Glenn F. Knoll. *Radiation Detection and Measurement*. Wiley, 2010.
- [38] Gary Was. “Fundamentals of Radiation Materials Science: Metals and Alloys”. In: *Fundamentals of Radiation Materials Science: Metals and Alloys* (Jan. 2007), pp. 1–827. DOI: 10.1007/978-3-540-49472-0.
- [39] Weichao Bao et al. “Structural integrity and damage of ZrB₂ ceramics after 4MeV Au ions irradiation”. In: *Journal of Materials Science Technology* 72 (2021), pp. 223–230. ISSN: 1005-0302. DOI: <https://doi.org/10.1016/j.jmst.2020.09.019>. URL: <https://www.sciencedirect.com/science/article/pii/S1005030220308264>.
- [40] Haonan Chen et al. “Effect of electron beam irradiation in TEM on the microstructure and composition of nanoprecipitates in Al-Mg-Si alloys”. In: *Micron* 116 (2019), pp. 116–123. ISSN: 0968-4328. DOI: <https://doi.org/10.1016/j.micron.2018.10.003>. URL: <https://www.sciencedirect.com/science/article/pii/S0968432818302646>.
- [41] Anton Lechner. “Particle interactions with matter”. In: *CERN Yellow Rep. School Proc.* 5 (2018). Ed. by Bernhard Holzer, p. 47. DOI: 10.23730/CYRSP-2018-005.47.

- [42] Natalia E. Koval et al. “Modeling Radiation Damage in Materials Relevant for Exploration and Settlement on the Moon”. In: *Lunar Science*. Ed. by Yann-Henri Chemin. Rijeka: IntechOpen, 2022. Chap. 4. DOI: 10.5772/intechopen.102808. URL: <https://doi.org/10.5772/intechopen.102808>.
- [43] *ESTAR: Stopping Powers and Ranges for Electrons*. <https://physics.nist.gov/PhysRefData/Star/Text/method.html>. Accessed: 2023-03-06.
- [44] Javier Fernández-Tejero. “Design and Optimization of Advanced Silicon Strip Detectors for High Energy Physics Experiments”. PhD thesis. July 2020. DOI: 10.13140/RG.2.2.22580.07048.
- [45] *Irradiation Effects in Nuclear Materials: Part One*. <https://www.totalmateria.com/page.aspx?ID=CheckArticle&site=kts&NM=536>. Accessed: 2023-03-06.
- [46] Alan W. Smith and Ned S. Rasor. “Observed Dependence of the Low-Temperature Thermal and Electrical Conductivity of Graphite on Temperature, Type, Neutron Irradiation, and Bromination”. In: *Phys. Rev.* 104 (4 Nov. 1956), pp. 885–891. DOI: 10.1103/PhysRev.104.885. URL: <https://link.aps.org/doi/10.1103/PhysRev.104.885>.
- [47] Patricia B. Weisensee, Joseph P. Feser, and David G. Cahill. “Effect of ion irradiation on the thermal conductivity of UO₂ and U₃O₈ epitaxial layers”. In: *Journal of Nuclear Materials* 443.1 (2013), pp. 212–217. ISSN: 0022-3115. DOI: <https://doi.org/10.1016/j.jnucmat.2013.07.021>. URL: <https://www.sciencedirect.com/science/article/pii/S0022311513009094>.
- [48] C. M. Pieters et al. “Optical effects of space weathering: The role of the finest fraction”. In: *Journal of Geophysical Research: Planets* 98.E11 (1993), pp. 20817–20824. DOI: <https://doi.org/10.1029/93JE02467>. eprint: <https://agupubs.onlinelibrary.wiley.com/doi/pdf/10.1029/93JE02467>. URL: <https://agupubs.onlinelibrary.wiley.com/doi/abs/10.1029/93JE02467>.
- [49] Kanuchová, Z. et al. “Space weathering of asteroidal surfaces* - Influence on the UV-Vis spectra”. In: *A&A* 517 (2010), A60. DOI: 10.1051/0004-6361/201014061. URL: <https://doi.org/10.1051/0004-6361/201014061>.
- [50] *Radiation*. <https://www.britannica.com/science/radiation>. Accessed: 2023-02-09.
- [51] *Ion beam sputter deposition*. <https://polygonphysics.com/applications/ion-beam-sputter-deposition/>. Accessed: 2023-03-05.
- [52] Gary Was. “Challenges to the use of ion irradiation for emulating reactor irradiation”. In: *Journal of Materials Research* 30 (May 2015), pp. 1–25. DOI: 10.1557/jmr.2015.73.
- [53] Lauren M. Garrison et al. “The response of ZrB₂ to simulated plasma-facing material conditions of He irradiation at high temperature”. In: *Journal of Nuclear Materials* 507 (2018), pp. 112–125. ISSN: 0022-3115. DOI: <https://doi.org/10.1016/j.jnucmat.2018.04.016>. URL: <https://www.sciencedirect.com/science/article/pii/S0022311517311303>.
- [54] *Effects of Radiation Damage*. [Online; accessed 2023-01-31]. Nov. 2020.
- [55] Bernhard Hidding et al. “Laser-plasma-based Space Radiation Reproduction in the Laboratory”. In: *Scientific Reports* 7 (Feb. 2017). DOI: 10.1038/srep42354.
- [56] *Pulsed high-energy electron accelerator facilities*. <https://www.tudelft.nl/tnw/over-faculteit/afdelingen/chemical-engineering/principal-scientists/laurens-siebbeles/laurens-siebbeles-group/experimental-facilities/pulsed-high-energy-electron-accelerator-facilities>. Accessed: 2023-03-22.
- [57] F.C. Grozema. “Opto-Electronic Properties of Conjugated Molecular Wires”. In: (July 2023).
- [58] Lisa-Marie Heisig, Rhena Wulf, and Tobias Fieback. “Investigation and Optimization of the Hot Disk Method for Thermal Conductivity Measurements up to 750 °C”. In: *International Journal of Thermophysics* 44 (Apr. 2023). DOI: 10.1007/s10765-023-03190-6.
- [59] Pierre Villars and Karin Cenzual. *ZrB₂ Crystal Structure*. Copyright 2023 Springer-Verlag Berlin Heidelberg & Material Phases Data System (MPDS), Switzerland & National Institute for Mate-

- rials Science (NIMS), Japan. URL: https://materials.springer.com/isp/crystallographic/docs/sd_0251829.
- [60] Pierre Villars, Cenzual, and Karin. *C Crystal Structure*. Copyright 2023 Springer-Verlag Berlin Heidelberg & Material Phases Data System (MPDS), Switzerland & National Institute for Materials Science (NIMS), Japan. URL: https://materials.springer.com/isp/crystallographic/docs/sd_1637904.
- [61] G. Carter and V. Vishnyakov. “Roughening and ripple instabilities on ion-bombarded Si”. In: *Phys. Rev. B* 54 (24 Dec. 1996), pp. 17647–17653. DOI: 10.1103/PhysRevB.54.17647. URL: <https://link.aps.org/doi/10.1103/PhysRevB.54.17647>.
- [62] James W. Zimmermann et al. “Thermophysical Properties of ZrB₂ and ZrB₂-SiC Ceramics”. In: *Journal of the American Ceramic Society* 91.5 (2008), pp. 1405–1411. DOI: <https://doi.org/10.1111/j.1551-2916.2008.02268.x>. eprint: <https://ceramics.onlinelibrary.wiley.com/doi/pdf/10.1111/j.1551-2916.2008.02268.x>. URL: <https://ceramics.onlinelibrary.wiley.com/doi/abs/10.1111/j.1551-2916.2008.02268.x>.
- [63] L.L. Snead, S.J. Zinkle, and D.P. White. “Thermal conductivity degradation of ceramic materials due to low temperature, low dose neutron irradiation”. In: *Journal of Nuclear Materials* 340.2 (2005), pp. 187–202. ISSN: 0022-3115. DOI: <https://doi.org/10.1016/j.jnucmat.2004.11.009>. URL: <https://www.sciencedirect.com/science/article/pii/S0022311504010001>.
- [64] PAIGE L. HIGBY et al. “Radiation Effects on the Physical Properties of Low-Expansion-Coefficient Glasses and Ceramics”. In: *Journal of the American Ceramic Society* 71.9 (1988), pp. 796–802. DOI: <https://doi.org/10.1111/j.1151-2916.1988.tb06416.x>. eprint: <https://ceramics.onlinelibrary.wiley.com/doi/pdf/10.1111/j.1151-2916.1988.tb06416.x>. URL: <https://ceramics.onlinelibrary.wiley.com/doi/abs/10.1111/j.1151-2916.1988.tb06416.x>.
- [65] Harold Shulman and William S. Ginell. “Nuclear and Space Radiation Effects on Materials, NASA SPACE VEHICLE DESIGN CRITERIA (Structures)”. In: 1970.
- [66] Xinghang Zhang et al. “Radiation damage in nanostructured materials”. In: *Progress in Materials Science* 96 (2018), pp. 217–321. ISSN: 0079-6425. DOI: <https://doi.org/10.1016/j.pmatsci.2018.03.002>. URL: <https://www.sciencedirect.com/science/article/pii/S007964251830032X>.
- [67] Chunhui Niu, Ting Zhu, and Yong Lv. “Influence of Surface Morphology on Absorptivity of Light-Absorbing Materials”. In: *International Journal of Photoenergy* 2019 (Sept. 2019), pp. 1–9. DOI: 10.1155/2019/1476217.
- [68] Olivier Rozenbaum, Domingos Meneses, and Patrick Echegut. “Texture and Porosity Effects on the Thermal Radiative Behavior of Alumina Ceramics”. In: *International Journal of Thermophysics* 30 (Apr. 2009), pp. 580–590. DOI: 10.1007/s10765-008-0510-1.
- [69] Bruce Banks et al. “Atomic Oxygen Effects on Spacecraft Materials”. In: (July 2003).

A

X-ray Diffraction Reference Data in Vesta

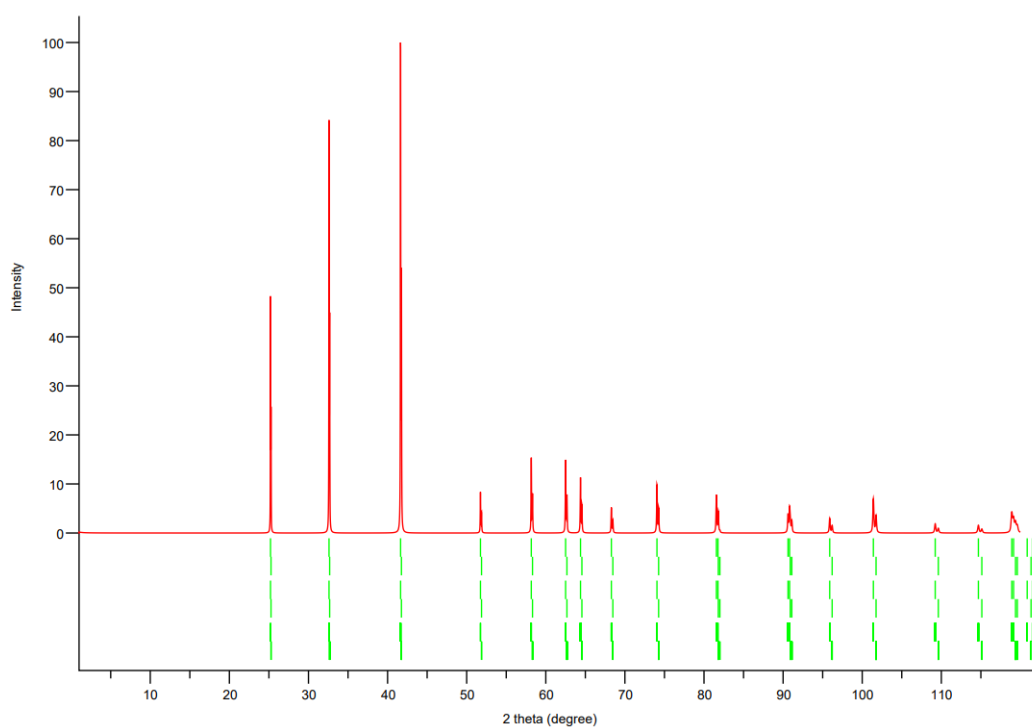


Figure A.1: XRD ZrB₂ Reference [59]

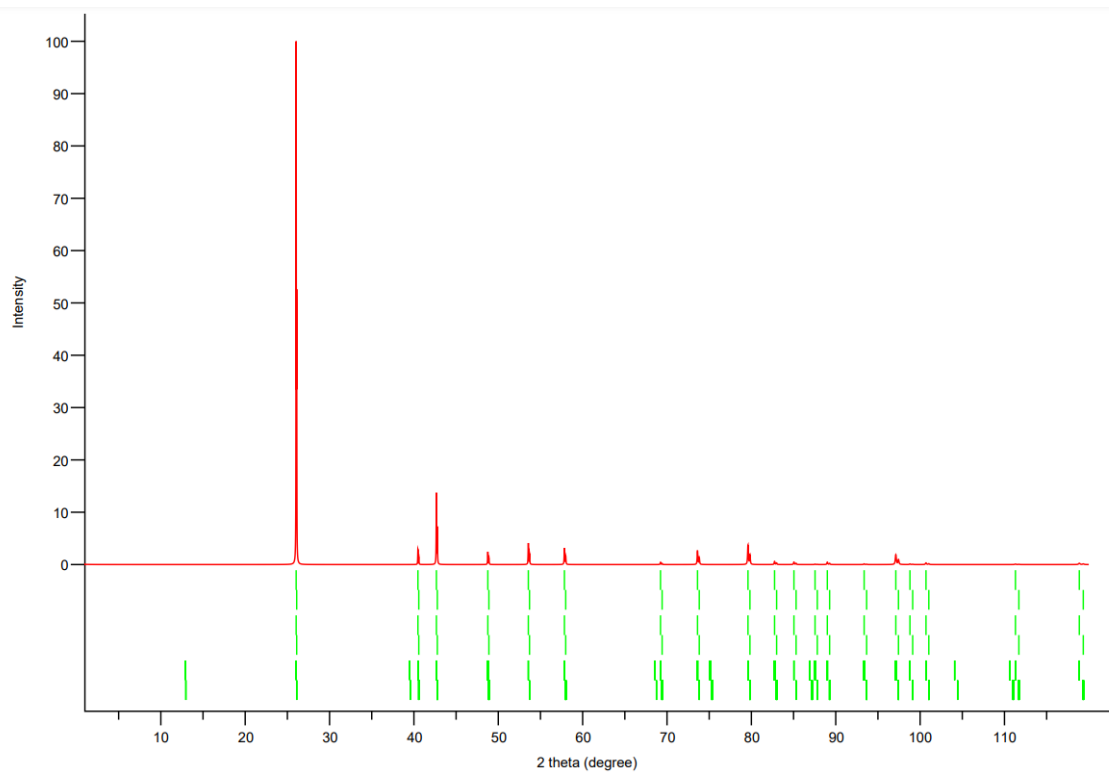


Figure A.2: XRD C Reference [60]

B

Reflectance Spectra of ZrB_2 Samples from Spectrophotometer

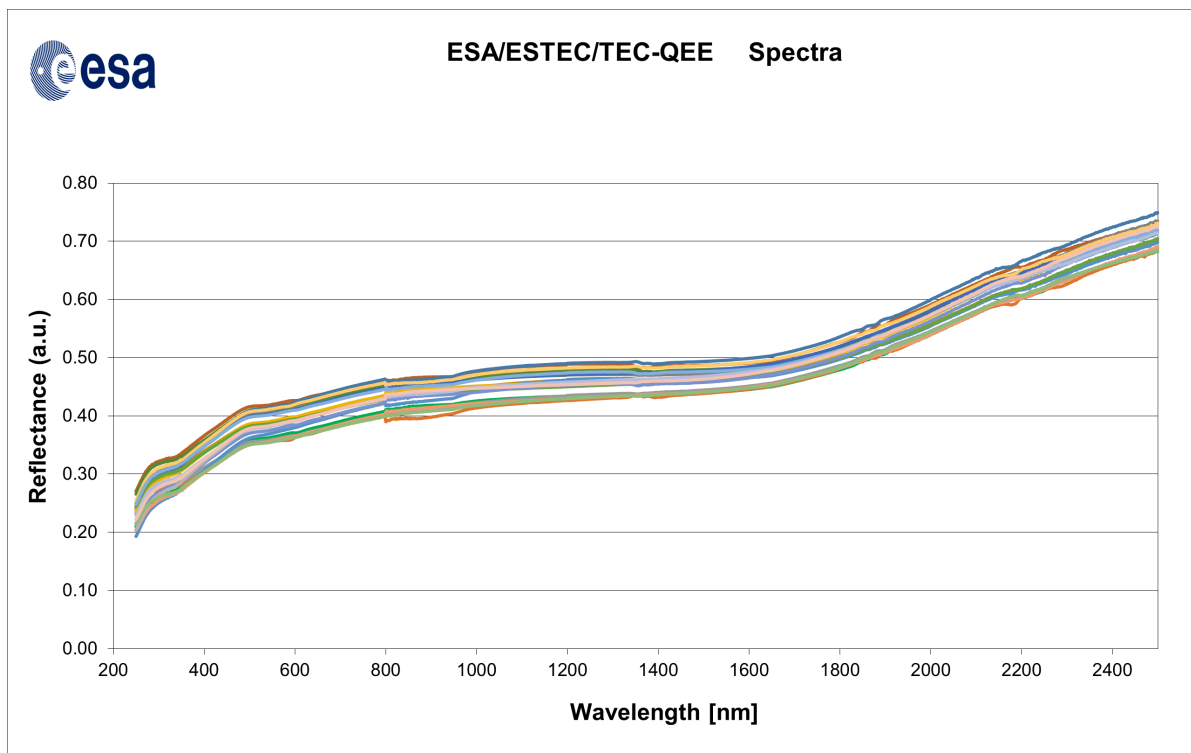


Figure B.1: Reflectance spectra of ZrB_2 samples

C

CTE of ZrB₂ Samples

Sample	CTE K^{-1}	Irradiated Sample	CTE K^{-1}
Sample 1	1,20758E-5	Sample 1	1,18968E-5
Sample 2	9,25413E-6	Sample 2	9,99834E-6
Sample 3	1,07385E-5	Sample 3	9,33203E-6
Sample 4	1,21745E-5	Sample 4	1,06656E-5
Sample 5	1,02599E-5	Sample 5	1,0211E-5
Sample 6	9,28115E-6	Sample 6	1,46947E-5
Sample 7	3,4126E-6	Sample 7	1,31409E-5
Sample 8	1,16383E-5	Sample 8	1,09711E-5
Sample 9	1,59025E-5	Sample 9	9,96677E-6
Sample 10	7,7387E-8	Sample 10	1,02363E-5

Table C.1: CTE of unirradiated and irradiated samples

D

Thermal Conductivity Data

Sample	Thermal C. ($\text{W m}^{-1} \text{K}^{-1}$)	Irradiated Sample	Thermal C. ($\text{W m}^{-1} \text{K}^{-1}$)
Sample 1	48.53	Sample 1	51
Sample 2	51.31	Sample 2	49.65
Sample 3	53.46	Sample 3	52.3
Sample 4	49.95	Sample 4	54.6
Sample 5	51.68	Sample 5	50.89
Sample 6	56.77	Sample 6	58.93
Sample 7	58.24	Sample 7	55.21
Sample 8	54.01	Sample 8	52.3
Sample 9	53.46	Sample 9	47.08
Sample 10	47.63	Sample 10	45.46

Table D.1: Thermal conductivity of unirradiated and irradiated samples

E

Transient temperature increase in Hot Disk

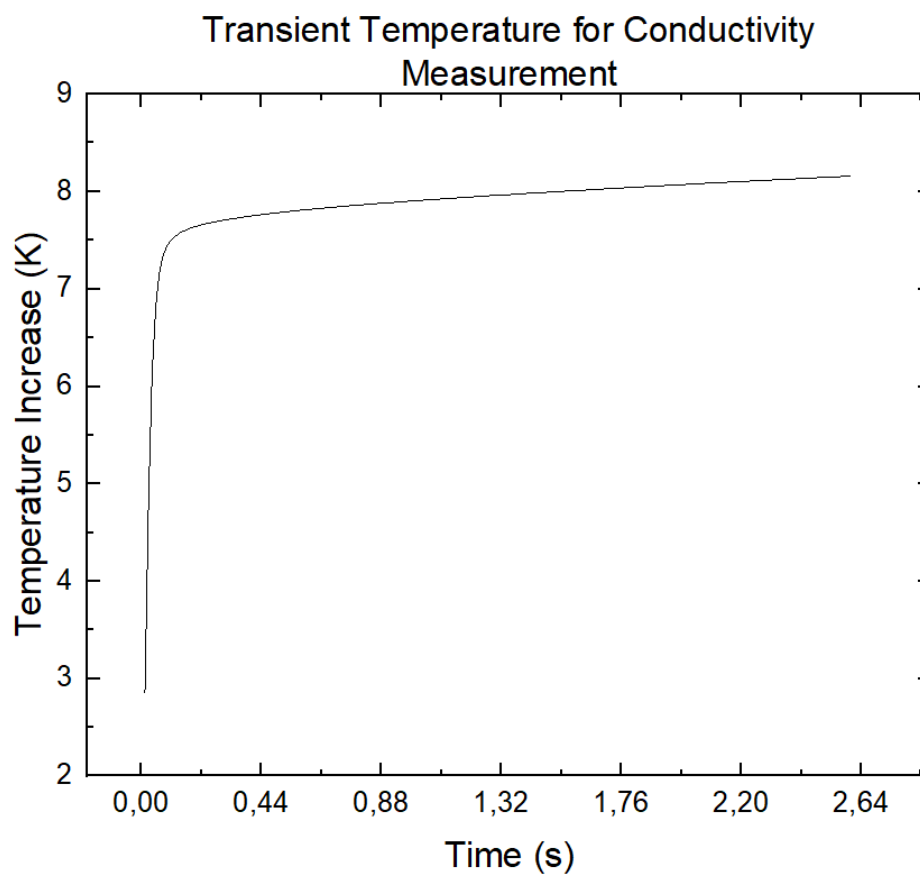


Figure E.1: Transient temperature increase during 2.5s

F

Raw emittance data

Sample	Angle 20										Angle 60													
	1.5-2.0		2.0-3.5		3.0-4.0		4.0-5.0		5.0-10.5		10.5-21.0		1.5-2.0		2.0-3.5		3.0-4.0		4.0-5.0		5.0-10.5		10.5-21.0	
	R	R	R	R	R	R	R	R	R	R	R	R	R	R	R	R	R	R	R	R	R	R	R	R
1 UI	0.525	0.696	0.82	0.843	0.876	0.92	0.519	0.677	0.804	0.838	0.873	0.911	0.519	0.677	0.804	0.838	0.873	0.911	0.519	0.677	0.804	0.838	0.873	0.911
2 UI	0.577	0.747	0.862	0.887	0.914	0.946	0.554	0.716	0.838	0.87	0.902	0.938	0.554	0.716	0.838	0.87	0.902	0.938	0.554	0.716	0.838	0.87	0.902	0.938
3 UI	0.563	0.738	0.863	0.881	0.911	0.945	0.543	0.71	0.842	0.873	0.909	0.94	0.543	0.71	0.842	0.873	0.909	0.94	0.543	0.71	0.842	0.873	0.909	0.94
4 UI	0.54	0.704	0.829	0.857	0.892	0.938	0.527	0.682	0.813	0.852	0.889	0.931	0.527	0.682	0.813	0.852	0.889	0.931	0.527	0.682	0.813	0.852	0.889	0.931
5 UI	0.598	0.772	0.89	0.916	0.941	0.967	0.547	0.712	0.843	0.882	0.916	0.952	0.547	0.712	0.843	0.882	0.916	0.952	0.547	0.712	0.843	0.882	0.916	0.952
6 UI	0.582	0.747	0.863	0.886	0.914	0.94	0.539	0.686	0.801	0.835	0.866	0.902	0.539	0.686	0.801	0.835	0.866	0.902	0.539	0.686	0.801	0.835	0.866	0.902
7 UI	0.573	0.744	0.867	0.896	0.924	0.96	0.546	0.709	0.841	0.878	0.907	0.945	0.546	0.709	0.841	0.878	0.907	0.945	0.546	0.709	0.841	0.878	0.907	0.945
8 UI	0.521	0.686	0.812	0.852	0.883	0.927	0.506	0.659	0.786	0.836	0.861	0.906	0.506	0.659	0.786	0.836	0.861	0.906	0.506	0.659	0.786	0.836	0.861	0.906
9 UI	0.543	0.712	0.833	0.863	0.899	0.939	0.532	0.689	0.813	0.855	0.886	0.926	0.532	0.689	0.813	0.855	0.886	0.926	0.532	0.689	0.813	0.855	0.886	0.926
10 UI	0.554	0.727	0.854	0.871	0.903	0.94	0.533	0.697	0.831	0.862	0.899	0.932	0.533	0.697	0.831	0.862	0.899	0.932	0.533	0.697	0.831	0.862	0.899	0.932
1 I	0.543	0.709	0.836	0.863	0.903	0.943	0.522	0.676	0.807	0.848	0.89	0.935	0.522	0.676	0.807	0.848	0.89	0.935	0.522	0.676	0.807	0.848	0.89	0.935
2 I	0.544	0.711	0.842	0.864	0.899	0.943	0.525	0.684	0.82	0.856	0.896	0.937	0.525	0.684	0.82	0.856	0.896	0.937	0.525	0.684	0.82	0.856	0.896	0.937
3 I	0.535	0.706	0.835	0.86	0.895	0.938	0.536	0.699	0.83	0.867	0.902	0.94	0.536	0.699	0.83	0.867	0.902	0.94	0.536	0.699	0.83	0.867	0.902	0.94
4 I	0.512	0.681	0.814	0.838	0.883	0.934	0.511	0.669	0.804	0.843	0.887	0.927	0.511	0.669	0.804	0.843	0.887	0.927	0.511	0.669	0.804	0.843	0.887	0.927
5 I	0.556	0.731	0.857	0.876	0.909	0.943	0.552	0.717	0.843	0.88	0.91	0.944	0.552	0.717	0.843	0.88	0.91	0.944	0.552	0.717	0.843	0.88	0.91	0.944
6 I	0.546	0.705	0.817	0.848	0.883	0.926	0.547	0.701	0.815	0.852	0.884	0.921	0.547	0.701	0.815	0.852	0.884	0.921	0.547	0.701	0.815	0.852	0.884	0.921
7 I	0.564	0.735	0.861	0.886	0.92	0.953	0.548	0.711	0.841	0.879	0.912	0.947	0.548	0.711	0.841	0.879	0.912	0.947	0.548	0.711	0.841	0.879	0.912	0.947
8 I	0.541	0.712	0.837	0.867	0.9	0.942	0.53	0.687	0.811	0.851	0.878	0.92	0.53	0.687	0.811	0.851	0.878	0.92	0.53	0.687	0.811	0.851	0.878	0.92
9 I	0.553	0.728	0.854	0.882	0.917	0.95	0.534	0.692	0.82	0.855	0.891	0.927	0.534	0.692	0.82	0.855	0.891	0.927	0.534	0.692	0.82	0.855	0.891	0.927
10 I	0.565	0.738	0.859	0.881	0.916	0.949	0.539	0.703	0.837	0.868	0.905	0.941	0.539	0.703	0.837	0.868	0.905	0.941	0.539	0.703	0.837	0.868	0.905	0.941

Table F.1: Reflectance values (R) for emittance angles of 20° and 60°

G

Calculated Lattice Parameters

Peak Position (°)	Lattice Parameter c (Å)	Peak Position (°)	Lattice Parameter a (Å)
25.28	3.520149603	32.66	3.163433184
51.80	3.526977318	58.22	3.166759295
		68.32	3.168124013
Average	3.52356346	Average	3.166105497

Table G.1: Calculated lattice parameters and average values